Optical Properties of Semiconductor Quantum Dots

Optical Properties of
Semiconductor Quantum Dots

Proefschrift

ter verkrijging van de graad van doctor
aan de Technische Universiteit Delft,
op gezag van de Rector Magnificus prof. ir. K. C. A. M. Luyben,
voorzitter van het College voor Promoties,
in het openbaar te verdedigen
op donderdag 17 februari 2011 om 10.00 uur

door

Umberto PERINETTI

Laurea Specialistica in Scienze Fisiche, Universitá di Pisa, Italië
geboren te L'Aquila, Italië.

Dit proefschrift is goedgekeurd door de promotor:
  Prof. dr. ir. L. P. Kouwenhoven

Copromotor:
  Dr. V. Zwiller

Samenstelling van de promotiecommissie:
  Rector Magnificus   voorzitter
  Prof. dr. ir. L. P. Kouwenhoven   Technische Universiteit Delft, promotor
  Dr. V. Zwiller   Technische Universiteit Delft, copromotor
  Prof. dr. M. A. G. J. Orrit   Universiteit Leiden
  Prof. dr. A. Lagendijk   Universiteit Amsterdam
  Prof. dr. P. M. Koenraad   Technische Universiteit Eindhoven
  Prof. dr. H. W. M. Salemink   Technische Universiteit Delft
  Prof. dr. K. K. Berggren   MIT, United States
  Prof. dr. ir. L. M. K. Vandersypen   Technische Universiteit Delft, reservelid
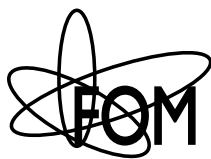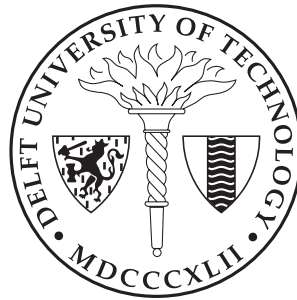
Preface

Studying physics in Pisa gave me a taste for theory but also a craving for experiments and applications. I felt the need of studying physics as a contemporary challenge, rather than a beautiful historical picture. During my master project I became more and more convinced that my future was in experimental physics and a visit to the Quantum Transport Group (QT) in Delft made it clear that this was a suitable place to cultivate my interests. Five years have passed since then and I can certainly draw a positive balance. I am very happy, in particular, for having had the chance to work on different research projects in collaboration with many people. We built a laboratory, studied different types of quantum dots and distilled in papers what we had learned. Things did not always work fine, far from that, but I am glad to see that we built something, that we, indeed, added a grain of sand to the mountain of human knowledge.

There are many people that I must thank for this five-year adventure and I will start from my supervisors who gave me the possibility to do my PhD in QT. Leo, thanks for keeping QT an interesting place where people like to discuss about physics, but not only about that. Your practical attitude and your way of asking questions definitely contribute to the success of QT. Val, thanks for your enthusiasm, your broad curiosity and your great talent in sparking collaborations. Also thank you for an amazing holiday on Mont Blanc! I wish you good postdocs, more time and success with (or without) the optics lab.

A great *thank you!* goes to our collaborators outside QT, that contributed so much to this thesis: Armando Rastelli, Fei Ding, the *equipe* of Jean-Christophe Harmand, George Cirlin, the team of Erik Bakkers and Glenn Solomon. Armando, thanks for your care in revising papers and in discussing about experiments. Fei, it was great to have you in Delft. I am sure your determination and positive attitude will bring you far. Thanks to Jean-Christophe Harmand and his team for our work on nanowires, our discussions and the hospitality in Marcoussis. George, thanks for trying to grow the *suitable sample* for us. I am very happy that the samples were suitable for something else. Erik, thanks for helping making nanowires useful tools for optics as well. Thanks also for the

particular, for being so kind as to speak French to me. Floris, Fei, Ilse, Stijn, Reinier, thank you for your help with the Dutch part of this thesis. Yuki, Angèle, Bram, Remco, Peter, thanks for your help and efficiency. Still, there should be more of you. A big thank to Ad and those who helped with the chemical room.

Special thanks go to my former housemates who have been almost a family to me for about four years. Pol, I really appreciate your curiosity and your passion for physics. Thanks for the discussions about TV series, Spanish politics, qubits, cooking, resonators and much more. I wish you good luck with your postdoc and I am looking forward to meeting you and Roser again soon. Katja, thank you for the *Feuerzangenbowle*, the many barbecues with marinated-something, your advice on propositions and, in short, for being so sensible and organized. Lan, thanks for the many – sometimes long – discussions, the carnival in Germany, some peculiar tapas on the beach, accepting to be my paranymph and, above all, for your friendship. Hannes, it was great to have you and all your instruments at the *Petteflet*. Good luck with your PhD, I am sure you will have fun.

I am happy that, in spite of the distance, I could often discuss with my sister Paola, with Annalisa and with Liliana. Annalisa, I am very grateful for your support and I wish you and Pascal good luck in Santa Cruz. Paola, *la frangine*, we had so many frank discussions. *Shukran!*, I really appreciate. I had a great time with you and Rodolfo and it was a pleasure to visit you in Paris, Venice, Damascus, Amman and Geneva. Looking forward to Tel Aviv. Liliana, thanks for the incredible holiday in India and good luck for your post PhD.

A huge *thank you!* goes to my parents for their love and support: you definitely helped me in finishing this work. I am also very grateful to my family at large, to my uncles and aunts and to my brother. Salvatore, Angelo, thanks for discussing about work with me. Thanks, Tullio, for our sometimes incoherent chatting and for being my paranymph. Finally, I want to thank Valentine for the time we spent together, for her patience, her irony and her support. I am very happy, deeply grateful and looking at the future with more confidence than ever.

<div align="right">

Umberto Perinetti
January 2011

</div>

<div align="right">

</div>

Contents

Chapter 1

Introduction

1.1 Quantum dots

Semiconductors have been used for decades for making all sort of devices like diodes, transistors, LEDs (light emitting diodes) and lasers [1]. As the technological advances in fabrication made possible to make ever pure semiconductor crystals it was also possible to study structures, made of different semiconductors, in which some carriers, electrons or holes, are confined to thin sheets (quantum wells), narrow lines (quantum wires) or confined around a point (quantum dots) [2, 3]. It was also possible to confine carriers in non simply connected regions like quantum rings.

One of the most prominent features of these structures is that the confinement strongly modifies the energy spectrum of carriers, in a way that is appreciable at the relatively high temperatures of a few Kelvin. Because of confinement, electrons in quantum dots occupy discrete energy levels, in a similar way as they do in atoms. For these reasons quantum dots are also called *artificial atoms.*

The applications of quantum dots are still mostly confined to research laboratories, but they are remarkable and often rely on the fact that quantum dots give acces to the quantum mechanical degrees of freedom of only a few carriers. Single electron transistors [4], the manipulation of one [5], or two [6] electron spins are only some examples.

Other applications of quantum dots are related to optics: some quantum dots can confine both electrons and holes in the same region, making it possible to perform, in a solid state system, similar experiments as in atoms [7, 8]. In particular, quantum dots where successfully used to produce single photons, photon pairs in an entangled polarization state and indistinguishable photons [9, 10, 11].

Two ambitious aims underlying the research on quantum dots are quantum communication and quantum computation [12, 13], i.e. exploiting the features

of quantum mechanics in order to perform some computational tasks faster than it is allowed for a classical computer. Optically active quantum dots can have applications in both quantum communication and quantum computation. Single photons or entangled photon pairs can be used as the quantum-bits (qubits) of a quantum communication protocol [14]. Also a scheme [15] was proposed to perform quantum computation with only identical photons, linear optics components and detectors. Optically active quantum dots could not only be the sources of the photons required in these protocols, they could be a useful system for implementing a quantum computer based both on fixed qubits (e.g. the spin of an electron) and *flying qubits* i.e. photons.

This thesis deals with different optical experiments on semiconductor quantum dots and quantum rings. We studied dots of different geometries and materials in order to explore their suitability as controllable sources of single photons and indistinguishable photons.

1.2 Outline of this thesis

We introduce the theoretical concepts useful to describe the studied structures in **chapter 2** and we present an overview of the techniques and the equipment we used for the measurements in **chapter 3**. More information about techniques used for a particular experiment are given in the corresponding chapters. We start our discussion about quantum dots in nanowires in **chapter 4** were a study of structural and optical properties of InP wires with InAsP inclusions is presented. A similar structure is studied in **chapter 5** were the focus is put on optical properties: on how the polarization of excitation light and photoluminescence are related and what information this gives about electron spin states in the quantum dot. We continue the study of these quantum dots in **chapter 6** where we present preliminary results on electron and hole g-factors.

The following two chapters (**chapters 7** and **8**) deal with quantum dots in layered semiconductor structures. We studied these dots in order to find a compromise between the material and geometry flexibility of quantum dots in nanowires, and a good optical quality, which, at the time, was nanowires' weak spot. In **chapter 7** we see how optically active GaAs quantum dots in AlGaAs can be designed to emit in resonance with optical transitions in a gas vapor, and we discuss one possible application of this fact. **Chapter 8** is a characterization of InAs quantum dots grown on vicinal GaAs surfaces which showed particularly narrow lines for this growth technique. This growth method allows to broaden the size range of quantum dots that can be produced making

it possible to have dots with different features of their optical spectrum. In particular, our aim was to achieve a small energy separation between the neutral exciton and biexciton transitions, a requirement for producing entangled photons with a scheme proposed by Avron et al. [16]. In the last chapters of this thesis we turn the attention to two quantum mechanical effects made accessible by semiconductor quantum rings and quantum dots respectively. **Chapters 9** and **10** present how the optical emission spectrum of a quantum ring changes as a function of an external magnetic field along the growth direction. Changes in the energy and brightness of the transitions suggest that the Aharonov-Bohm effect plays a role in determining the energy levels of a neutral exciton. As a first step towards interfering photons emitted by two quantum dots we demonstrate two-photon interference (**chapter 11**) of photons emitted by a single dot.

The material presented in some chapters was accepted for publication; in those cases the reference is indicated on the first page of the chapter.

Chapter 2

Fundamental properties
of quantum dots

U. Perinetti, M. P. van Kouwen & M. H. M. van Weert

In this chapter we discuss the fundamental properties of optically active quantum dots. First we address the properties of quantum dots as boxes for electrons and holes, using an effective mass approach. As an illustrative case we discuss the geometry and the confinement properties of quantum dots in nanowires, we then describe a standard photoluminescence experiment and the optical selection rules that apply to the studied quantum dots. We finish the chapter discussing the effect of a magnetic field on the electron and hole states and what this implies for optical properties.

2.1 Confinement

Quantum dots are nanostructures in which electrons and/or holes are confined to a small region [3]. In the case of optically active quantum dots the confinement is usually achieved by having a nanometer sized piece of low bandgap semiconductor surrounded by a higher bandgap material. In this thesis we report on different examples of such structures and we discuss here, in this chapter, the illustrative case of quantum dots in nanowires, where confinement has been achieved by introducing a short section of InAsP material in an InP nanowire. Typically, the height of the InAsP section is less than 10 nm, while the diameter is about 30 nm. See Figure 2.1a for the nanowire quantum dot geometry. Wires are grown in z-direction using the MBE and MOCVD growth techniques (chapter 4 and section 5.7). The z-axis is defined along the growth direction.

In order to calculate the energy levels of heterostructure quantum dots, an atomistic approach is common [17, 18]. In that case many-body effects of the $\sim 10^6$ atoms have to be taken into account. For fixed quantum dot sizes, the analysis is carefully done for self-assembled quantum dots [17, 18], and more recently for InAsP quantum dots in InP nanowires [19].

To have a basic idea of the influence of the quantum dot size and shape on the energy levels we do not need to resort to such complex methods: we take here an effective mass approach [20] and solve for the energy levels analytically. Assuming that the confinement potential $V(\mathbf{r})$ can be written as a product of a function V_{axial} of z and a function $V_{lateral}$ of (x, y), i.e. $V = V_{lateral}(x, y) V_{axial}(z)$, then the lateral and axial confinement problems can be treated separately. Although side-faceting may occur, resulting in hexagonal or triangular nanowire cross-sections [21], we assume, for simplicity a cylindrical cross-section throughout this chapter.
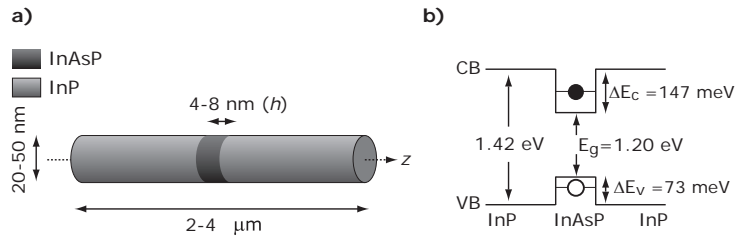
Figure 2.1: Schematics of the nanowire quantum dot geometry. (a) Typical dimensions of the nanowire quantum dots under study. (b) Band structure of an InP nanowire with an $InAs_{0.25}P_{0.75}$ quantum dot, presenting the band gap E_g, and the conduction and valence band offsets, ΔE_c and ΔE_v, respectively.

Table 2.1: Band gaps and particle effective masses for InP and InAs$_{0.25}$P$_{0.75}$ used for determining the finite well confinement energy.

	InP	InAs$_{0.25}$P$_{0.75}$
Band gap[a] (eV)	1.42	1.20
Effective mass electron[b] (m_e^*/m_0)	0.073	0.061
Effective mass heavy hole[b] (m_{hh}^*/m_0)	0.6	0.553
Effective mass light hole[b] (m_{lh}^*/m_0)	0.089	0.073

[a] Measured value for a section in a nanowire
[b] Calculated from theoretical InAs and InP bulk values

2.1.1 Confinement in the z-direction

Consider an InP nanowire with a ternary InAs$_x$P$_{1-x}$ quantum dot of height h (see Figure 2.1a). Here, x is the ternary parameter, it has a value between 0 and 1, and influences the energy gap of the ternary material InAsP. To calculate the z-direction confinement energies for electrons and holes, the band gap energy of InP (E_g^{InP}), InAsP (E_g^{InAsP}), and the relative conduction and valence band offsets, ΔE_c and ΔE_v, are required.

Bulk values for the effective masses of electrons (m_e^*), heavy holes (m_{hh}^*) and light (m_{lh}^*) holes are considered for the InP wire. We assume that the effective masses change linearly in x, from the values they have in InP to the ones they have in InAsP. The effective mass of an electron in the quantum dot is then approximated by $m_{e,InP}^*(1-x) + m_{e,InAs}^*x$. In a similar way m_{hh}^* and m_{lh}^* can be determined for the quantum dot. The origin of heavy and light holes will be discussed later in this chapter in section 2.2.2.

In table 2.1 we list the relevant effective masses and band gaps of zinc-blende[1] InP and the InAs$_{0.25}$P$_{0.75}$ quantum dot. For the band offsets we assume a 66% (147 meV) offset in the conduction band and 33% (73 meV) in the valence band, predicted for InAs/InP interfaces in the absence of strain [22]. Now, for a derivation of the one-dimensional finite well confinement energies as a function of quantum dot height h, we follow a standard textbook approach [23].

Figure 2.2 presents the resulting confinement energies for the ground state electron (E_{e0}^{conf}), heavy hole (E_{hh}^{conf}), light hole (E_{lh}^{conf}) and the first electron

---

[1]Although a wurtzite crystal structure is often observed in InP nanowires, electronic properties of this crystal phase are still unknown, except for the band gap.
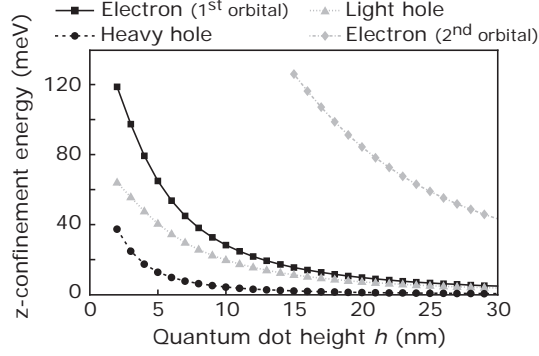
Figure 2.2: Axial confinement energies. Modeled one-dimensional finite well z-confinement energies for electrons (ground and first excited state) and holes (light and heavy) relative to the corresponding band edge, as a function of the height h of a InAs$_{0.25}$P$_{0.75}$ quantum dot. Confining potential and effective masses as presented in table 2.1.

excited state (E_{e1}^{conf}) as a function of quantum dot height. As expected, the confinement energies increase with smaller quantum dot size. In the case of $h < 17$ nm, the first electron excited state confinement energy exceeds the conduction band-offset and becomes an unbound state. For $2 < h < 17$ nm, the quantum dot contains a single z-confined electron level. In absence of strain, heavy holes have a lower confinement energy than light holes, due to the difference in effective mass. Therefore, heavy holes form the valence band ground state. For future reference, the calculated z-confinement energies are listed for quantum dots of heights $h = 4$ nm and 8 nm, respectively, in table 2.2.

Table 2.2: Confinement energies for a quantum dot height of 4 nm and 8 nm.

Quantum dot height (nm)	4	8
Electron z-conf. energy, E_e^{conf} (meV)	79	38
Heavy hole z-conf. energy, E_{hh}^{conf} (meV)	18	6
Light hole z-conf. energy, E_{lh}^{conf} (meV)	48	26

2.1.2   Lateral confinement

As described in the previous section, the quantum dot confines only the lowest orbital in z, since its height is smaller than 10 nm. However, besides the axial confinement, the (weaker) lateral confinement causes the formation of sublevels. Following the convention of atomic physics, the lowest energy sublevel is named s-shell, the first excited sublevel p-shell, and the second excited sublevel is referred to as d-shell, in optically-active quantum dots.

In order to derive the s-p-shell energy splitting E^{sp}, the radial confinement potential is assumed to be a harmonic potential. Such an assumption consists in approximating the potential to its firs relevant order and has proven reasonably good in predicting the sublevel spacings for self-assembled quantum dots [24].
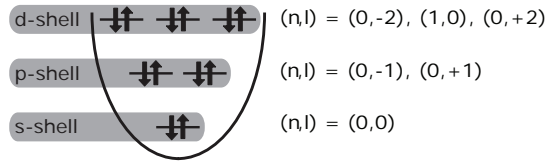
Figure 2.3: Shell model in the conduction band for a two-dimensional harmonic potential. Electron shells are labelled s, p, d, in analogy with atomic physics. The principal quantum number is indicated as n and the z-component of the angular momentum is indicated as l. Degenerate states are shown on the same line.

We model the energy levels in the nanowire by neglecting few-particle interactions and strain. In polar coordinates (r,θ), the two-dimensional harmonic potential in the conduction band is given by $V(r) = \frac{1}{2}m_e^*\omega_e^2 r^2$, in which ω_e is the conduction band harmonic oscillator frequency and m_e^* denotes the electron effective mass (table 2.1). This model can be solved analitically also in the presence of an external magnetic field leading to the well known Fock-Darwin states [25, 26]. At zero magnetic field the energies of the eigenstates $|n, l\rangle$ are:

$$E_{n,l} = (2n + |l| + 1)\hbar\omega_e, \tag{2.1}$$

where, $n = 0, 1, 2, \ldots$ is the radial quantum number and $l = 0, \pm 1, \pm 2, \ldots$ is the angular momentum quantum number of the oscillator. Note that $E_{0,0}$ corresponds to the s-shell, which (neglecting the spin) is non degenerate. The states $|0, \pm 1\rangle$ are degenerate and form the p-shell, while $|1, 0\rangle$ and $|0, \pm 2\rangle$ are degenerate and form the d-shell. When considering the twofold spin-degeneracy of each state $|n, l\rangle$ the s, p, and d-shell are, respectively, two, four, and sixfold degenerate. See Figure 2.3 for an overview.

To obtain the energy separation between the shells we assume the potential $V(r)$ at the edge of the nanowire ($r = R$, with R the nanowire radius) is limited to the band offset (ΔE_c) with InP, since during growth a thin InP shell is deposited around the wire simultaneously with growth at the catalyst particle. In that case ω_e can be derived as a function of nanowire diameter:

$$qV_c(R) = \frac{m_e^* \omega_e^2 R^2}{2} = \Delta E_c, \tag{2.2}$$

in which ΔE_c is the conduction band offset (see table 2.1). The energy levels are separated by:

$$E^{sp} = \hbar \omega_e(R) = \hbar \sqrt{\frac{2\Delta E_c}{m_e}} \frac{1}{R}. \tag{2.3}$$

A similar derivation is applicable for the valence band.

In Figure 2.4, the energy $E^{sp} = \hbar \omega(R)$ is plotted for the conduction and valence band. The conduction + valence band s-p splitting is also shown (circles). For a nanowire of 30 nm in diameter a total s-p splitting of 24 meV is predicted for the harmonic potential case. The s-p splitting according to an infinite well potential is depicted in grey diamonds for comparison. In this case, a splitting of 21 meV is predicted for a nanowire of diameter 30 nm.
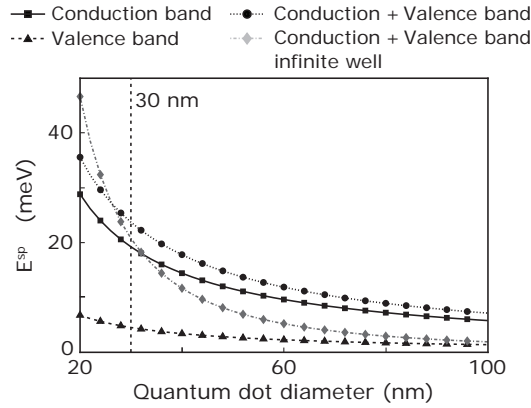
Figure 2.4: Radial confinement energies. Modeled two-dimensional harmonic potential radial confinement energies (E^{sp}) for electrons in the conduction band, holes in the valence band and the total confinement (conduction + valence band) as a function of InAs$_{0.25}$P$_{0.75}$ quantum dot diameter. The grey curve represents the total confinement for an infinite potential well.

2.2 Optical properties

2.2.1 Photoluminescence experiments

A common way to study the energies of electrons and holes in a quantum dot is by photoluminescence experiments. These consist in using laser light to excite electrons from the valence band to the conduction band of the material that surrounds the dot. In this way electron and holes are created that can be captured in the dot and relax to the respective ground states (Fig.2.5).

The main mechanisms for carrier relaxation are scattering with phonons (longitudinal acoustical and optical), the emission of far infrared photons and Auger processes [27]. Scattering with phonons is usually faster (10-100 ps) than the radiative recombination (1 ns), allowing to the carriers in the dot to relalax to the ground state before optical recombination.

Depending on the excitation power a different number of carriers can accumulate in the dot and different optical transitions can take place. In particular transitions between s, p and d shells are visible (Fig. 2.5).

2.2.2 Optical selection rules

In order to understand which transitions are visible in a photoluminescence experiment we need to look at the optical selection rules. In the dipole approximation the coupling between electron states that determines the emission of a photon is $H_I \propto \hat{\mathbf{e}} \cdot \mathbf{r}$, where $\hat{\mathbf{e}}$ is the polarization unit vector and $\mathbf{r}$ is the position operator. To appreciate the role of the envelope and Bloch wave functions in optical transitions, within the effective mass and dipole approximations, we can first consider a one dimensional case (Fig. 2.6). In this case the optical transition operator H_I is proportional to the position x and only couples states of different parity. For a symmetric confinement the ground state envelope functions for the electron and the hole have the same parity (they are both even functions). The optical transition between the electron and hole states is allowed because of the parity of the parity of the Bloch functions, which are even for the conduction band and odd for the valence band.

We can extend these considerations to the three dimensional case by taking into account the angular momentum $\mathbf{L}_{band}$ associated to different bands and by considering thatthe total angular momentum should be preserved in the electron-hole recombination and photon generation. Let us first recapitulate the quantum states, and in particular the angular momentum and spin in our quantum dot.

The angular momentum operator $\mathbf{J} = \mathbf{L_{band}} + \mathbf{L} + \mathbf{S}$ consists of the spin
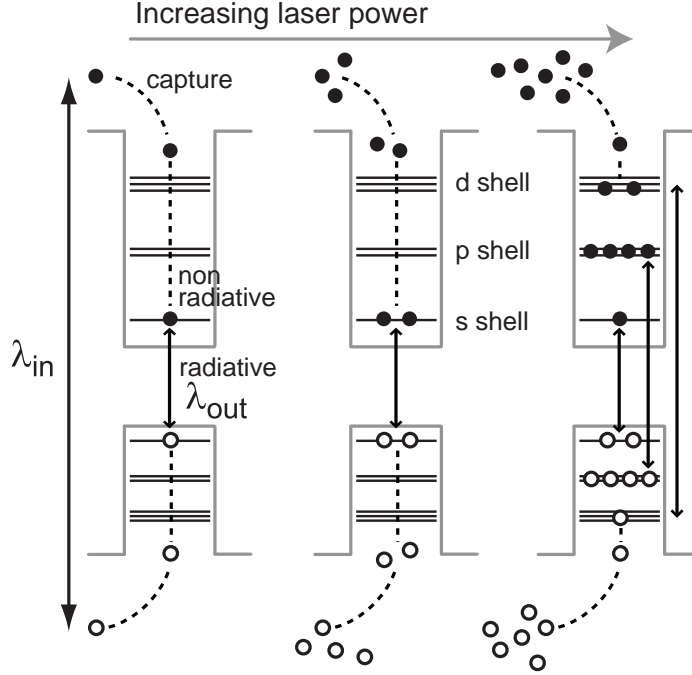
Figure 2.5: Photoluminescence experiment. A laser excites electrons (solid circles) across the bandgap of the host material leaving holes (hollow circles) in the valence band. Electron and holes relax to low energy states in the dot and recombine giving photons of energy λ_{out}. For low laser power only one transition, between s-shells is visible. As the laser power is increased more electron and holes accumulate in the dot and transitions between other shells (p, d, etc.) are observed.

angular momentum, $\mathbf{S}$, the angular momentum $\mathbf{L_{band}}$ carried by the Bloch waves, and the orbital angular momentum $\mathbf{L}$ associated to the single particle envelope functions. The corresponding quantum numbers for the relevant operators J, J_z, and S are denoted j, j_z, and s, respectively.

In bulk InP, the electrons at the conduction band minimum have zero angular momentum ($\mathbf{L_{band}} = 0$) since they occupy an s-like orbital. The total angular momentum, $\mathbf{J} = \mathbf{L_{band}} + \mathbf{S}$, is found by including the spin of the electron, $S = \frac{1}{2}$. Thus, the projections of the angular momentum, j_z, can take the values of $\pm\frac{1}{2}$.

In contrast, holes at the top of the valence band occupy a p-like orbital, corresponding to $L_{band} = 1$. Including the spin of the hole, $S = \frac{1}{2}$, there are six possible states for the hole in the valence band. For the two states, for which $J = \frac{1}{2}$ holds, the corresponding projections along z are $j_z = \pm\frac{1}{2}$. For the states where $J = \frac{3}{2}$, the four possible values are $j_z = \pm\frac{1}{2}$, and $\pm\frac{3}{2}$. The $J = \frac{1}{2}$ states are split from the $J = \frac{3}{2}$ states by spin-orbit interaction, where the two $J = \frac{1}{2}$ states,

referred to as split-off bands, are typically a few hundreds of meV's below the $J = \frac{3}{2}$ states, and can be neglected [22]. The $J = \frac{3}{2}$ states can be separated in the light-hole band ($j_z = \pm\frac{1}{2}$), and the heavy-hole band ($j_z = \pm\frac{3}{2}$). In bulk, the heavy- and light-hole bands are degenerate. Confinement lifts the degeneracy, due to different effective masses [2]. As already mentioned in section 2.1.1, the light-hole states are typically tens of meV's below the heavy-hole states. As a result, the lowest energy optical transition is that between a $j_z = \pm\frac{1}{2}$ electron and a $j_z = \pm\frac{3}{2}$ hole. Interaction between the sublevels can lead to heavy-light hole mixing. The strength of this intersub-band mixing depends on the difference in effective mass along and across the symmetry axis. Furthermore, the strength of the mixing increases with decreasing dot size [28]. Strain, however, can lead to a weakening of the intersub-band interaction. In the following, the intersub-band mixing will be neglected, which is motivated by experiments showing clean selection rules for holes in self-assembled quantum dots, such as Ref. [29]. In Figure 2.7a, the different energy levels for the electrons and holes are depicted schematically.
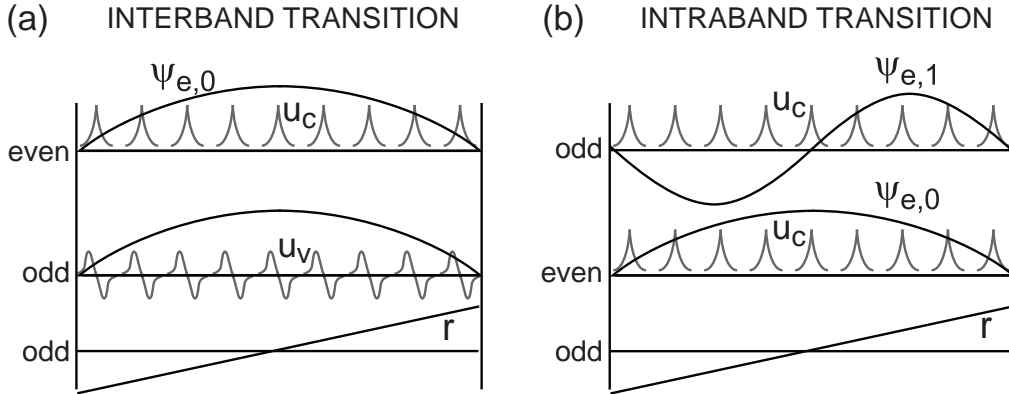
Figure 2.6: Interband and intraband transitions in a quantum dot (**a**) The different symmetry of Bloch waves for the conduction and valence bands allows optical transitions between the electron s-shell and the hole s-shell. (**b**) Intraband transitions between electron p- and s-shells are allowed because of the different symmetry of the electron envelope functions $\psi_{e,0}$, $\psi_{e,1}$

Since a circularly polarized photon carries angular momentum of $\pm\hbar$ and has zero spin, the following selection rules should be obeyed for a transition between two electronic states:

$$\begin{aligned} \Delta j_z &= \pm 1, \\ \Delta s &= 0. \end{aligned} \tag{2.4}$$

These constraints distinguish the *bright* exciton states, $|M\rangle = |-\frac{1}{2}\rangle_e + |+\frac{3}{2}\rangle_h = |+1\rangle$ and $|M\rangle = |+\frac{1}{2}\rangle_e + |-\frac{3}{2}\rangle_h = |-1\rangle$, from the *dark* exciton states, $|M\rangle = |+\frac{1}{2}\rangle_e + |+\frac{3}{2}\rangle_h = |+2\rangle$ and $|M\rangle = |-\frac{1}{2}\rangle_e + |-\frac{3}{2}\rangle_h = |-2\rangle$. We call *bright* the exciton states in which an optical recombination is possible and *dark* those that cannot decay optically. These transitions are depicted in Figure 2.7a.

So far, we have discussed the ground states of the dot. We can extend this to the excited states using the shell model, introduced in the previous section 2.1. We do this for the heavy holes, since these transitions have the lowest energy. The shell model is taken into account by the orbital angular momentum of the particle L, originating from the Fock-Darwin states [24]. Since $\Delta j_z = \pm 1$ is fulfilled by the L_{band} part in J, the change in orbital angular momentum should vanish $\Delta l = 0$. Hence, only transitions between conduction and valence band states with the same values for l are optically allowed. In Figure 2.7b the optically allowed transitions in the different shells are shown schematically.
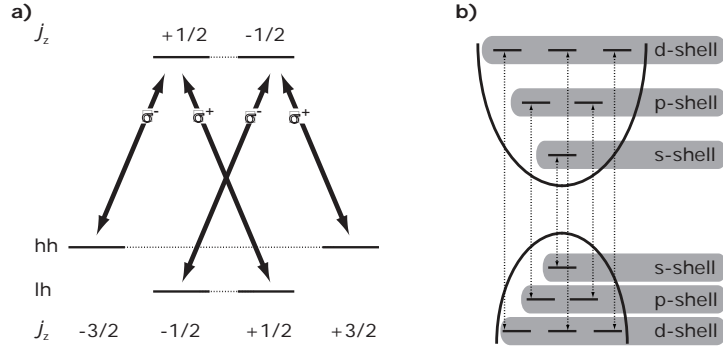
Figure 2.7: Allowed optical transitions in an ideal quantum dot. (a) Optical selection rules applied to ground state transitions including spin degeneracy. (b) Energy levels in conduction and valence band. The allowed optical transitions ($\Delta l = 0$) are indicated by vertical arrows.

The energy levels and selection rules described above apply to the ideal situation of a circularly symmetric dot embedded in a homogeneous and isotropic medium. In practice, asymmetry in the quantum dot (*e.g.* geometrical or crystallographic) leads to an anisotropic exchange splitting of the neutral exciton state. Furthermore, some of the dots studied here are embedded in a nanowire structure, which affects the far field properties of the dot. These effects will be elucidated in the following.

2.2.3 Anisotropic exchange splitting

In an external magnetic field B the exciton transition exhibits a Zeeman splitting. This is treated in section 2.3. However, even without applying an external magnetic field a splitting can arise from the exchange interaction, which couples the spins of the electron and hole. This exchange interaction consists of a short range and a long range contribution. We will discuss the short range term below. The long range term can be included, by adding its contribution to the short range interaction [30]. The Hamiltonian for the electron-hole exchange interaction is given by

$$H_{exchange} = - \sum_{i=x,y,z} \left(a_i J_{h,i} \cdot S_{e,i} + b_i J_{h,i}^3 \cdot S_{e,i} \right), \tag{2.5}$$

where J_h and S_e are the spins of the heavy-hole and electron, respectively, and the coefficients a_i and b_i are material-dependent. This interaction energy is more than a factor of ten smaller than the splitting between heavy and light holes, hence the light holes are neglected. We can construct a matrix representation of the Hamiltonian in equation 2.5, by using the bright and dark exciton states $(|+1\rangle|-1\rangle|+2\rangle|-2\rangle)$ as a basis[30]:

$$H_{exchange} = \frac{1}{2} \begin{pmatrix} \delta_0 & \delta_1 & 0 & 0 \\ \delta_1 & \delta_0 & 0 & 0 \\ 0 & 0 & -\delta_0 & \delta_2 \\ 0 & 0 & \delta_2 & -\delta_0 \end{pmatrix}. \tag{2.6}$$

The three coefficients in this representation are $\delta_0 = 3/2 \left(a_z + 9/4 b_z \right)$, $\delta_1 = 3/4 \left(b_x - b_y \right)$, and $\delta_2 = 3/4 \left(b_x + b_y \right)$. The coefficients a_i in the linear term of equation 2.5 are larger than the coefficients b_i in the cubic term. Hence, the splitting between the bright and dark excitons, δ_0, is the largest. For a perfectly symmetric quantum dot $(b_x = b_y)$ δ_1 vanishes. In this case, $|+1\rangle$ and $|-1\rangle$ are degenerate eigenstates of $H_{exchange}$. When the dot is not perfectly symmetric, the bright excitons will hybridize: the two eigenstates are symmetric and anti-symmetric linear combinations of the two ± 1 excitons, split by δ_1, the anisotropic exchange splitting. In contrast, the dark ± 2 excitons always mix, regardless of the quantum dot symmetry. The splitting between the two new eigenstates (linear combinations of the ± 2 exciton states) is δ_2.

The long range interaction introduces an extra splitting between the two bright excitons, and has the same form as the short range term. Therefore, it can be taken into account by adding the corresponding energies to the off-diagonal terms that mix the ± 1 states [30]. The long range term vanishes for $b_x = b_y$, similar as the short range term.

To summarize, when the dot is symmetric around z, the ± 1 exciton states are (degenerate) eigenstates of the $H_{exchange}$ Hamiltonian, and the two oppositely circularly polarized photon states, $\sigma\pm$, can couple to the dot. When the dot has no rotational symmetry, the (non-degenerate) eigenstates of $H_{exchange}$ are the symmetric and anti-symmetric linear combinations of the ± 1 exciton states. In this case, two orthogonally *linearly* polarized photon states of different energies can couple to the dot.

The above is valid for a neutral exciton X^0, with one electron and one hole. For a singly charged exciton X^{1-} (X^{1+}) the electron-hole exchange interaction vanishes, since the two electrons (holes) in the excited state form a singlet with zero spin. For the biexciton state $2X^0$ the exchange interaction also vanishes, because the two electrons and the two holes both form singlet states. The final state of the biexciton transition, however, is the X^0 state, and exhibits an anisotropic exchange splitting. Hence, in luminescence both X^0 and $2X^0$ transitions show (opposite) exchange splitting. This is shown schematically in Figure 2.8a.

When the optical axis is aligned with the symmetry axis z, the two linear polarizations of the hybridized exciton state can both be observed, since both polarizations are orthogonal to the optical axis. When the optical axis is aligned perpendicular to the symmetry axis, as is the case for the lying nanowire geometry, both polarization states are projected on the polarization perpendicular to the optical axis. Hence, the two exciton states are indistinguishable by polarization, or, in the special case where one of the polarization states is aligned with the optical axis, only one of the hybridized exciton states is observable [31]. This is shown schematically in Figure 2.8b.

The anisotropic exchange splitting has important technological implications. In 2000, Benson *et al.* [32] proposed a scheme for generating entangled photon pairs using the exciton-biexciton cascade. However, the anisotropic exchange splitting prevents measuring polarization entanglement, since in that case the photons can be distinguished in energy. Recent calculations show that nanowire quantum dots show no anisotropic exchange splitting due to their highly symmetric shape (circular or hexagonal) and crystal structure (wurtzite, $\langle 111 \rangle$) [19].

2.3 Quantum dots in a magnetic field

In this section we discuss the influence of a magnetic field B on the exciton emission. We consider different geometries: first the conventional Faraday and Voigt configurations in which the magnetic field is, respectively, parallel or orthogonal to the (approximate) rotational symmetry axis of the quantum dot. We then
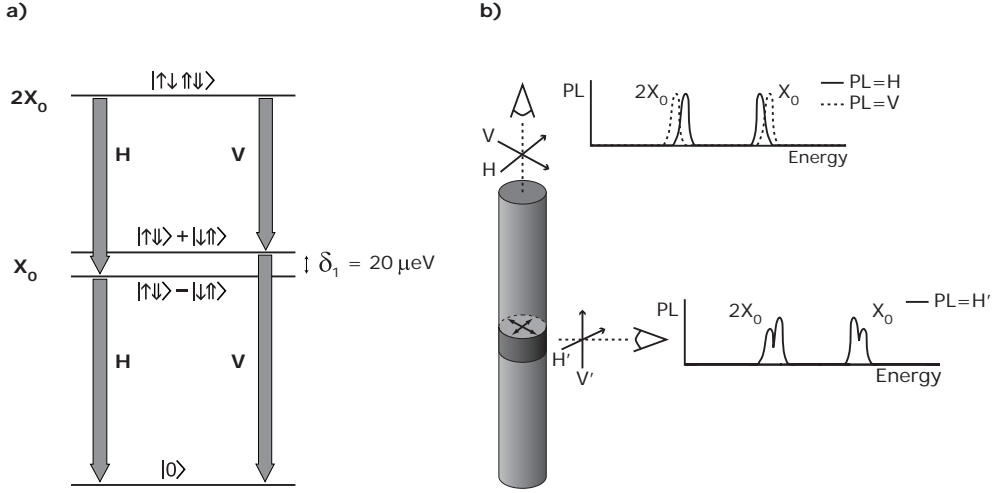
Figure 2.8: Electron-hole exchange interaction for the exciton and biexciton.
(**a**) Energy diagram of the exciton (X_0) and biexciton ($2X_0$) cascade. The exciton state is split by δ_1 due to anisotropic electron-hole exchange interaction. These states are the ground states for the biexciton transition, which as a result shows an opposite splitting with respect to the exciton transition. The arrows denoted with H and V represent horizontally and vertically polarized emission, respectively. (**b**) Effect of the alignment of the optical axis on the observation of the emission from the hybridized (bi-)exciton states. When the optical axis is aligned parallel to the confinement axis, both hybridized (bi-)exciton states can be distinguished by polarization (H and V). When the optical axis is aligned perpendicular to the confinement axis the two hybridized states are indistinguishable by polarization (H' and V').

discuss an intermediate case with the magnetic field is at an angle θ with the symmetry axis. In all these cases the optical axis coincides with the symmetry axis of the studied dot. The focus of these paragraphs is the Zeeman interaction from the magnetic field acting on the spins of the electron-hole pair, and the polarization of the emitted photons. In addition to the Zeeman interaction the B-field induces a diamagnetic shift. This is explained in the last paragraph of this section.

2.3.1 Faraday configuration

The Hamiltonian of the electron and hole spins in a magnetic field is as follows [30]:

$$H_{Zeeman} = \mu_B \sum_{i=x,y,z} \left(g_{e,i} S_{e,i} - g_{h,i} J_{h,i} \right) B_i, \tag{2.7}$$

where μ_B is the Bohr magneton, g_e and g_h are the electron and hole Landé g factors, and $B = (B_x, B_y, B_z)$ is the applied magnetic field. Note that the g-factors are anisotropic in general: their values are dependent on crystal axis orientation, confinement, strain; quantities which are all anisotropic.

In the Faraday configuration a magnetic field is applied parallel to the symmetry axis, $B = (0, 0, B_z)$. In this case the Hamiltonian 2.7 in the basis of bright and dark exciton states
$(|+1\rangle |-1\rangle |+2\rangle |-2\rangle)$, is as follows:

$$H_{Zeeman} = \frac{\mu_B B}{2} \begin{pmatrix} +\left(g_{e,z}+g_{h,z}\right) & 0 & 0 & 0 \\ 0 & -\left(g_{e,z}+g_{h,z}\right) & 0 & 0 \\ 0 & 0 & -\left(g_{e,z}-g_{h,z}\right) & 0 \\ 0 & 0 & 0 & +\left(g_{e,z}-g_{h,z}\right) \end{pmatrix}. \tag{2.8}$$

Since rotational symmetry is preserved in this configuration, the matrix has diagonal form and no (extra) mixing between the basis states occurs. It is convenient to introduce the exciton g-factor $g_{exc} = g_e + g_h$. The two Hamiltonians 2.6 and 2.8 can now be summed to obtain the total Hamiltonian for a neutral exciton X^0. At low magnetic fields the exchange interaction dominates, and the emitted photons will have linear polarizations due to hybridization of the ± 1 and ± 2 states, as explained in section 2.2.3. At higher magnetic fields the diagonal matrix elements, which are proportional to B, start to dominate, and the exchange can be neglected. In this case, the ± 1 and ± 2 excitons are eigenstates of the Hamiltonian with different energies. As a result, the emitted photons will have circular polarization, according to the spin $M = \pm 1$ of the exciton. Furthermore, the energy difference between the two bright exciton states is proportional to the magnetic field, with a proportionality factor of $g_{exc}\mu_B$. The same holds for the dark excitons. A schematic of the resulting energy levels of an exciton in a B-field using Faraday configuration is shown in Figure 6.1a. For a charged exciton X^{1-} the exchange interactions are absent and the Hamiltonian simplifies to equation 2.8, a linear dependence.

2.3.2 Voigt configuration

In the Voigt configuration, the magnetic field is aligned perpendicular to the symmetry axis, $B = (B_x, B_y, 0)$. For simplicity, we choose $B_y = 0$. The matrix form of Hamiltonian 2.7 becomes in this case:

$$H_{Zeeman} = \frac{\mu_B B}{2} \begin{pmatrix} 0 & 0 & g_{e,x} & g_{h,x} \\ 0 & 0 & g_{h,x} & g_{e,x} \\ g_{e,x} & g_{h,x} & 0 & 0 \\ g_{h,x} & g_{e,x} & 0 & 0 \end{pmatrix}. \tag{2.9}$$
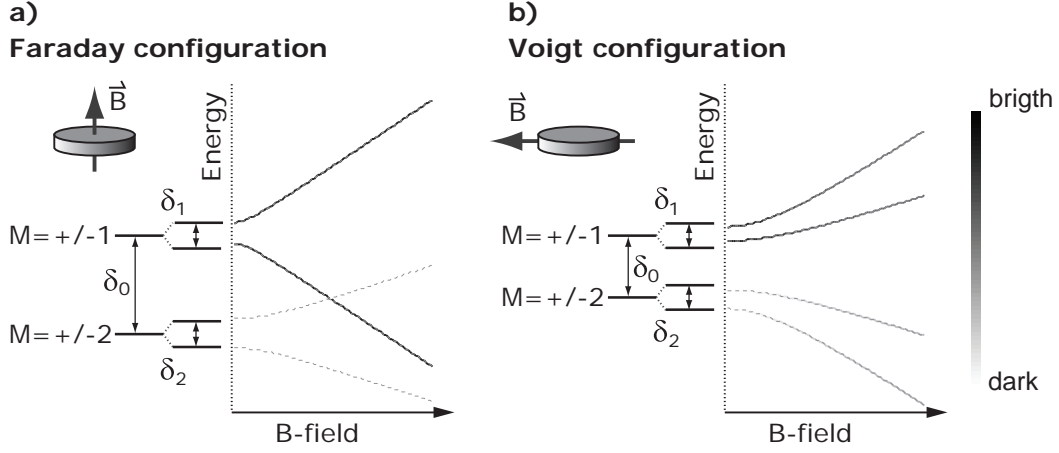
Figure 2.9: Neutral exciton levels as a function of magnetic field. Due to exchange interaction the dark ± 2 excitons are split from the bright ± 1 excitons by δ_0. Both bright and dark exciton pairs hybridize due to the anisotropic exchange interaction. (**a**) With increasing magnetic field B in the Faraday configuration the bright and dark exciton pairs split. When the magnetic energy $g_{exc}\mu_b B$ is stronger than the exchange energies δ_1, δ_2, a linear dependence of the exciton splitting on the B-field is found. (**b**) With increasing magnetic field B in the Voigt geometry, the bright and dark exciton pairs split. With increasing magnetic field, both bright and dark excitons split and mix, since the B-field destroys the circular symmetry.

In contrast to the Faraday configuration, this matrix does not have diagonal form and causes the mixing of bright and dark excitons. As a result, the optical transition of the dark excitons become weakly allowed and are observable in luminescence. A schematic of the resulting neutral exciton energy levels in Voigt configuration is shown in Figure 6.1b. For a charged exciton X^{1-} the dependence is similar, except that the exchange interactions vanish. This implies that the eigenstates of the system will be a superpositions of a dark and a bright state with amplitudes of equal absolute value. For this reason the X^{1-} single emission line will split into four equally bright emission lines even at small magnetic fields.

2.3.3 Diamagnetic shift

A magnetic field does not only couple to the spin of the particles, but also to their orbital motion. To show this we write the kinetic term of the single particle Hamiltonian, including the minimal coupling term:

$$K \;=\; \frac{1}{2m}\left(\mathbf{p} + e\mathbf{A}(\mathbf{r})\right)^2, \qquad \mathbf{A} = \frac{\mathbf{B} \times \mathbf{r}}{2} \tag{2.10}$$

$$=\; \frac{\mathbf{p}^2}{2m} + \frac{eB}{2m}l_z + \frac{e^2}{8m}B^2. \tag{2.11}$$

The second term gives the coupling of the electron (hole) magnetic moment to the B field for states with non zero angular momentum of the envelope function. The third term is quadratic in B and the energy shift caused by this term is called diamagnetic shift. It influences all the states and is the dominant term in the case of a neutral exciton.

It is customary to write the exciton energy as [33]:

$$E_{exc}(B) = E_{exc}(0) + \beta B + \gamma B^2 + O(B^3). \tag{2.12}$$

It is immediate to see that the diamagnetic coefficient, in first order perturbation theory, is given by:

$$\gamma \sim \frac{e^2}{8}\left(\frac{1}{m_e^*}\langle r_e\rangle^2 + \frac{1}{m_{hh}^*}\langle r_{hh}\rangle^2\right), \tag{2.13}$$

in which $\langle r_e^2\rangle$ and $\langle r_{hh}^2\rangle$ are the expectation values of the electron and hole squared radii over the unperturbed states. Measurement of the diamagnetic coefficient γ can be used to estimate the quantum dot size, as we do in Chapter 5 and compare this value with TEM.

Chapter 3

Setup and measurement techniques

U. Perinetti & N. Akopian

The large majority of the measurements presented in this thesis are on the photoluminescence (PL) of single cold nanostructures. Most of them were taken with a low temperature micro-PL setup which is, essentially, a cryogenic microscope combined with a set of lasers, to excite the sample, and a spectrometer and other instruments, to analyze the resulting PL. The main components of this setup and their operation are described in this chapter.

3.1 Low temperature microscope

Our cryogenic microscope was developped starting from a commercial setup by Attocube (attoCFM I), consisting in a liquid helium bath cryostat and an insert. The insert is a metal cylinder containing the sample together with an objective lens and inertial nano-positioners. It is filled with helium at a pressure of a few millibar in order to have thermal contact between the sample and the liquid helium bath.

We replaced the optics provided with the system with an assembly of our design which is more suitable for our measurements and, in particular, provides better collection efficiency (by replacing a single lens with an objective), highly improved stability and ease of alignment. A schematic representation of the setup is shown in Figure 3.1.

Laser light is guided to the setup through a single mode optical fiber. After being turned into a collimated beam it is directed to the sample via a motorized neutral density (ND) filter and a non polarizing beam splitter (BS) which allows to split off part of the laser light to measure the laser power. The same beam splitter is used to collect 90% of the PL that exits the insert. Different filters (colored glass, dielectric-stack) are used to block the laser light reflected from the sample.

Inside the insert the excitation laser is focussed on the sample by an objective with a numerical aperture of 0.85. The same objective collects the photoluminescence from the sample. Inertial piezoelectric positioners (Attocube) allow to displace the sample in three directions in steps smaller than 100 nm allowing to accurately position a quantum dot in the focal point of the objective.

In order to image the sample surface directly, without scanning the sample, we added a white light source and a camera to the setup. A pellicle beam splitter on a motorized flip mount (see Fig. 3.1) directs the white light into the insert and collects the reflected light. Due to the length of the insert and to the small working distance of the objective ($\approx$ 0.2 mm) the field of view is limited to a circle with a diameter of about 13 μm. The optical window (W) reflects a sizeable fraction of the white light which overlaps in space with the reflection from the sample. In order to prevent this stray reflection from reaching the imaging camera we use light linearly polarized in one direction and detect light polarized in the orthogonal direction (see the polarizing beam splitters, PBS, in the schematics).

A photograph of the actual setup is shown in Fig. 3.2. It should be noted that the optical components outside the cryostat are mounted on a small optical table sitting on the top plate of the cryostat. The table rests on precise kinematic
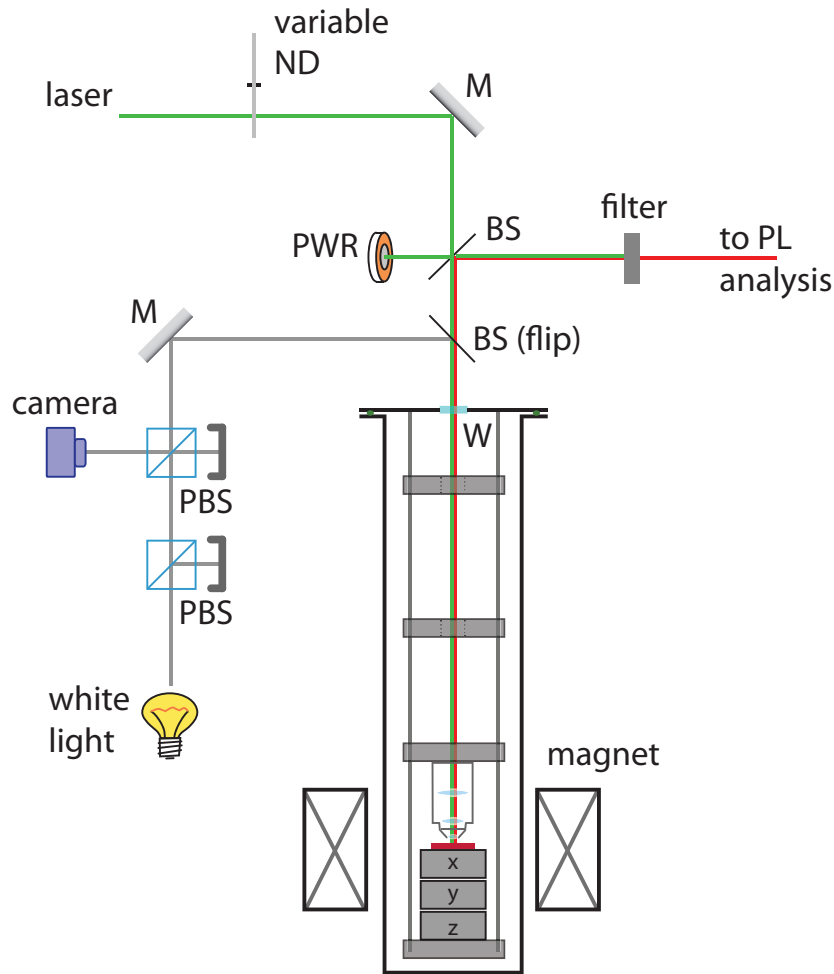
Figure 3.1: Schematics of the low temperature microscope. The excitation laser is attenuated and focussed on the sample. The photoluminescence is collected by the same objective. A white light source and a camera allow for direct imaging of the sample (M, mirror; BS, beam splitter; PBS, polarizing beam splitter; ND, neutral density filter)

mounts that allow for it to be removed and placed back with small changes in the alignment. A small misalignment can easily be compensated for: we use an iris at the top of the cryostat as a reference for the beam position and we make sure that the beam enters the objective along the optical axis. This is done by looking at the laser spot on the sample with a CCD camera.
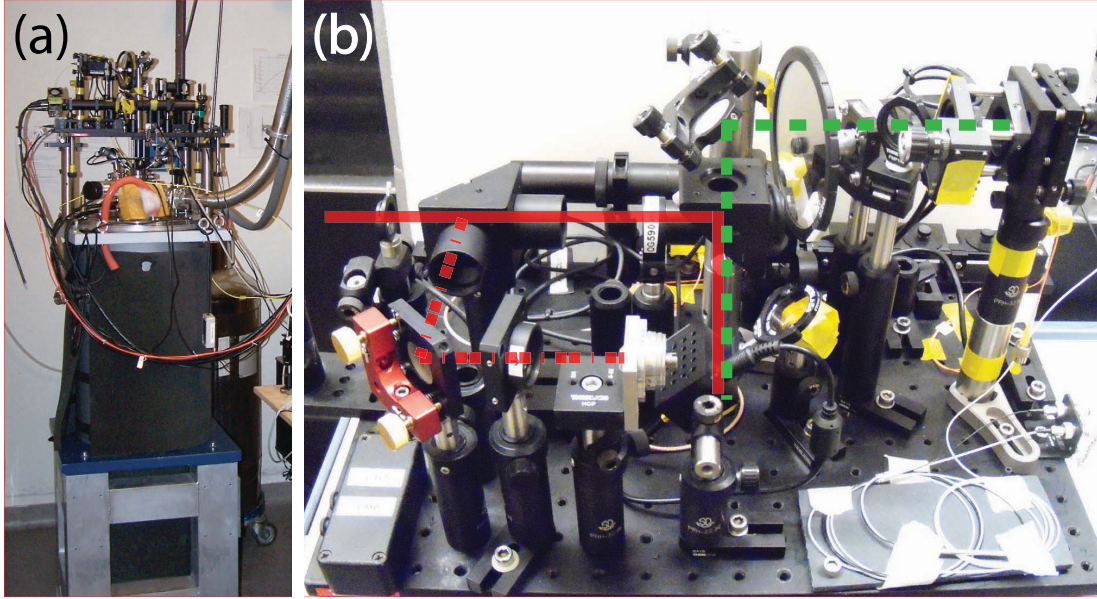
Figure 3.2: Low temperature microscope. (a) Cryostat with, on top, a small optical table. **(b)** Detail view of the optical table in (a). The excitation path (dashed line) and two alternative detection paths (solid and dot-dash lines) are marked.

3.2 Photoluminescence analysis

3.2.1 Simple spectroscopy

For most of the experiments presented in this thesis we used a commercial spectrometer by Acton (SP2750). This is a Czerny-Turner monochromator with a dispersion length of 75 cm equipped with three diffraction gratings with 150, 600, and 1800 groves per mm respectively. For the detection we used a back illuminated CCD detector (SPEC-10:100BR) by Princeton Instruments) which, in combination with the 1800 l/mm grating gives a spectral resolution of about 30 μeV. For some of the measurements we used an old 1 m spectrometer by Jobin-Yvon (THR1000) that we refurbished ourselves by changing the motion controller and by equipping it with a 1200 gr/mm holographic grating.

3.2.2 Fabry-Perot

In order to achieve a better resolution than the one of our spectrometers, we used a Fabry-Perot (FP) cavity formed by two flat dielectric mirrors 1 inch in diameter and separated by a few millimeters. The cavity was kept in place by a structure developed at Leiden University: the position of one mirror was controlled by three

micrometer screws while the other mirror could be displaced and tilted at small angles by means of three piezo actuators. We used a 650 nm laser for a rough alignment of the cavity based on interference fringes. We then used a 780 nm laser in combination with a photodiode at the F-P output in order to optimize the parallelism of the two mirrors and achieve a good finesse: we scanned the cavity observing the transmission peaks measured by the photodiode and we used an offset voltage on the piezos to tune the cavity. We achieved a finesse of about 100, corresponding to an energy resolution of about 2 μeV.
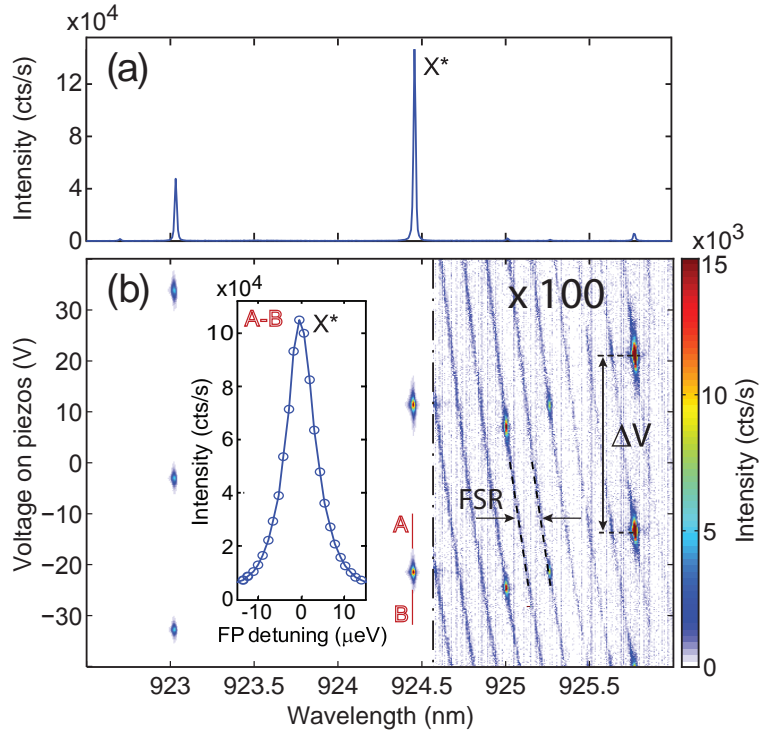
Figure 3.3: Fabry-Perot measurement. (a) Spectrum of a self assembled InAs quantum dot under non-resonant ($\lambda = 650$ nm) laser excitation. (b) Photoluminescence filtered by a Fabry-Perot (FP). The color map represents spectra as a function of the FP detuning. The different FP modes are clearly visible in the closeup (x100). The **inset** shows a vertical section of the colormap giving a high resolution measurement of one of the QD transitions, X^*

The basic idea of a FP measurement is that the FP can be used as a very narrow tunable filter interposed between a light source and a detector. If we restrict ourselves to a single mode, a spectroscopy measurement consists in scanning this mode over a given energy range and register the intensity on the detector. This gives a spectrum with a resolution corresponding to the spectral width of the FP mode.

The FP has, however, multiple modes, equally spaced in energy by what is called the free spectral range (FSR). It is therefore necessary to add some extra filtering or energy selectivity in order to perform a measurement with a single mode as described above. This is done, in practice, by using a spectrometer as detector: since the FSR of our FP is much bigger than the spectrometer resolution we can independently measure light which is in resonance with different FP modes.

This is convenient not only because it allows to do spectroscopy of different lines at the same time, but also because it offers a direct way for calibrating the F-P measurement. From a measurement like Fig. 3.3(b) we can determine the FSR and the mode detuning as a function of the piezo bias.

3.2.3 Polarization tomography

In order to identify some of the transitions in a PL spectrum, it is useful to know what is the polarization state of photons emitted at a given energy. The density matrix representing the state of these photons can be reconstructed measuring the PL intensity I_j for different polarization states $j = H, V, D, A, R, L$ which are respectively horizontal, vertical, diagonal and antidiagonal linear polarizations, and right and left circularly polarizations. From these measurements the density matrix can be calculated [34] as

$$\hat{\rho} = \frac{1}{2} \sum_{i=0}^{3} S_i \hat{\sigma}_i, \tag{3.1}$$

where $\hat{\sigma}_i$ are the Pauli matrices and S_i are the Stokes parameters, which can be written as functions of the measured intensities:

$$\begin{aligned}
S_0 &= 1, \\
S_1 &= \frac{I_D - I_A}{I_H + I_V}, \\
S_2 &= \frac{I_R - I_L}{I_H + I_V}, \\
S_3 &= \frac{I_H - I_V}{I_H + I_V}.
\end{aligned} \tag{3.2}$$

We used liquid crystal variable retarders (LCVRs) and a polarizing beam splitter (PBS) in order to select the required polarization states. The setup is sketched in Fig. 3.4. For different retardation values of the two liquid crystal
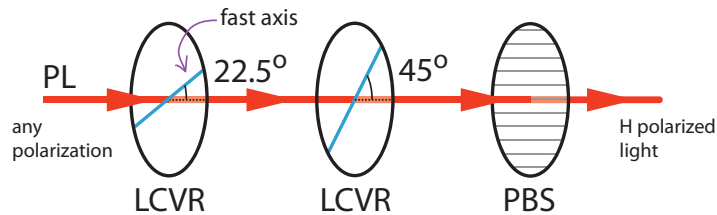
Figure 3.4: Polarization tomography setup. Different settings of the liquid crystal variable retarders (LCVRs) allow to transform different polarization states into horizontal polarization (H)

retarders, different polarization states are transformed into the H state transmitted by the polarizing beam splitter. The retarder settings corresponding to measuring different polarizations are summarized in Table 3.1.

A good features of this measurement setup is that, although we are probing different polarization components of the emitted PL, the light that arrives to our detector has always the same polarization (H in the drawing). In this way we don't suffer for the intrinsic polarization sensitivity of our detector. The absence of moving parts and the reduced switching times make us prefer this arrangement over movable $\lambda/2$ and $\lambda/4$ waveplates.

Table 3.1: LCVR settings for measuring different polarizations.

Polarization	Retardation LCVR 22°30'	Retardation LCVR 45°
V	0	$\lambda/2$
D	$\lambda/2$	0
A	$\lambda/2$	$\lambda/2$
R	0	$\lambda/4$
L	$\lambda/2$	$\lambda/4$

The retardation in LCVRs is controlled by the amplitude of an oscillating voltage applied across the thickness of the retarder. This retardation strongly depends on the wavelength making it necessary to calibrate the retarders at different wavelengths. We do this with a setup [Fig. 3.6(a)] that does not require reference wave plates, making the calibration more reliable. The working principle of this setup is that the power measured at the power meter (PWR) changes as a function of the retardation introduced by the LCVR [Fig. 3.6(b)]. We can take the cases of zero retardation and $\lambda/2$ retardation as illustrative cases. For zero
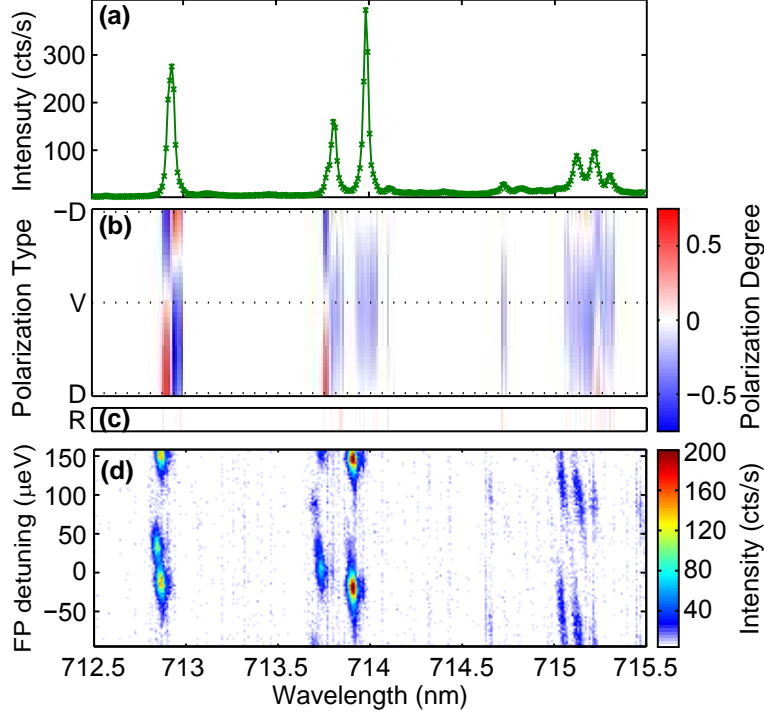
Figure 3.5: Polarization and Fabry-Perot measurement. (a) Spectrum of a GaAs quantum dot in AlGaAs under non-resonant laser excitation. **(b,c)** Degree of polarization as a function of wavelength and the type of polarization. This is defined for a given polarization P as the difference between the probability of measuring $|P\rangle$ and the probability of measuring it's orthogonal $|\bar{P}\rangle$. The colormap is plotted only for wavelengths at which the signal excedes 5% of the maximum. **(d)** Fabry-Perot measurement of the same PL. Peaks that are too close together to be resolved by the spectrometer are visible in the FP measurement, at wavelengths were the polarization measurement suggested the presence of multiple peaks.

retardation, horizontally (H) polarized light reaches the mirror and is reflected back. This light is still H polarized and it will not be reflected at the beam splitter. The situation is quite different when the retardation is $\lambda/4$ and it is convenient to indicate the polarization with the electric field unit vector $\hat{e} = \cos\alpha\,\hat{x} + e^{i\phi}\sin\alpha\,\hat{y}$ with $\hat{x}$ along the slow axis of the retarder and $\hat{y}$ along the fast axis. After the beam splitter the polarization is given by $\hat{e} = \frac{1}{\sqrt{2}}(1,1)$ (horizontal) and passing through the retarder it becomes $\hat{e} = \frac{1}{\sqrt{2}}(i,1)$. After reflection at the mirror the propagation direction and the electric field are inverted, but the electric field is still turning in the same direction (looking from the PBS to the mirror), so it's polarization is still $\hat{e} = \frac{1}{\sqrt{2}}(i,1)$. After passing again through the retarder the

light is polarized along $\hat{e} = \frac{1}{\sqrt{2}}(-1, 1)$, that is vertically polarized. It is therefore completely reflected at the beam splitter and goes to the power meter.
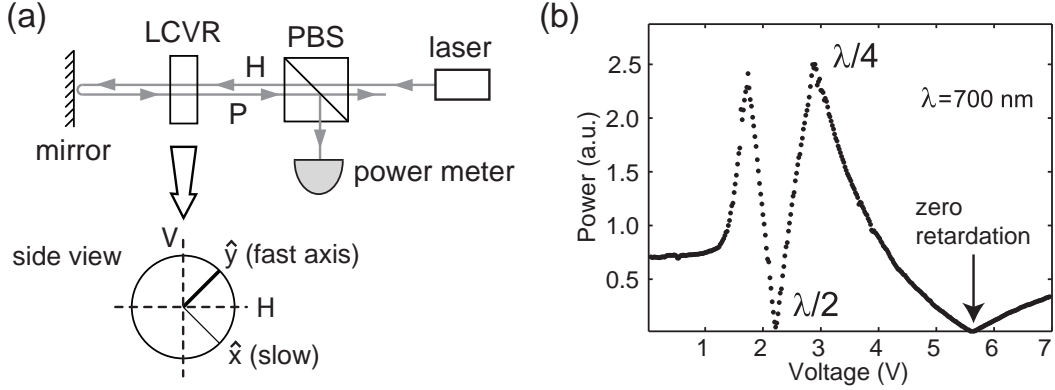
Figure 3.6: Calibration of a liquid crystal variable retarder. (a) Calibration setup. **b** Example of calibration measurement for a 700 nm laser. Voltages at which the retardation is $\lambda/2$ and $\lambda/4$ are indicated.

An example of polarization tomography measurement is shown in Figure 3.5(b,c) where the polarization data are represented in a colormap as a function of wavelength and polarization state. For a given polarization $|P\rangle$, the color represents a Stokes-like parameter $S_P = \frac{I_P - I_{\bar{P}}}{I_P + I_{\bar{P}}}$, where $|\bar{P}\rangle$ is the state orthogonal to $|P\rangle$. Measuring spectra at different polarizations allows to resolve different lines that would merge together in an ordinary (polarization averaged) spectrometer measurement [Fig.3.5(a)] and that require the use of a Fabry-Perot [Fig.3.5(d)] to be resolved in energy alone.

3.2.4 Time resolved measurements

We used a Hamamatsu streak camera (C5680-24) and avalanche photodiode modules (PerkinElmer, SPCM-AQRH series) in order to take time resolved measurements of the studied photoluminescence. The streak camera is most suitable when an overview of the evolution in time of a photoluminescence spectrum is necessary. It allows for an excellent time resolution of a few picoseconds. We used APDs in order to take correlation measurements and also to measure lifetimes. An example of this is shown in chapter 11 where more details about this measurement technique are given. It is worth mentioning here that, although the streak camera time resolution is much better than the one of our APDs. The APDs can be the measurement system of choice when low noise is necessary and

when only a few parameters are needed to model the measured time evolution (e.g. lifetime in chapter 11).

Chapter 4

Growth and characterization of InP nanowires with InAsP insertions

M. Tchernycheva, G. E. Cirlin, G. Patriarche, L. Travers,
V. Zwiller, U. Perinetti & J.-C. Harmand

We report on the fabrication by Au-assisted molecular beam epitaxy of InP nanowires with embedded InAsP insertions. The growth temperature affects the nucleation on the nanowire lateral surface. It is therefore possible to grow the wires in two steps: to fabricate an axial heterostructure (at 420 °C), and then cover it by a shell (at 390 °C). The InAsP alloy composition could be varied between $InAs_{0.35}P_{0.65}$ and $InAs_{0.5}P_{0.5}$ by changing the As to P flux ratio. When a shell is present, the InAsP segments show strong room-temperature photoluminescence with a peak wavelength tunable from 1.2 to 1.55 μm by adjusting the As content. If the axial heterostructure has no shell, luminescence intensity is drastically reduced. Low-temperature micro-photoluminescence performed on isolated single wires shows narrow peaks with a line width as small as 120 μeV.

4.1 Introduction

Free standing semiconductor nanowires (NWs) attract an increasing attention due to their emerging applications to nano-scale devices such as photo-emitters, photo-detectors, transistors, etc [35]. A commonly used technique for NW fabrication relies on the catalytic mechanism generally referred to as vapor-liquid-solid (VLS) growth [36], whereby liquid particles are formed by alloying of the catalyst with the semiconductor constituents. The one dimensional growth is promoted by the fast local precipitation of adsorbed species at the liquid-semiconductor interface under the droplets. The VLS technique allows to fabricate heterostructures in both axial and radial directions and to intentionally dope the NWs [37, 38]. The catalytic growth has successfully been applied to synthesize NWs of almost all III-V semiconductors using metalorganic vapor phase epitaxy, chemical beam epitaxy, or molecular beam epitaxy (MBE) growth techniques. A large effort has been devoted to the fabrication of NWs of In(As)P, which is a key material for high-speed electronics [39, 40] and for near infrared light emission/detection applications [41, 42, 43]. The band gap of InAsP can be tailored from 3.5 μm to 0.92 μm by adjusting the alloy composition and, in particular, can cover the 1.3-1.55 μm wavelength range of technological importance for optical telecommunications.

In this letter, we report on the synthesis of InAsP insertions in InP nanowires by Au-assisted molecular beam epitaxy (MBE). We show that the growth temperature allows us to control the nucleation on the NW lateral surface and provide a method to embed InAsP insertions into InP shells. When a shell is present the resulting heterostructures demonstrate strong room-temperature photoluminescence with a peak wavelength tunable from 1.2 μm to 1.55 μm by adjusting the As content. If the axial heterostructure has no shell, luminescence intensity is drastically reduced. The micro-photoluminescence performed at 10 K on isolated single wires show narrow peaks with a linewidth as small as 120 μeV.

4.2 Fabrication

NWs were grown on InP (111)B substrates in an MBE system equipped with solid sources supplying In atoms, and cracker As and P sources to produce dimers. The substrate surface was first deoxidized at 530 °C, then a 100 nm thick InP buffer layer was grown to achieve atomically flat surface. A total amount of Au equivalent to 1 nm layer was deposited under phosphorus flux at 420 °C using an Au effusion cell installed directly into the III-V growth chamber. The substrate temperature was then set to the desired value for the growth. This procedure

results in the formation of droplets containing Au alloyed with the substrate constituents. The typical distribution of droplet sizes ranges between 30 nm and 40 nm.After this stage, the NW growth was initiated by opening the In shutter. For all samples the nominal growth rate (i.e., the growth rate on a clean and Au-free InP surface) was fixed at 0.2 nm/s. For InP/InAsP/InP heterostructure formation, the growth started with 20 min of InP, then the As source was opened for 30 s in order to form an InAsP segment. The As to P flux ratio was varied from sample to sample to investigate different alloy compositions. The growth was completed with 5 min deposition of InP. We did not perform any growth interruption at the heterointerfaces. The resulting morphology of NW ensembles was investigated by scanning electron microscopy (SEM). The crystallographic structure was analyzed in a transmission electron microscope (TEM) equipped with an energy dispersive X-ray (EDX) spectrometer for composition measurements. For TEM characterization of the NWs, they were either prepared on their substrate by thinning the sample by mechanical polishing and Ar ion milling or separated from their substrate and picked up by touching the substrate with Cu TEM grid with a lacey carbon film. The photoluminescence (PL) of NW ensemble was investigated using the following setup. The sample was excited at normal incidence with 532 nm line of frequency doubled NdYag laser at low excitation density (0.1 W/cm^2). The luminescence signal was dispersed with a 0.46m focal length spectrometer and was detected with a nitrogen-cooled Ge photodetector. For micro-PL measurements, NWs were removed from their substrate, dispersed on a SiO2/p-Si substrate with the average density of 0.1 NW per m2 and placed in a continuous LHe flow cryostat. The light from a semiconductor based laser ($\lambda = 532$ nm) was focused by microscope objective (NA = 0.75) to a spot size of 1 μm allowing to excite a single NW. The signal was collected with the same objective, dispersed with a 0.75m spectrometer and detected with a linear array of InGaAs detectors.

First, we investigated the temperature domain where binary InP NWs can be formed. A series of 7 samples was grown at temperatures ranging from 330 °C to 440 °C with a constant growth time equal to 20 min. The NW formation was observed only in a relatively narrow temperature window, between 350 °C and 420 °C. The growth at 330 °C produced only a rough two-dimensional layer that covered the deposited Au catalyst. At 440 °C, the catalyst droplets were found segregating on the growing surface without giving rise to NW formation. In the intermediate range of temperature, NW growth is induced by diffusion of adatoms from the surface to the catalyst droplets and by their subsequent precipitation at the catalyst-semiconductor interface [44]. This mechanism includes the adatom migration along the facets of the NWs, as soon as the latter start to grow. The

highest average NW growth rate of 0.7±0.25 nm/s was observed for 420 °C. This is 3.5 times greater than the nominal growth rate. The competing growth rate at the bottom surface, which occurs in parallel with the growth of NWs, is 0.15 nm/s.

For temperatures below 410 °C, NWs develop a pencil-like shape. The diameter in the lower part of the wire is two-three times larger than that of the catalyst particle and the NW end is tapered. This morphology indicates that at low temperatures, concomitantly with the vertical growth governed by the catalyst, the nucleation on the lateral facets also takes place. This phenomenon occurs when the mean diffusion length of species on the lateral NW facets becomes shorter than the NW height. In this case, most of In adatoms cannot reach the catalyst droplets. Instead, the species can nucleate on the NW sidewalls giving rise to a significant lateral growth. As suggested by Chen et al. [45], this growth on the sidewalls may occur in a layer by layer fashion to minimize the steps at the sidewalls surface. As a result, the top of the wires develops tapering to recover the smaller radius of the catalyst particle. On the other hand, one must consider that because of the design of the MBE machine, the molecular beams are not ideally normal to the substrate surface. The incident angles are typically 75° (i.e., a significant part of flux can directly impinge the NW sidewalls). This provides additional species for the step flow of the lateral growth, as well as for maintaining a nonzero axial growth rate, even when the NW length is above the mean adatom diffusion length. These phenomena can explain why along most of their length, the NW have a constant radius, whatever this length is.

To reduce the lateral growth, temperature must be raised to increase the adatom diffusion length. At temperatures higher than 410 °C, InP NWs present cylindrical shape with the diameter equal to that of the catalyst. This means that by raising the substrate temperature it is possible to switch from the mixed axial/lateral growth to almost pure axial growth. For heterostructure formation, two temperatures corresponding to the two morphologies of InP NWs discussed above were chosen: 390 °C and 420 °C. Fig.4.1(a) shows the SEM cross-sectional image of typical InP/InAsP/InP NWs grown at 390 °C. The resulting NW height is about 1 μm, the diameter varies from 50 to 80 nm. As seen in Figure 4.1a, the NW cross-section has a hexagonal shape with six facets normal to the [0-11] substrate directions. The InAsP insertion has little influence on the NW morphology, the NWs present the typical pencil-like shape observed in binary InP NWs grown at this temperature. When the growth proceeds at 420 °C [Fig.4.1(b)], the NWs keep a cylindrical shape with 30-40 nm diameter equal to that of the catalyst droplets, a sign that lateral growth is inhibited.

In a third sample, we have intentionally promoted the lateral growth by de-

46
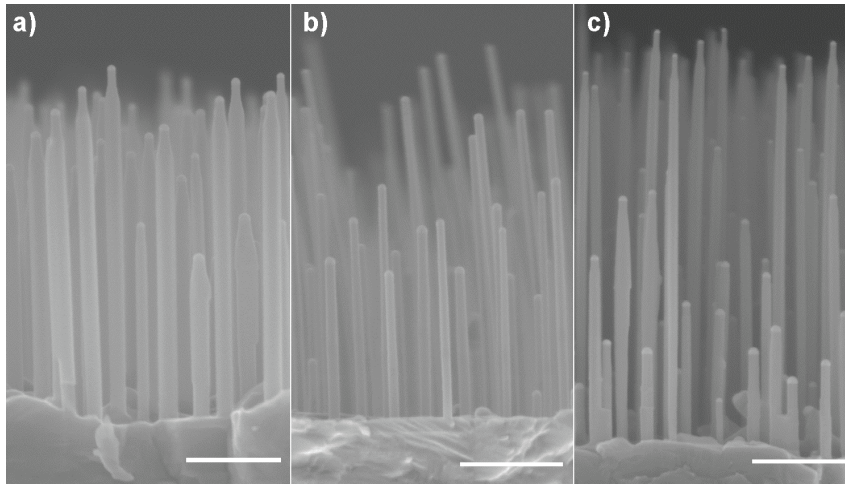
Figure 4.1: Cross-sectional SEM images of InP/InAsP/InP NWs grown a) at 390 °C, b) at 420 °C and c) at 420 °C overgrown with InP at 390 °C. The scale bar corresponds to 0.4 μm.

creasing the temperature after the InAsP insertion. Fig. 1 c) presents a SEM image of these InP/InAsP/InP NWs that were grown at 420 °C until the formation of InAsP segments was completed. The last 5 min of InP growth were performed at 390 °C. The resulting NW diameter (40-55 nm) is larger than that of the catalyst, especially for long wires, confirming that lateral growth took place. The size, shape, crystalline structure and composition of InAsP segments grown at different temperatures were studied by TEM. Fig. 4.2(a) shows the TEM image of InP/InAsP/InP NW ensemble grown at 390 °C. The pencil-like morphology is clearly seen. The NW crystalline structure is wurtzite, as commonly observed for VLS grown III-V wires [46]. The viewing direction is oriented parallel to <2-1-10> zone axis of the NWs in order to reveal the stacking faults. The InP parts of the NWs presented less than 1 stacking fault per 500 nm of length. However, in the InAsP insertions, stacking faults appeared systematically.Different results were reported by Minot et al., who observed more stacking faults in InP parts of NWs than in InAsP insertions. Stacking faults and changes in crystal structure from sphalerite to wurtzite are widely observed in III-V NWs. They represent one of the major problems whose origin is still to be clarified. The supersaturation of the III-V constituents in the catalyst phase is probably a key factor. This supersaturation is indeed intimately dependent on the gas-phase conditions, which can strongly vary between growth techniques. In the present heterostructures, switching on and off the P flux is likely to be responsible for transient supersaturation conditions, resulting in stacking faults at proximity of

the interfaces. It is important to notice, that stacking faults were the only defects present in the structure. No dislocations were observed despite a large misfit (up to 1.6%) between the InAsP insertion and the InP NW lattice parameters. This is consistent with recent calculations showing that the critical thickness of a mismatched layer, i.e. the thickness beyond which interfacial dislocations appear, is larger for a NW than for a two-dimensional layer [47].
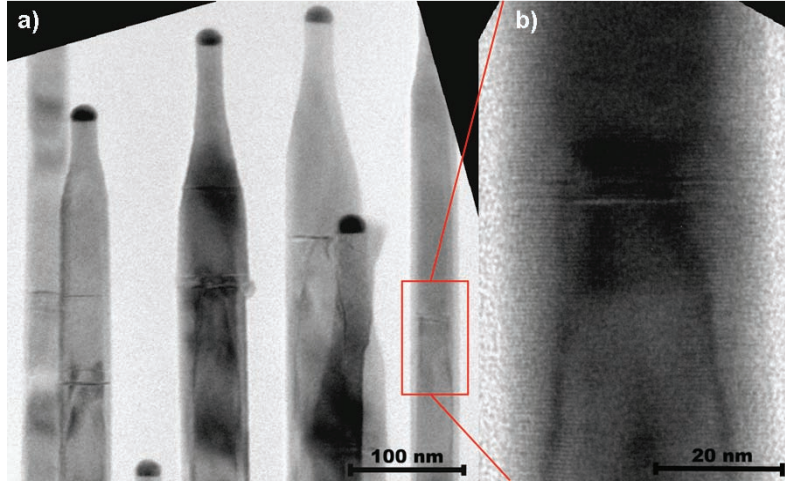
Figure 4.2: a) TEM image of the InP/InAsP/InP NW ensemble grown at 390 °C, b) high-resolution TEM image of the InAsP insertion showing 0002 lattice fringes.

Fig. 4.2(b) presents a high magnification image of an InAsP segment. The small difference between the factors of structure of InP and InAsP explains the weak contrast observed in the high resolution TEM image and makes it difficult to clearly visualize the InAsP segment. Indeed, the contrast is mainly due to the deformation related to the mismatch between the two materials. The strain between InP and InAsP induces a deformation of the atomic planes near interfaces, which locally changes the Bragg condition and thus introduces an additional contrast in the images allowing to locate the interfaces. To further enhance this strain-induced contrast, the orientation of the NWs was tilted by 2° around the [0001] direction from the <2-1-10> zone axis. Fig. 4.3 displays an InAsP insertion observed in these conditions, together with a schematic drawing explaining the insertion location. The atomic planes cannot be resolved in that case, but the strain field clearly reveals the interface positions. The segment length and diameter are 27 nm and 26 nm, respectively. As expected, the InAsP segment is laterally covered with an InP shell formed during the subsequent InP growth. This shell is 7-nm-thick. It is noteworthy, that a dark region also exists in the NW part below the InAsP insertion: during the catalyzed growth of this segment, a thin layer of InAsP was also deposited on the sidewalls of the

pencil-like end of the InP host NW. This dark region [seen in both Fig.4.2(b) and Fig. 4.3] reproduces the tapered end of the InP NWs grown at 390 °C.
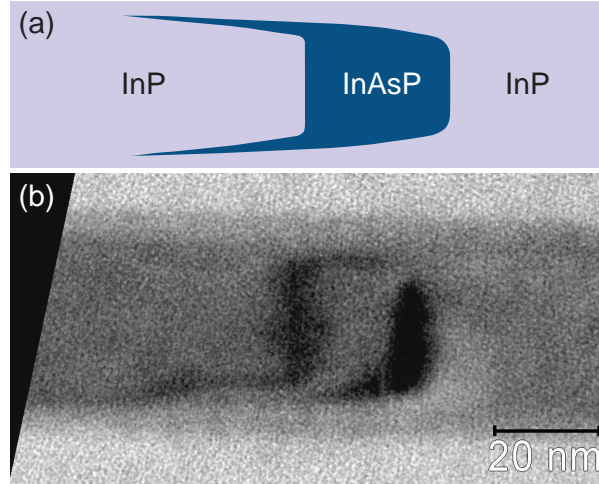
Figure 4.3: (**a**) Schematic drawing showing the insertion shape. (**a**) TEM image of InAsP insertion. The orientation of the NW is tilted by 2° around [0001] direction away from the <2-1-10> zone axis, which explains the asymmetry of the deformation contrast around the InAsP segment. (The NW growth direction goes from left to right.)

The EDX spectroscopy was systematically used to determine the composition of InAsP insertions. The measured value was corrected for the presence of InP shell of known thickness and then averaged over several NWs. The average composition was $InAs_{0.35}P_{0.65}$ for samples grown with As to P flux ratio equal to 1 and $InAs_{0.5}P_{0.5}$ for As/P=1.5. However, important composition fluctuations from wire to wire up to 10% were observed. Size and composition fluctuations from wire to wire can be due to the initial distribution of catalyst particle diameters, as well as their relative position on the surface. The diameter can affect the NW growth rate and its composition; however, experimentally the composition fluctuations were not found to be correlated with the NW diameter. It is possible that shadowing effects, determined by the NW heights and their position relative to each other, lead to significant variations of the effective fluxes impinging the NW sidewalls. This could explain the fluctuations of InAsP insertion composition, as well as the variation of the InP shell thickness.

We have shown that the growth at 390 °C favors the formation of an InP shell around the InAsP segment, but it also produces a thin InAsP foil which extends below the heterointerface. It will be shown below that the InP shell is favorable for the emission properties [48]. However, the presence of the foil is undesirable, as it modifies the shape of the InAsP insertion and makes difficult the precise control of its thickness. The InAsP foil can be almost suppressed by

using a higher growth temperature for InP/InAsP part of the wire. Then the InP shell can be formed by lowering the temperature after the InAsP insertion. Figure 4.4 shows the TEM image of the InAsP segment synthesized at 420 °C and overgrown by InP at 390 °C during 5 min [SEM image of this sample is shown in Fig.4.1(c)]. The length and diameter of the inserted InAsP segment are 32 nm and 27 nm, respectively. The length of the InAsP foil is strongly reduced and it is clear that the wire end was cylindrical during the growth of the InAsP insertion. The segment presents flat interfaces and is laterally covered with a 10 nm thick InP shell.
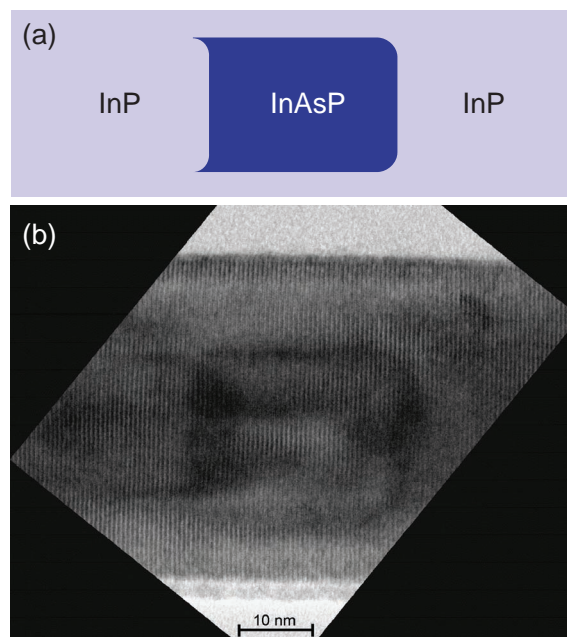
Figure 4.4: (**a**) Schematic drawing showing the insertion shape. (**b**) TEM image of InAsP insertion formed at 420 °C and overgrown with InP at 390 °C. (The NW growth axis is directed from left to right.)

4.3 Macro-Photoluminescence

The macro-PL measurements were performed on the NW ensembles grown at different temperatures. For samples grown at 390 °C and thus having an InP shell around the InAsP insertions, the luminescence spectra show two peaks (Fig.4.5). The high energy peak, situated around 1.35 eV at 300 K with a linewidth of about 150 meV, has the same position in all the samples. The peak energy corresponds to the bulk InP band gap and should mainly originate from the two dimensional InP buffer layer with a possible contribution from InP NWs. The large broadening

may be explained by a residual concentration of As in InP. The low energy peak is ascribed to the luminescence of the embedded InAsP segments. To ascertain that this peak does not originate from the emission of the two-dimensional layer, which can still grow between the NWs, we have removed all the NWs from the surface using an ultrasonic bath. After this treatment, the PL spectrum showed only the short wavelength peak; this excludes the possibility of the emission of two-dimensional InAsP layer. The PL spectra for NW heterostructures grown at 420 °C and overgrown with InP at 390 °C look similar to those of samples grown at 390 °C. However, for samples grown entirely at 420 °C only the high energy peak at 1.35 eV is present, no emission from the InAsP insertions is observed. This should be related to the suppression of the lateral growth at high temperature. The InP shell acts as an energy barrier that confines the carriers in the InAsP insertion and prevents their diffusion to the NW surfaces. When the InP shell is suppressed, the fast recombination of photogenerated carriers via surface states might hinder the PL emission from InAsP insertions. In addition, the oscillator strength of the exciton is much lower in a shell-free structure because the strain inhomogeneities tend to spatially separate electrons and holes [49]. The InP shell limits the strain relaxation of InAsP insertions, resulting in a better overlap of carrier wave functions. Fig.4.5 shows the room-temperature PL spectra of two samples grown at 390 °C with InAsP insertions synthesized at different As to P flux ratio. By changing the As to P flux ratio from 1 to 1.5, the peak emission energy was tuned from 1.025 eV (1.2 μm) to 0.8 eV (1.55 μm). This demonstrates the potential of the InP/InAsP/InP heterostructures for the fabrication of emitters in the telecommunication wavelength range (1.3-1.55 μm). The InAsP peak has an inhomogeneous broadening of 100150 meV, which should be related to the wire-to-wire composition fluctuations of the InAsP alloy. The room temperature band gap energies for the observed alloys $InAs_{0.35}P_{0.65}$ and $InAs_{0.5}P_{0.5}$ in the zinc-blend phase are 0.98 eV and 0.828 eV, respectively [50]. Taking into account the uncertainty on the band gap of wurtzite material and the composition fluctuations, the agreement with the observed peak energies is good. It is noteworthy, that the As/P incorporation ratio for MBE-grown NWs is different from the case of CBE. For InAsP NWs grown at 390 °C with tertiarybutylarsine to tertiarybutylphosphine ratio exceeding 50%, the InAsxP1-x alloy contains more than 80% of As [51].
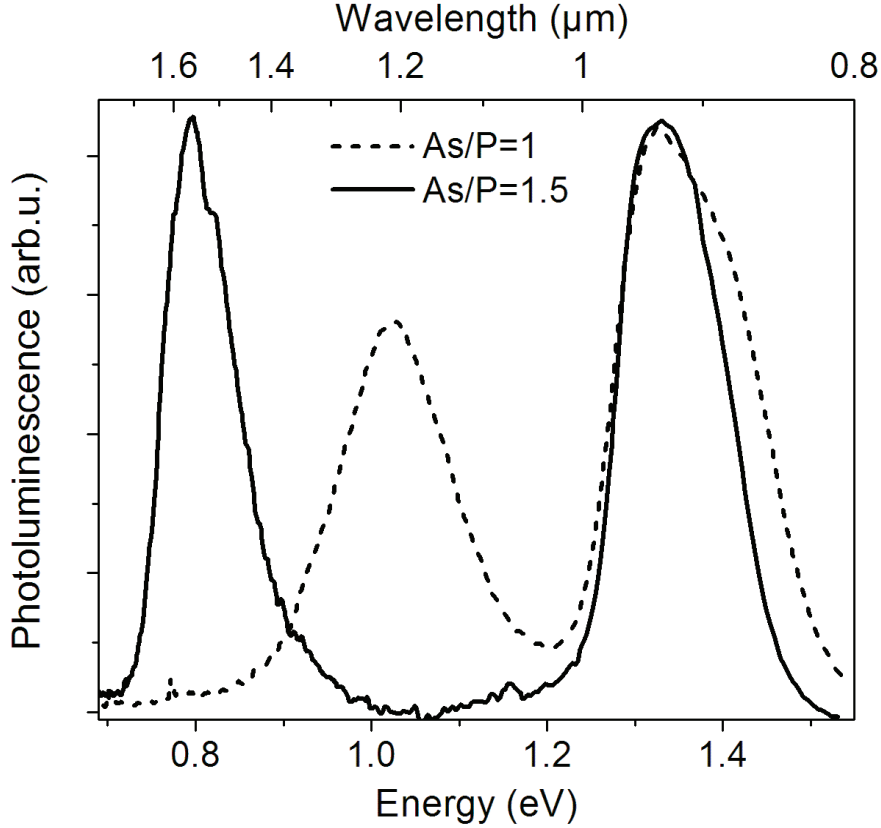
Figure 4.5: Room temperature PL of InP/InAsP/InP NWs grown at 390 °C with As to P flux ratio equal to 1 (dashed line) and to 1.5 (full line).

4.4 Low temperature micro-PL

Finally, we have performed low temperature micro-PL measurements on NWs grown at 390 °C containing two InAsP insertions of different lengths (growth time of 30 s and 45 s). Fig. 4.6 presents the PL spectrum of an individual NW measured at 10 K with 23 W/cm^2 excitation density. Two sharp lines attributed to the emission of the InAsP insertions are observed at 1.401 μm and 1.412 μm with a full width at half maximum (FWHM) as small as 120 μeV (0.19 nm). The small observed FWHM might be a signature of a quantum-dot-like confinement in InAsP insertions. The linewidth can be expected to be even narrower if we succeed to fabricate smaller InAsP insertions: in the present samples, the sizes of the insertions are larger than the Bohr exciton radius, and quantum confinement should be weak. The effective confining potential is probably reduced by the effect of internal electric field (spontaneous and piezoelectric) that builds up in these heterostructures, since the NWs are oriented along the polar ¡0001¿ direction.

In conclusion, we have fabricated 27-30 nm high InAsP insertions in InP
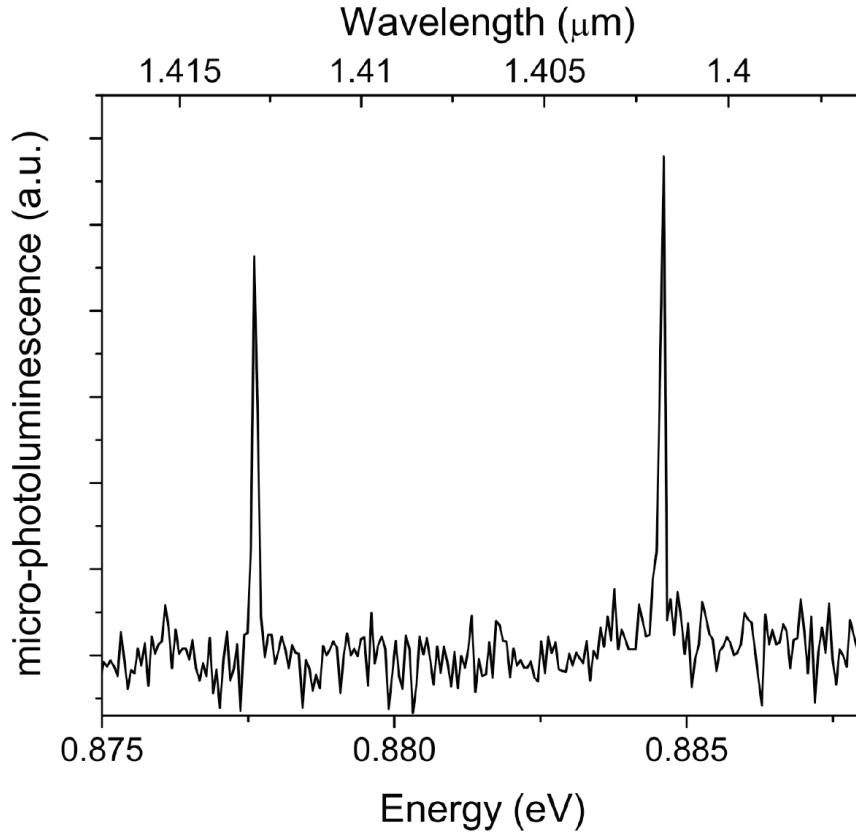
Figure 4.6: Micro-photoluminescence spectrum at 10 K of an individual NW containing 2 InAsP insertions of different lengths.

nanowires by Au-assisted MBE. The wire shape was shown to change from pencil-like for 390 °C growth to cylindrical for 420 °C growth. The alloy composition was adjusted between $InAs_{0.35}P_{0.65}$ and $InAs_{0.5}P_{0.5}$ by changing the As to P flux ratio. The presence of InP shells around the InAsP insertions is important to observe efficient PL emission. In that case, the InAsP insertions show room temperature photoluminescence peaked in the 1.2-1.55 μm wavelength range. The micro-photoluminescence from isolated nanowires shows narrow lines with full width at half maximum as small as 120 μeV. Acknowledgements The financial support of PNANO Filemon35 project, SANDiE European project and that of different RFBR grants is acknowledged.

Chapter 5

Selective excitation and detection of spin states in a single nanowire quantum dot

M. H. M. van Weert, N. Akopian, U. Perinetti, M. P. van Kouwen,
R. E. Algra, M. A. Verheijen, E. P. A. M. Bakkers,
L. P. Kouwenhoven & V. Zwiller

We report exciton spin memory in a single $InAs_{0.25}P_{0.75}$ quantum dot embedded in an InP nanowire. By synthesizing clean quantum dots with linewidths as narrow as about 30 μeV we are able to resolve individual spin states at magnetic fields of order 1 Tesla. We can prepare a given spin state by tuning excitation polarization or excitation energy. These experiments demonstrate the potential of this system to form a quantum interface between photons and electrons.

5.1 Introduction

The unprecedented material and design freedom makes semiconducting nanowires very attractive for novel opto-electronics [52, 53, 54, 55]. Quantum dots incorporated in nanowires enable experiments on both quantum optics [48, 56, 57] and electron transport [58]. This system has the potential to form a quantum interface between these separate fields of research. A crucial element for such interface is control over the spin of an exciton by means of photon polarization. Optical spectra of such nanowire quantum dots, however, have so far been hampered by broad linewidths, insufficient for identifying quantum states. Here, we demonstrate clean $InAs_{0.25}P_{0.75}$ quantum dots embedded in InP nanowires with excellent optical quality. Narrow linewidths enable us to selectively excite and detect single exciton spins. We control spin excitation by the polarization or the energy of the excitation light. The dots exhibit exciton-spin memory demonstrating that nanowires are a viable alternative to the system of self-assembled dots with new design options to interface single photon [59, 60] with single electron devices [61, 5].

Photoluminescence (PL) from homogeneous nanowires [62, 63] and from quantum dots (QDs) embedded in nanowires is highly linearly polarized for light emitted perpendicular to this 1D geometry [41, 64]. This forms an important obstacle for controlling the spin states of excitons for which circularly polarized light is needed. Circular polarization requires the light to be precisely aligned along the nanowire axis, since nanowires are circularly symmetric around this axis. Here we report such a study on as-grown, vertical nanowires standing parallel to our optical axis. We demonstrate full optical access to the spin states of individual excitons by means of right and left circularly polarized photons.

Exciton spin states have been studied extensively in self-assembled quantum dots [65]. Quantum dots in nanowires are a promising alternative to self-assembled dots when it comes to more complex circuits. For instance, multiple dots are naturally aligned in nanowires [21]; heterostructure dots can be connected to gate-defined dots [66]; and circuits of dots can be integrated with *pn*-junctions to allow for electroluminescence and photocurrent experiments. Also local gating of heterostructure dots in nanowires has become possible with recently developed wrap-around gates [67, 68, 69]. These promises motivate the development of clean nanowire quantum dots where cleanliness is measured as a narrow linewidth in the optical spectra. Initial optical studies of nanowire quantum dots reported linewidths of order meV [48, 56, 57], which is a thousand times broader than expected for the natural linewidth (*i.e.* the inverse radiative lifetime of about 1 ns). Such broad lines hampered resolving individual spin states.

Here we report on clean nanowire quantum dots with optical linewidths of tens of μeV; *i.e.* sufficiently sharp for measuring spin states above a magnetic field of ~ 1 Tesla.

5.2 Quantum dot characterization

We grow $InAs_{0.25}P_{0.75}$ quantum dots embedded in InP nanowires (see methods [21, 70, 71]. Figure 5.1a shows an image of our sample with bright spots from the nanowires. The typical distance between the nanowires is larger than our spatial resolution (0.6 μm), enabling us to select an individual dot. The dots are typically 10 nm high with a diameter of 30 nm and are surrounded by a thin shell of InP (see Figure 5.1[b]).
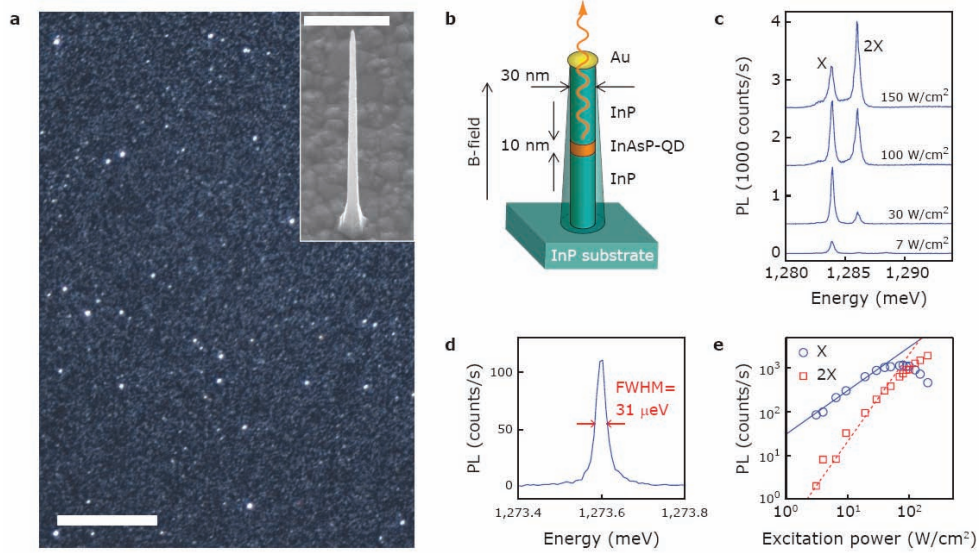
Figure 5.1: Structural and optical properties of nanowire quantum dots. (**a**) Dark field optical microscope image of standing nanowires, observed as bright white spots (scale bar is 5 μm). Inset shows a scanning electron micrograph of a 4 μm long, standing nanowire. (**b**) Schematic nanowire device. Magnetic field and optical axis are parallel to the nanowire axis. (**c**) Photoluminescence (PL) spectra for increasing excitation power, taken at 4.2 K under non-resonant (532 nm) cw excitation. The two emission peaks correspond to the exciton (X) and biexciton (2X) transitions. (**d**) Example of a narrow exciton transition from a single dot. The linewidth is limited by our setup resolution. (**e**) Integrated PL intensity of X and 2X versus excitation power. The solid (dashed) line is a guide to the eye for linear (quadratic) power dependence.

The presented data are all taken at 4.2 K on different quantum dots. Figure 5.1 shows optical spectra with peaks as narrow as 31 μeV (limited by the

resolution of our spectrometer). Figure 5.1d shows a single peak for exciton emission (X) at low excitation power. On increasing the power the biexciton (2X) emission becomes visible with an exciton-biexciton splitting of 2.2 meV. The PL intensities of X and 2X depend, as expected, linearly and quadratically on excitation power (Figure 5.1e), clearly identifying these optical transitions. Note also the saturation of the peak intensities at high powers indicating that also other states become occupied.

5.3   Magnetic field dependence

Next we measure the spin splitting of the exciton transition as function of a magnetic field, B, parallel to the nanowire axis (*i.e.* Faraday configuration). The excitation light is polarized linearly with an energy exceeding the InP bandgap. Via phonon relaxation, electrons and holes occupy the quantum states in the dot where they annihilate under emission of a photon (see Figure 5.2a and b). We select the exciton transition from the lowest energy (s-) states and measure the peak evolution as a function of B. Figure 5.2c shows a peak splitting linear in B on top of a quadratic B-dependence. The distance between the two peak maxima corresponds to the Zeeman spin splitting from which we obtain an exciton g-factor, $g_{exc} = (g_e + g_h) = 1.3 \pm 0.1$. A g_{exc}-factor value between 1 and 2 is typical for our dots with a material fraction As/P = 1/3. Variations between dots are likely due to small variations in the material composition and different confinements [58]. The overall quadratic shift, $\alpha = 10~\mu\text{eV/T}^2$, can be fitted to the diamagnetic shift of an electronic orbital with a diameter of ~ 20 nm [33]. This is in reasonable agreement with our quantum dot size.

   The measured PL in Figure 5.2c is not filtered for a specific polarization. By adding such filters (see setup in Figure 5.2b) we analyze the polarization of the emitted photons from which we deduce the spin states of the exciton transitions. Right (σ^+) and left (σ^-) circularly polarized photons are expected, respectively, for the exciton states $\downarrow\Uparrow$ and $\uparrow\Downarrow$. Here, $\uparrow(\Uparrow)$ represents a spin-up electron (hole) and $\downarrow(\Downarrow)$ represents a spin-down electron (hole). For well-resolved spin states at 9 T we indeed find in Figure 5.2e that the high energy emission peak consists of σ^+-photons whereas the lower energy peak is σ^--polarized. Note that the (nearly complete) absence of a second peak in Figure 5.2e implies full circular polarization of the two spin resolved exciton transitions. For linear polarizers, two peaks of equal height are visible, as expected (Figure 5.2d). For spin-degenerate excitons at $B = 0$ the polarization analyzers make no difference for the observed PL, as shown in Figures 5.2f and g. We emphasize that the observed absence of any
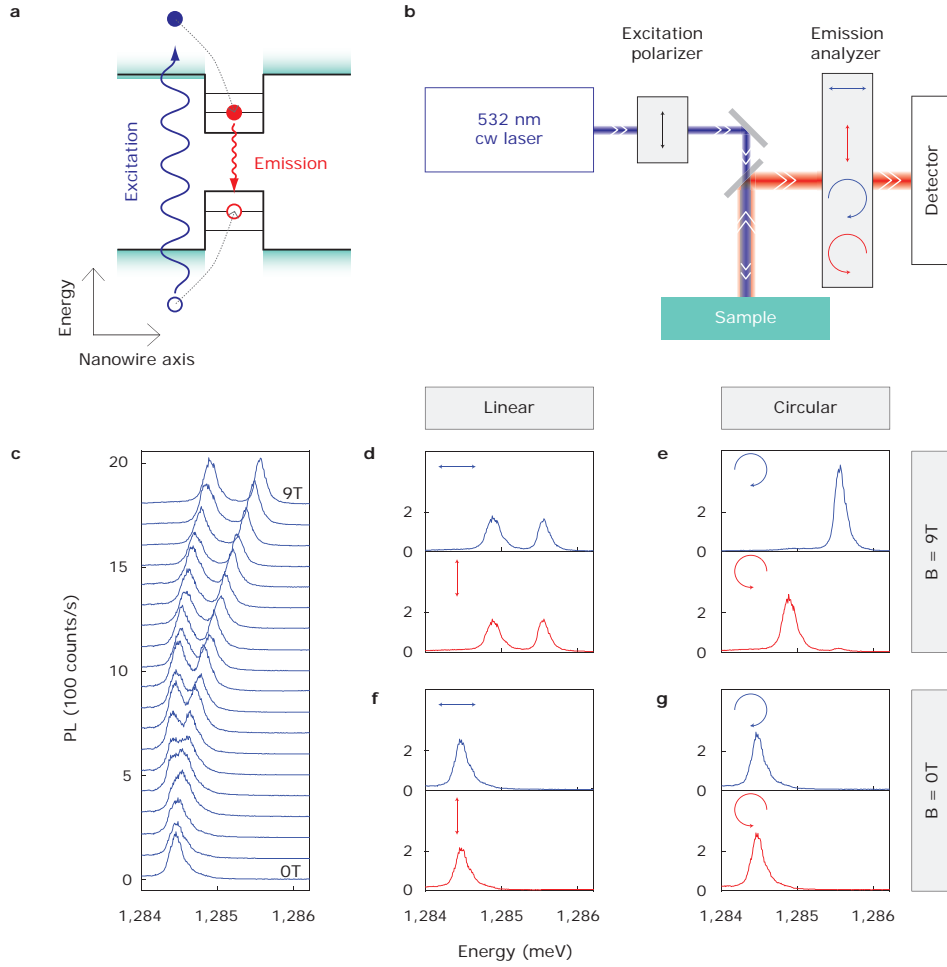
Figure 5.2: Polarization sensitive magneto-photoluminescence of a single nanowire quantum dot. (**a**) Schematic of non-resonant excitation and recombination. (**b**) Experimental setup. The excitation polarization is vertically linearly polarized, while the polarization of the emission is analyzed. (**c**) PL for different magnetic fields in steps of 0.5 T. Emission polarization is not filtered. (**d-g**), PL with linear and circular polarization filters for 0 and 9 T.

linear polarization for vertical nanowires is essential for exciting and measuring specific spin states, which we discuss next.

5.4 Polarization-selective excitation of spin states

A specific spin state can be excited when using either σ^+ or σ^- polarized light. If the emitted photons have the same polarization, it means that no spin relaxation has occurred during this excitation-relaxation cycle. Although this cycle is short

(of order the radiative lifetime of about 1 ns) it represents a first step towards an exciton-spin memory. A complete spin memory also requires the ability to suppress the radiative decay for a controllable storage time, as has been demonstrated with self-assembled dots [72]. We have found that excitation above the InP band gap (as in Figures 5.1 and 5.2) with subsequent relaxation into the dot, scrambles up the spin state and thus destroys any spin memory effect. The phase space for relaxation is largely reduced when we excite below the InP band gap into one of the confined higher energy states of the dot. Figure 5.4a illustrates excitation in an excited p-state with subsequent relaxation to the ground s-state. This relaxation between confined states is spin conserving, as we now demonstrate.
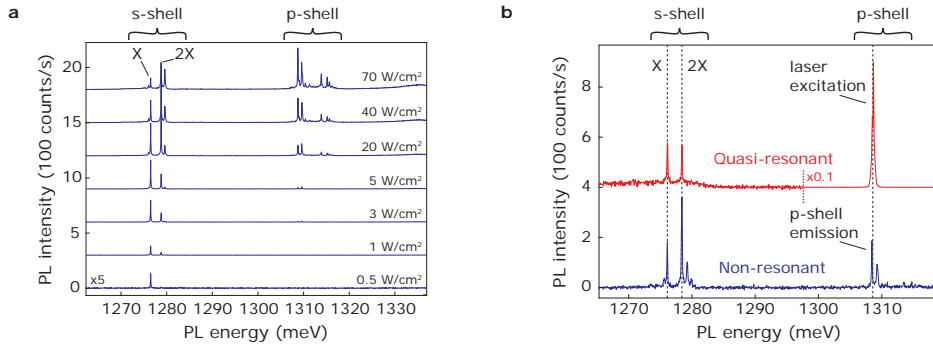
Figure 5.3: Excited states in a nanowire quantum dot. (**a**), Power dependent PL from a nanowire quantum dot. At low powers only the X and 2X transitions are visible. At high excitation powers the X and 2X peak heights saturate and excited states at higher emission energies become visible. (**b**), Comparison of non-resonant PL (lower blue spectrum) with quasi-resonant PL (upper red spectrum). In the lower spectrum the exciton, biexciton, and excited states are visible. The upper spectrum is taken with the laser energy tuned into the p-shell at 1309 meV. The peak at 1309 meV is from excitation light scattered into the detector. The peaks at lower energies correspond to the X and 2X transitions after fast phonon relaxation from the p-shell to the s-shell.

We characterize the higher energy states using combined PL and PLE (photoluminescence excitation) and identify a p-shell resonance around 1300 meV. Figure 5.3a shows an example of non-resonant photoluminescence spectra of a nanowire quantum dot under increasing excitation power density. Under low excitation power density, only the exciton (X) transition is visible. At higher powers also the biexciton (2X) appears (as identified by its quadratic power dependence). When increasing the power further, new emission lines in a second energy band emerge. These emission lines emerge from excited states in the quan-
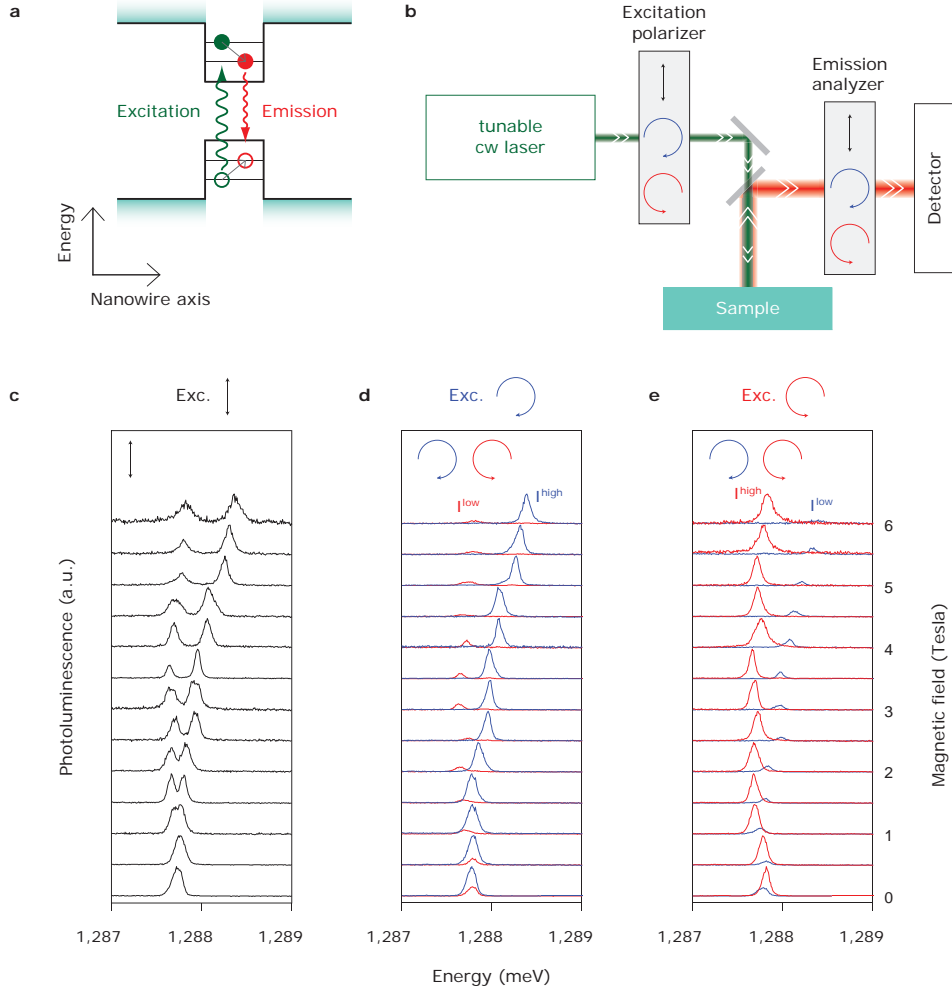
Figure 5.4: Polarization selective excitation and detection of exciton spin states. (**a**) Schematic of quasi-resonant excitation and recombination. (**b**) Experimental setup. Both excitation and detection polarizations are varied. (**c-e**) PL for different magnetic fields. Excitation is linearly, right circularly and left circularly polarized, respectively. Emission analyzers are set to linear (black), right (blue) or left (red) circular polarization.

tum dot, which are populated when the ground states are saturated. Figure 5.3b shows a comparison of non-resonant PL with quasi-resonant PL. Resonances in absorption are found in the same energy region as the p-shell emission.

We use quasi-resonant excitation into this p-shell and measure the exciton luminescence for various polarization analyzers (see schemes in Figure 5.4a,b). We first reproduce Figure 5.2c but now for quasi-resonant excitation. Figure 5.4c is taken with linear excitation and analyzer such that both spin states are excited and measured. Again as a function of B, the exciton transition shows a Zeeman

splitting and a diamagnetic shift. Note that the two split-peaks are of different height due to a slightly unequal spin excitation since the p-shell also shows spin splitting. Figures 5.4d and e show the results for left and right circularly polarized excitation. When exciting with right circular polarization, only the spin up branch of the Zeeman split exciton is populated. In this case we dominantly observe luminescence from the high-energy peak which is also right-circularly polarized. We thus clearly observe spin memory. Close inspection reveals that the spin memory is not perfect and that also a small peak for the wrong polarization is observed. For non-zero B the peak-height ratio $I^{high}/I^{low} \sim 10$. However, at $B = 0$ a reduced polarization ratio $I^{high}/I^{low} \sim 3$ was found for all seven dots that we measured. This likely indicates spin relaxation mediated by the hyperfine interaction with nuclear spins [73]. Similar measurements have been reported on ensembles of self-assembled quantum dots under quasi-resonant [74] and resonant excitation [75]. However polarization memory was not observed at $B = 0$, possibly due to a larger exciton fine structure splitting.

5.5 Energy-selective excitation of spin states

As we noted the spin memory only works for quasi-resonant excitation into the p-shell. The precise initialization of a particular spin depends on the exact excitation conditions, as exemplified by the peak height differences in Figure 5.4c. This excitation energy dependence can, as we discuss now, be exploited for an alternative method for spin initialization. To understand the absorption sensitivity, Figure 5.5a shows quasi-resonant PLE into the p-shell for linearly polarized excitation. The excitation energy is scanned and the spin-split exciton transition is measured at 4 T. The lower left panel shows two vertical stripes that are narrow in PL energy (~ 0.1 meV) but broader along the vertical axis of excitation energy (~ 3 meV). These widths are directly related to the respective lifetimes, short in the p-shell ($\sim$ ps due to fast intra-band, non-radiative relaxation to the s-shell) but much longer for the inter-band radiative decay. The stripes are colored red and blue indicating the degree of measured circular polarization. Note that the red stripe is slightly shifted up in energy, indicating a higher σ^-intensity at high excitation energies. The upper panels display two cuts clearly showing a larger σ^--peak at high excitation energy and a larger σ^+-peak at low excitation energy. We find maximum polarization ratios $I^{high}/I^{low} \sim 2.5$. We emphasize that this polarization occurs despite using linear excitation light. The polarization is entirely due to selectivity in the *energy* of the excitation. By combining *energy*-selective excitation together with *polarization*-selective excitation, as shown in

Figures 5.5b,c, the polarization ratio is further increased to $I^{high}/I^{low} \sim 10$.
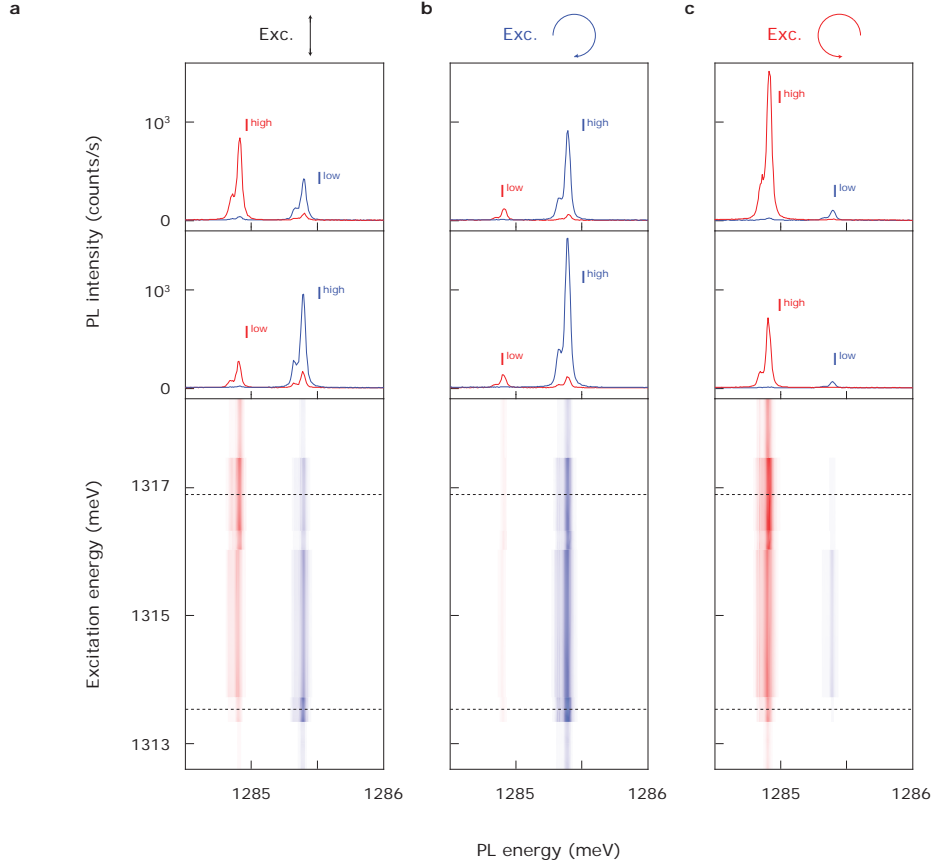
Figure 5.5: Selective excitation and detection of exciton spin states at 4 T.
Bottom panels show photoluminescence excitation (PLE) scans under (**a**), linearly,
(**b**), right circularly, and (**c**), left circularly polarized excitation. Blue and red colors
are measured separately with right and left circular polarization analyzers. Upper and
middle panels show horizontal cross sections taken, respectively, at the upper and lower
dashed lines in the lower panels.

5.6 Conclusion

In conclusion we have demonstrated clean quantum dots in nanowires with narrow
optical transitions. Specific exciton spin states are created and measured with
properly polarized light. In addition, we have demonstrated an alternative energy
selective mechanism for spin excitation. Future devices will have top and bottom

electrical contacts, for instance, for the use of fast energy selectivity using the Stark effect.

5.7 Methods

The nanowires were synthesized in a low pressure (50 mbar) Aixtron 200 metal-organic vapour-phase epitaxy (MOVPE) reactor in the vapour-liquid-solid growth mode. Colloidal gold particles of 20 nm diameter were deposited on a (111)B InP substrate as catalysts for nanowire growth. The diameter of the nanowire and the quantum dot was set by the gold particle size, while the nanowire density was set by the gold particle density on the substrate. The dot height and nanowire length were controlled with growth time [56]. By controlling diameter, height, and As concentration we can tune the quantum dot emission over the wide range of 900 nm to 1.5 μm [76]. Under appropriate growth conditions we were able to grow a sample with low density of nanowires containing single $InAs_{0.25}P_{0.75}$ quantum dots. These dots are designed to have luminescence around 1.2 eV. The gold particle is transparent for the light.

Micro-PL studies were performed at 4.2 K. For non-resonant excitation experiments, the nanowire quantum dots were excited with a linearly polarized 532 nm continuous wave laser focused to a spot size of 0.6 μm using a microscope objective with a numerical aperture $NA = 0.85$. For photoluminescence excitation experiments a tunable titanium sapphire laser was used. The PL signal was collected by the same objective and was sent to a spectrometer, which dispersed the PL onto a nitrogen-cooled silicon array detector with 30 μeV resolution. Linear and circular emission polarizations were analyzed using a half- or quarter-waveplate, respectively, followed by a fixed polarizer. Linear and circular excitation polarization was set by placing a fixed polarizer followed by a half- or quarter-waveplate, respectively. Magnetic fields were applied in the Faraday configuration, *i.e.*, along the quantum dot confinement axis. The data shown are all measured on different quantum dots. Similar results on polarization sensitive magneto-photoluminescence have been found on 3 dots. Polarization memory at $B = 0$ T has been measured on 7 dots, giving all similar results.

Chapter 6

Electron and hole g-factors in nanowire quantum dots

B. J. Witek, R. W. Heeres, U. Perinetti, R. E. Algra,
E. P. A. M. Bakkers, L. P. Kouwenhoven & V. Zwiller

We performed a magneto-luminescence experiment in order to determine the g-factors of electron and holes confined in a nanowire quantum dot. Our setup allows to apply magnetic fields along different directions in a plane parallel to the wire, making it possible to explore the Faraday geometry, the Voigt geometry as well as intermediate cases. This allowed us to determine 2 parameters of the g-tensors for both electron and hole.

6.1   Introduction

The coupling of a magnetic field to the spin of a particle is determined by its g-factor. In a semiconductor the spin-orbit interaction couples the angular momentum of carriers with their spin so that different energy bands correspond to states with a well defined total angular momentum. For this reason the observed g-factors in a semiconductor are different from the g-factor g_e of a free electron. Confinement introduces mixing between different bands and further modifies the g-factors of electrons and holes. Moreover, the g-factors of electrons and holes in a semiconductor structures usually depend on the direction of the applied field and can be described by a tensor of g-factors.

In the case of quantum dots it is often not easy [77] to calculate the g-factors: uncertainties in the shape and strain of a quantum dot can make it difficult to compare theoretical predictions and experimental data. Nanowires offer, in principle, the possibility of controllably growing dots of different sizes and aspect ratio allowing to make a systematic comparison between experiment and theory. Moreover strain is less important in nanowires, compared to self-assembled dots. In an experiment from a few years ago [78] it was possible to determine the electron g-factors for a series of quantum dots of different length in transport experiments. These values are in good agreement with a theoretical model [79]

In this chapter we present our preliminary results of a similar experiment, in which we used optical means in order to determine both the electron and hole g-factors for a InAsP quantum dot in a InP nanowire. The wires we studied come from the same batch as the ones described in chapter 5 and should have similar size and composition. While for the experiment presented in chapter 5 we could only apply a magnetic field along the nanowire axis, a new cryostat with a vector magnet allowed us to vary the direction of the magnetic field in a plane x-z, with z being both the optical axis and the nanowire direction. The g-factors can be derived by fitting the Zeeman splittings of an exciton transition with the ones predicted by the Hamiltonian $H_{exchange} + H_{Zeeman}$ introduced in chapter 2. In particular it is possible to determine $g_{e,x}$, $g_{e,z}$, $g_{h,x}$ and $g_{h,z}$ by measuring the Zeeman splittings produced by magnetic fields along three different directions.

6.2   Measurements

So far we could only take this set of measurements for one quantum dot. The main technical issues in performing this experiment were the difficulty of finding quantum dots with narrow optical transitions and the fact that the optical alignment was seriously modified as we swept the magnetic field. We tackled the

first issue by automating the search for quantum dots: we systematically scanned small regions of our sample (of a typical size of some tens to hundreds of μm) taking a spectrum at every step. During the scanning we recorded sharp photoluminescence peaks and the corresponding position. Afterwards we manually selected the quantum dot to study from the list of automatically found dots. The problem of loosing the optical alignment in magnetic field was partially solved by an automatic adjustment of the sample position and by a manual alignment of the collection optics.

We applied different magnetic fields to the quantum dot in different directions: parallel to the wire (Faraday configuration), orthogonal to the wire (Voigt configuration) and at an angle of 60° with the nanowire. In each case we increased the magnetic field in steps of 0.2 or 0.1 T, which was useful, and at times necessary, not to completely loose the alignment with the dot. We focus our attention on the splitting of a photoluminescence line that can be attributed to a singly charged exciton X$^+$ or X$^-$ based on the absence of fine structure splitting as evidenced by the measurements in magnetic field. In the case of Faraday configuration, the exciton line splits into two bright transitions with orthogonal circular polarizations: left and right. The energies of this two peaks are plotted in Figure 6.1 as a function of magnetic field. The diamagnetic shift, common to both transitions, was determined by fitting and subtracted from the plotted data. This measurement allows to determine the sum of electron and hole g-factors along the wire direction z.

In Voigt configuration the states involved in the optical transitions are mixed and four transitions become allowed and visible in photoluminescence. In this case the energy separation between different transitions is smaller than in Farday configuration and can be comparable to their linewidth. Neighboring lines have, however, orthogonal linear polarizations, making it possible to accurately determine their energy even at relatively small fields. From this data (Figure 6.2) we can determine both $g_{e,x}$ and $g_{h,x}$ [30].

In order to determine $g_{e,z} - g_{h,z}$ we need to be able to observe the dark transitions, which requires $B_x \neq 0$, and to also have a non zero B field component in the z direction. We chose, somewhat arbitrarily, to apply a field at 60° with the nanowire. In this case (Figure 6.3) the relation between Zeeman splittings and g-factors is less immediate and we determined the g-factors by fitting the data with a numerical model. This allows not only to calculate $g_{e,z} - g_{h,z}$, but also as a confirmation of the model, because the four g-factors we estimated are overdetermined by measuring five energy differences. Another confirmations that the model we are using is appropriate to describe the data come from the correspondence between calculated polarizations and measurement intensities with

the measured ones.

The g-factors that best fit the three sets of data are presented in Table 6.1. The uncertainties linked to the fitting are of about 10%. A possible additional source of error is the uncertainty in the angle between the magnetic field and the rotational symmetry axis of the quantum dot.

6.3 Conclusions

In conclusion, we could determine the electron and hole g-factors for electron and holes in a InAsP nanowire quantum dot, by studying the splitting of a singly charged exciton line in magnetic fields along three different directions. Although the attribution of the studied line to a charged exciton transition is very plausible, more measurements are necessary to confirm it.
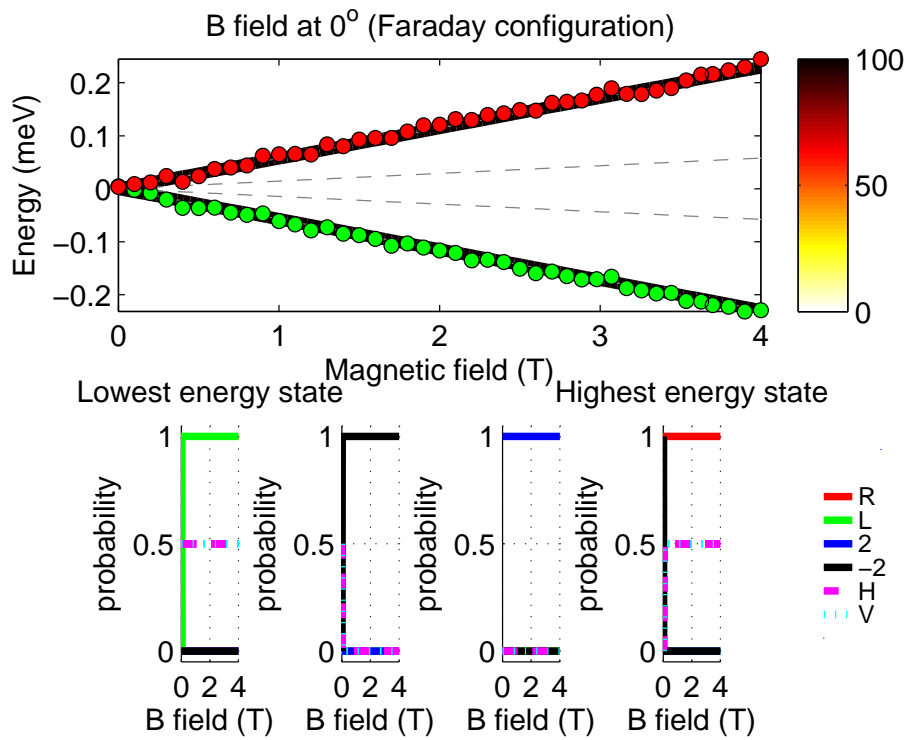
Figure 6.1: Faraday geometry. Magnetic fields of different intensities are applied parallel to the nanowire direction and there is a clear distinction between bright and dark transitions. The colormap shows the expected relative intensities for different transitions (dashed lines). Measured peak positions are shown as red and green points. The lower panels shows, for each transition, the probabilities of an emitted photon being measured in different polarization states.
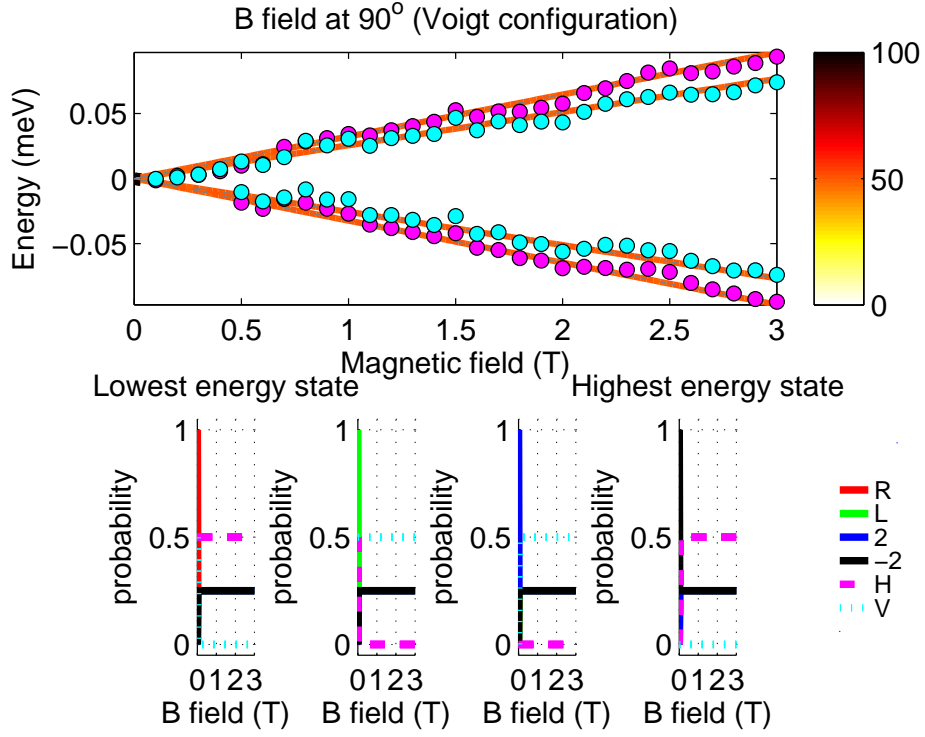
Figure 6.2: Voigt geometry. Magnetic fields of different intensities are applied parallel to the nanowire direction causing mixing between bright and dark transitions.

Table 6.1: g-factors

	x	z
electron	1.00	0.74
hole	0.12	1.24
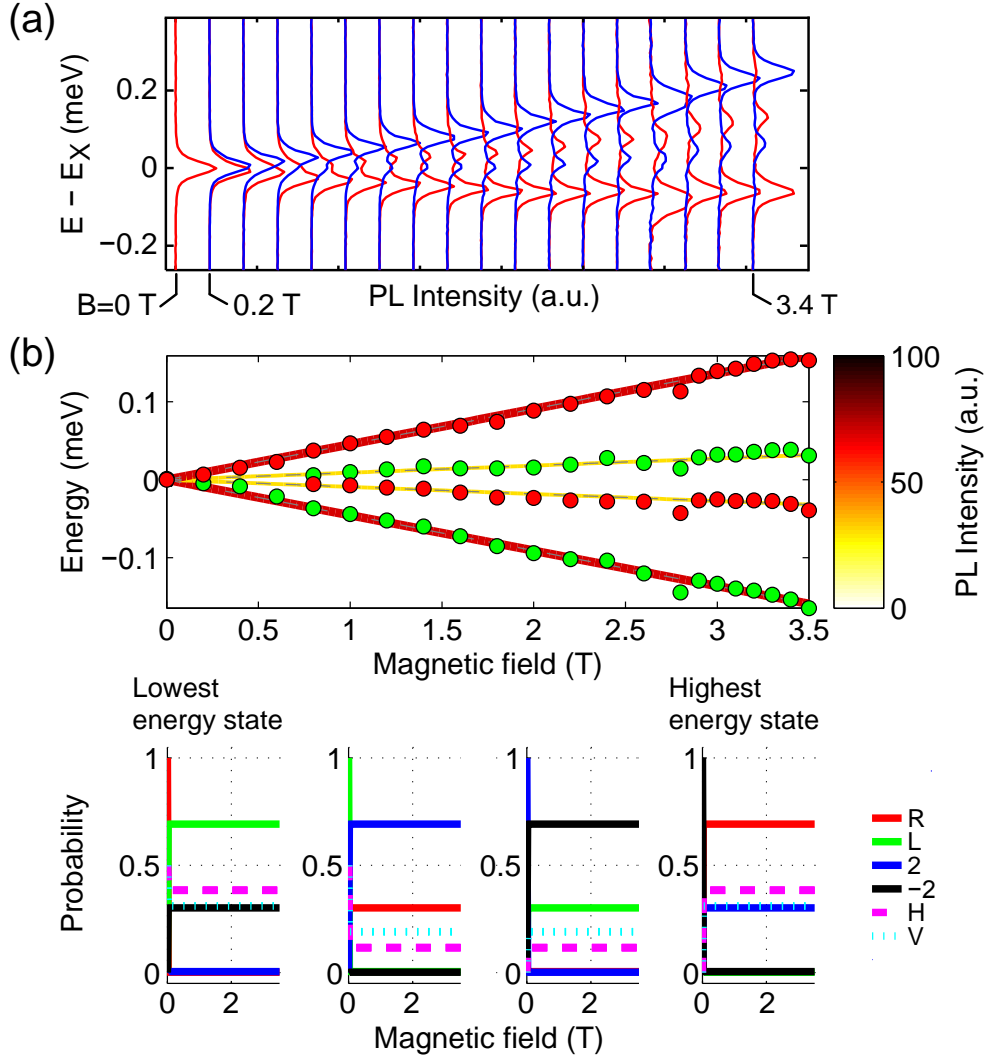
Figure 6.3: Field at $60°$ **with the wire.** The magnetic field component orthogonal to the wire mixes electron and hole states with a given angular momentum along z. This makes the dark transitions visible. (**a**) Measured spectra. Data plotted in blue (red) correspond to right (left) circularly polarized light. (**b**) Measured peak positions are plotted as colored points with the color reflecting the predominant polarization state. A fit to this measurement together with the other ones allows to determine the difference of hole and electron g-factors in the z-direction.

Chapter 7

Tuning the optical transitions of single GaAs quantum dots in resonance with D$_2$ transitions of a rubidium vapor

N. Akopian, U. Perinetti, L. Wang,
O. G. Schmidt, A. Rastelli, & V. Zwiller

We study single GaAs quantum dots with optical transitions that can be brought into resonance with the widely used D$_2$ transitions of rubidium atoms. We achieve resonance by Zeeman shifting the quantum dot levels and by Stark shift. This allows for the controlled coupling of an atomic vapor to a nano-scale, sub-poissonian light source. We discuss an energy stabilization scheme based on the absorption of quantum dot photoluminescence in a rubidium vapor. This offers a scalable means to counteract slow spectral diffusion in quantum dots, on time scales longer than 0.1 s.

7.1 Introduction

Quantum dots (QDs) can be used as efficient sources of single photons [80] with applications in the fields of quantum information and quantum communication [81]. Producing single photons that are indistinguishable, however, has proven quite challenging and the emission of identical photons from independent QDs has been demonstrated only very recently [82]. One of the difficulties in interfering photons from independent dots is that the spectra of different dots are not only different but they also fluctuate in time, making it difficult to adjust the energy of two or more QDs in perfect resonance. Some of the processes that cause spectral diffusion have rather slow time constants. This is the case for the energy shifts due to the hyperfine interaction with randomly oriented nuclear spins. In GaAs QDs the effective magnetic field due to the nuclei is a few mT, depending on the size of the dot, and evolves on a time scale that can be up to seconds [83].

The ability to produce indistinguishable photons from independent sources [84, 85] is a powerful tool for quantum information processing because interfering photons is a crucial ingredient for linear optics quantum computation [15], for the entanglement of remote qubits [8] and for quantum cryptography based on time-bin entanglement [86]. A scalable means to tune different QDs into resonance is therefore highly desirable.

Here we show that GaAs QDs can be brought to resonance with the D_2 transition line of ^{87}Rb (780 nm) by applying an external electric or magnetic field. Rb vapor cells are extensively used as a simple wavelength standard for lasers, are available in sub mm sizes [87] and would be suitable to stabilize in energy two independent QDs. The detuning of a photoluminescence (PL) line from the D_2 transitions is determined by measuring the PL transmission through a Rb vapor cell. This direct energy comparison between the optical transitions of a QD and Rb atoms would provide a fast and precise measurement of the QD environment. We examine how the transmitted PL can be used as a feedback signal for stabilizing the QD emission energies, we discuss the noise level and the achievable feedback rate.

7.2 Quantum dot fabrication and characterization

The QDs we study are GaAs inclusions in an AlGaAs matrix and are fabricated by molecular beam epitaxy in a multi-step self-assembly process [88, 89]. First we create a template of Stranski-Krastanow InAs/GaAs QDs. The sample sur-

face is then capped by GaAs and the InAs dots are removed by in-situ etching, leaving holes on a GaAs surface. After growing a 10 nm thick AlGaAs layer, the sample surface still shows nano-holes which are filled with GaAs to form the QDs discussed here. Finally an AlGaAs layer is grown. A scheme of the resulting sample structure is shown in the inset of Fig. 7.1. The QDs are connected by a GaAs quantum well (QW) whose thickness was optimized so that the QD photoluminescence is close to 780 nm. Unstrained GaAs/AlGaAs QDs are expected to have good properties for what concerns electron spin dephasing time because of the small nuclear spin of gallium ($I = 3/2$) as compared to indium ($I = 9/2$).

We studied the optical properties of these structures in a micro-photoluminescence setup at 4.2 K. In order to identify some of the transitions and study their fine structure we performed different polarization measurements and reconstructed the states by quantum tomography. Figure 7.1(a) shows photoluminescence spectra of a single QD for two orthogonal polarization states. The high energy peak is visible at low excitation power and consists of two linearly polarized components [Fig. 7.1(b)] with a fine structure splitting of 60 μeV. Based on these data, on previous studies of similar QDs and on information about the background doping [88], we can identify it as the neutral exciton transition and we can also identify the positively charged exciton [marked in Fig. 7.1(a) as X^+]. The case of indistinguishable photons emitted by two singly charged QDs is of particular interest: the spins of the electrons or holes that are left in the QDs after exciton recombination can be entangled by interfering the emitted photons on a beam splitter as recently demonstrated with atomic systems [8].

We performed time resolved PL measurements to determine the decay times of the optical transitions in our dots. We excited the dots with a pulsed Ti:Sapph laser with an energy of 1.676 eV and measured the time dependent PL with a streak camera. The typical decay time of about 500 ps [Fig. 7.1(c)] corresponds to a natural linewidth of 1.3 μeV and sets the relevant energy scale within which two dots need to be tuned in order to achieve a large degree of photon indistinguishability.

7.3 Energy tuning

7.3.1 Tuning by magnetic field

Without additional processing, we can tune the QD emission in resonance with the D_2 transition of Rb by applying an external magnetic field. We used magnetic fields up to 9 T along the growth direction allowing for energy shifts as large as 2 meV. We fitted the changes in peak positions including the Zeeman
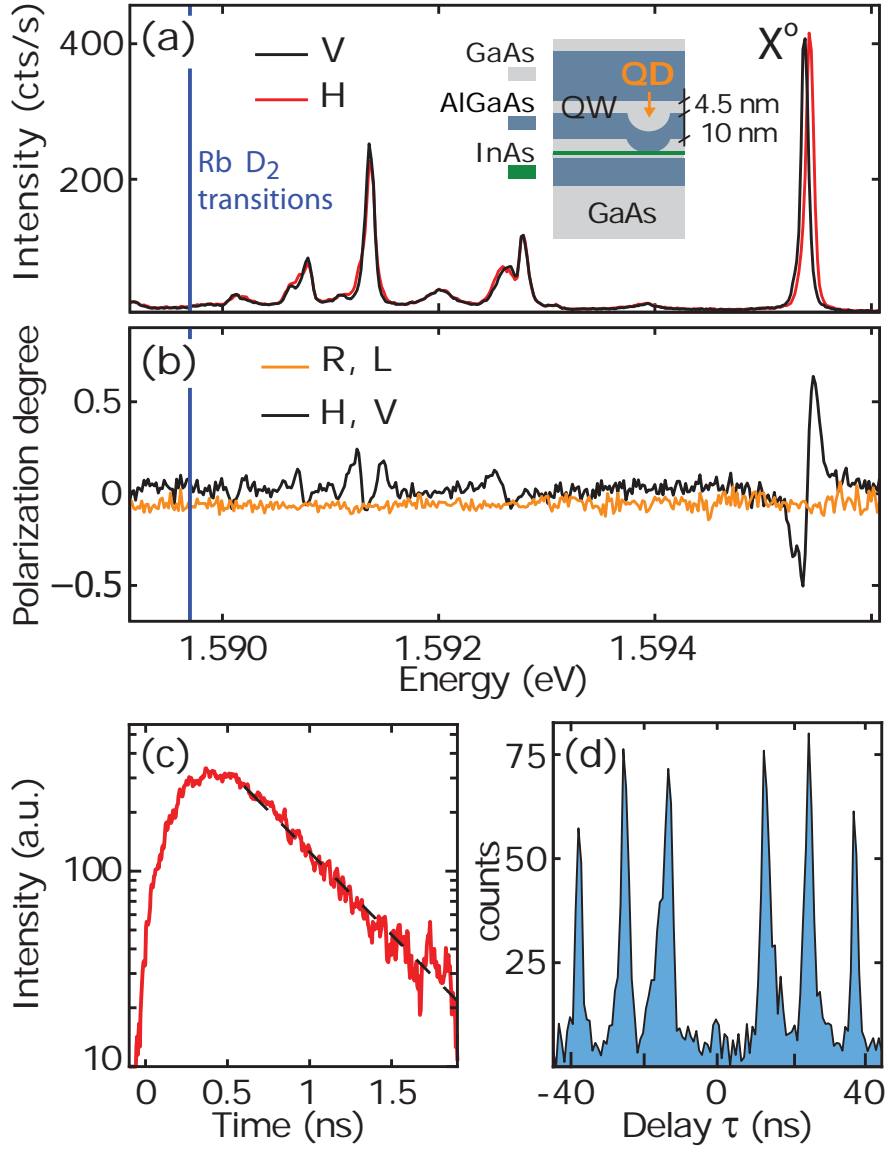
Figure 7.1: (a) Photoluminescence intensity for two orthogonal linear polarizations, horizontal (H) and vertical (V). The two components of the high energy peak are separated in energy by 60 μeV and correspond to the decay of the neutral exciton. The bright line at lower energy is unpolarized and can be attributed to the positively charged exciton. (b) Degree of polarization, $\left(I_{R(H)} - I_{L(V)}\right) / \left(I_{R(H)} + I_{L(V)}\right)$, for right and left (R, L) circularly polarized light and for horizontally and vertically polarized light. I_j is the PL intensity for polarization j. (c) Time resolved PL intensity from a single transition. For this measurement a QD is excited non resonantly by a picosecond pulse laser (1.676 eV, 76 MHz repetition rate). An exponential fit (dashed line) reveals a typical decay time of about 500 ps. (d) Autocorrelation measurement under pulsed excitation.

shift, the diamagnetic shift and the fine structure splitting of the exciton line and we determined an excitonic g-factor of 2.0 and a diamagnetic coefficient of 4.9 μeV/T^2.
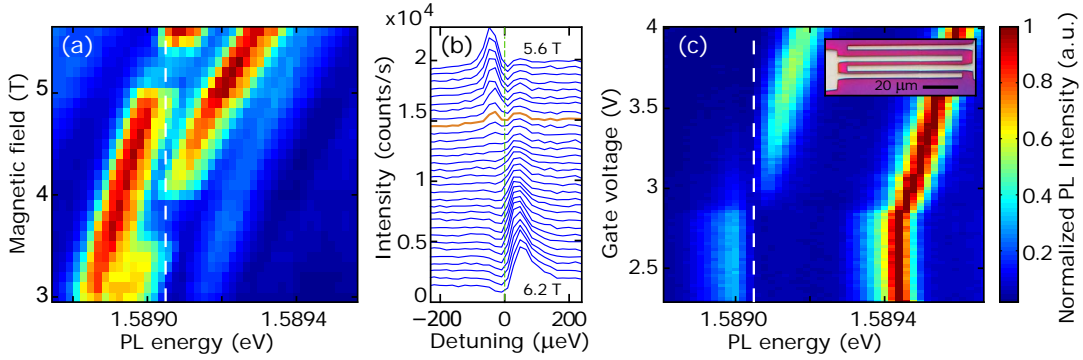
Figure 7.2: (a) Zeeman split PL line from a single QD as a function of magnetic field. The photoluminescence is filtered by a Rb cell before entering the spectrometer. Pronounced absorption at the D$_2$ transitions visible around 1.58905 eV (vertical line). (b) A PL line of another QD is brought into resonance with the D$_2$ transitions of Rb. (c) Stark shift is used to tune a third QD in resonance with Rb transitions. Pholuminescence spectra are shown as a function of gate bias. The inset shows metallic gates on the sample surface, 130 nm above the QD layer allowing to apply an in-plane electric field.

Figure 7.2(a) and 7.2(b) show the tuning of a different QD transitions in and out of resonance with the D$_2$ Rb transitions by means of an external magnetic field applied along the growth direction. The PL from the dot is collected by a microscope objective (NA = 0.85) and sent, in a collimated beam, through a 10 cm long cell filled with Rb vapor. The vapor is in equilibrium with liquid Rb at a temperature of 134 °C and 120 °C for Fig. 7.2(a) and 7.2(b) respectively. The PL transmitted through the cell is measured by a spectrometer. The lowest spectrum in Fig. 7.2(b) corresponds to a magnetic field of 6.2 T. Absorption by the Rb D$_2$ transitions is visible at zero detuning. As the magnetic field is lowered a PL line comes closer to resonance with the D$_2$ transitions, is absorbed in the Rb vapor and scattered away from the optical path. At B= 5.76 T the PL line is on resonance and almost completely absorbed (orange spectrum in Fig. 7.2(b)). With this tuning technique, two independent QDs can be made resonant with each other by tuning them both to the same reference wavelength.

7.3.2 Local tuning by electric field

In order to have more control on the optical transitions of a quantum dot we used an electric field as an extra tuning parameter and Stark shifted a QD transition in resonance with the Rb D_2 transitions. This would be useful for the implementation of more complex experiments like the remote entanglement of two spins [8]. In this case it is necessary to interfere photons of two different circular polarizations (right and left) which are emitted at two different energies due to the Zeeman splitting. For this reason two tuning parameters are needed.

We create an E field in the dot region by means of metallic gates on the surface of the sample. The gates are 3 μm wide and spaced by 2, 3 and 4 μm (Fig. 7.3, inset). With this geometry the QDs, situated only 130 nm below the sample surface, are subject to a mostly in-plane electric field. This tuning technique based on local gates is in general preferable to the magnetic field tuning because it allows for addressing different dots independently and for faster control. Stark shifted transitions are shown in Fig. 7.2(c). One of the two PL lines is tuned in resonance with Rb D_2 transitions for a gate voltage of about 3V. For this measurement the Rb vapor temperature was set to 160 °C and the QD was populated via excitation in the QW by a 1.645 eV laser. The gates do not affect the PL transition at low bias because of screening caused by p-background doping.

7.4 Feedback scheme

In order to use a feedback system to lock an emitter at a given energy, the feedback signal should change sharply as the emitter is detuned from resonance by its natural linewidth. This is the case for the PL intensity transmitted through a Rb cell, because the Doppler broadening of 2.5 μeV, at room temperature, is comparable to the exciton natural linewidth.

The characteristic time for energy stabilization based on absorption in a Rb vapor depends essentially on the time Δt, required to measure the PL energy with the desired precision. We calculated the feedback signal [Fig. 7.3(a)] and the corresponding error in PL energy, ΔE, as follows. Neglecting Doppler broadening and considering only the D_2 transitions, the coupling of light to the Rb vapor is determined by the optical susceptibility $\chi = A \left(\sum_j \frac{g_j}{\omega - \omega_j + i\gamma_j} \right)$, where A is the total resonance strength, proportional to the density of Rb atoms, and the $g_j's$ account for the different strengths of each transition (between hyperfine split energy levels) at frequencies $\omega_j/2\pi$ with linewidths of $2\gamma_j$. We assumed the QD luminescence to be a Lorentzian with a width of 1.3 μeV and we took into account the Doppler broadening by convoluting the susceptibility χ with a 2.5 μeV wide
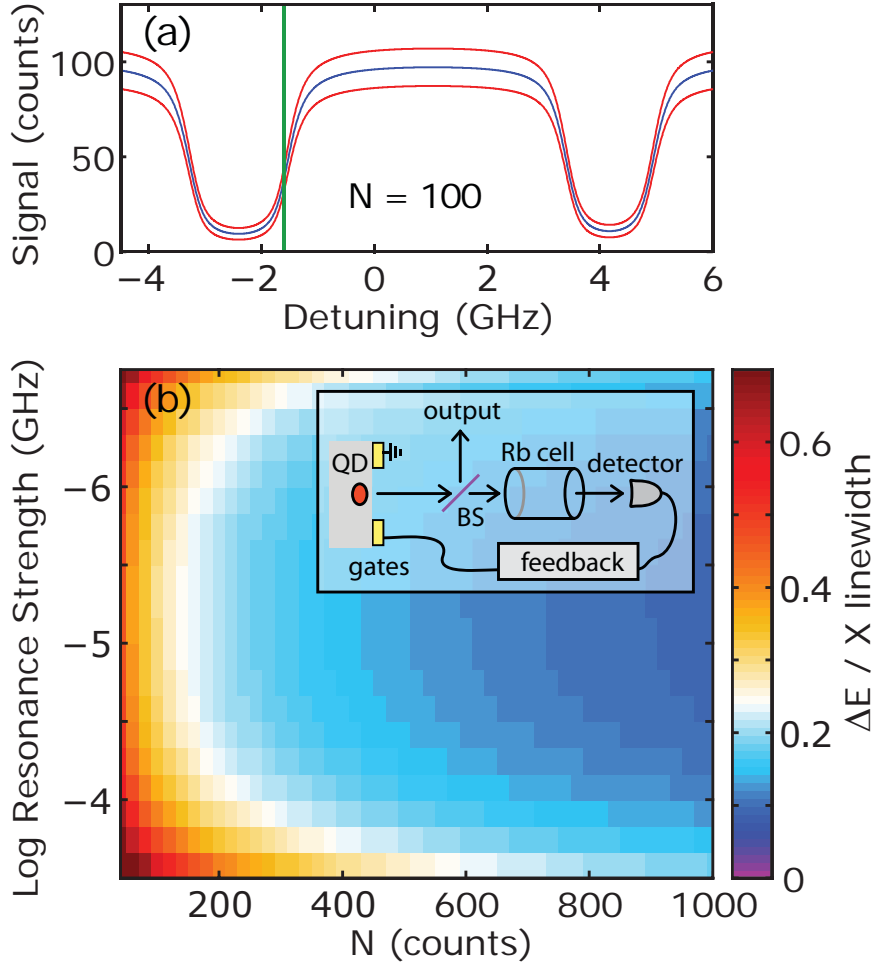
Figure 7.3: Estimation of the characteristic time for an energy stabilization system based on absorption by a Rb vapor. a) Transmitted photoluminescence intensity (counts) for a QD transition with a Lorentzian lineshape set by the decay time. The two red curves represent the Poissonian error range (plus and minus one standard deviation). b) Uncertainty in the measurement of the detuning of the QD transition, as a function of the coupling to the Rb vapor and of the PL intensity measured in counts. The inset is a sketch of the proposed feedback scheme.

Gaussian.

In the case of continuous wave excitation the noise of the transmitted PL intensity is Poissonian and determines the uncertainty on the PL energy that we wish to control. This uncertainty depends on the PL energy (the working point of the feedback) and is proportional to $1/\sqrt{N}$, with N the number of counts that would be measured for zero absorption in a time interval Δt. In calculating ΔE we approximated the feedback signal linearly around each working point. The

best working point is marked by a vertical line in Fig. 7.3(a).

The relevant quantity in view of producing indistinguishable photons is the ratio between the energy uncertainty ΔE and the exciton natural linewidth. This ratio is plotted in color in Fig. 7.3(b) as a function of the resonance strength A, and of the number of counts N. From this plot we can see that if two transition need to be tuned at the same energy within 20% of their linewidth, about 220 counts are necessary. For a typical intensity I=N/Δt of 3000 counts/s (see Fig.7.1) the characteristic time, Δt, for the proposed feedback is less than 0.1 s. The same type of QDs presented here were embedded in an optical microcavity [90] and intensities of about 10^5 counts/s were measured. For those QDs, the characteristic feedback time would be about 2 ms.

For most applications a source of indistinguishable photons needs to be triggered [91, 92] and the collection efficiency high [93]. This conditions can be satisfied by the QDs described here, provided that the dots are excited resonantly and that the collection efficiency is improved. It should be noted that in that case a well defined number of photons can be generated, giving sub-poissonian noise for the transmitted PL intensity. The error shown in Fig. 7.3, should therefore be considered as an upper limit.

7.5   Conclusions

In conclusion, we have demonstrated that optical transitions of single GaAs quantum dots can be tuned to resonance with transitions in rubidium atoms, by means of an external electric or magnetic field. This fact can be exploited for the energy stabilization of independent quantum dots and we discussed here the characteristic time of this tuning technique. Further improvements on the case discussed here would be the tuning of GaAs dots in microcavities and the triggered emission of photons. Both improvements would make the Rb vapour an even better energy reference due to sub-Poissonian noise in the feedback signal.

Chapter 8

Sharp emission from single InAs quantum dots grown on vicinal GaAs surfaces

U. Perinetti, N. Akopian, Yu. B. Samsonenko,
A. D. Bouravleuv, G. E. Cirlin, & V. Zwiller

We report on optical studies of single InAs quantum dots grown on vicinal GaAs(001) surfaces. To ensure low quantum dot density and appropriate size, we deposit InAs layers 1.4 or 1.5 monolayers thick, thinner than the critical thickness for Stranski-Krastanov quantum dot formation. These dots show sharp and bright photoluminescence. Lifetime measurements reveal an exciton lifetime of 500 ps. Polarization measurements show an exciton fine structure splitting of 15 μeV and allow to identify the exciton and charged exciton transitions with linewidth as narrow as 23 μeV.

8.1 Introduction

Self-assembled quantum dots (QDs) proved an excellent system for the implementation of quantum bits [91, 94, 95] and as sources of single [9, 96] and entangled photons [10, 97, 98]. The most common technique for growing self-assembled QDs, the Stranski-Krastanov (SK) method, allows for the fabrication of QDs with good optical properties: nearly lifetime limited linewidth of the optical transitions in these dots makes them suitable for single spin measurement [99] and two photon interference [100]. The ability of controlling the position of self-assembled QDs would allow for more complex devices and different attempts [101, 102] have been made in this direction. In particular a growth technique similar to the SK method has been used to produce rows of QDs [103] on vicinal GaAs substrates. Although this technique gives some control on the lateral alignment of QDs, the study of the optical properties of such vicinal QDs has been limited to ensemble measurements so far [104, 105].

In this letter, we present a study of the optical properties of single InGaAs QDs, grown on a vicinal GaAs substrate by molecular beam epitaxy (MBE). The low quantum dot density required for addressing single dots has been achieved by selecting a substrate with suitable misorientation angle and by exploring the subcritical regime of InAs island formation [106]. The high resolution spectroscopic measurements presented in this letter, combined with polarization selective and time resolved measurements, give a first contribution in identifying optical transitions in single QDs of this kind.

8.2 Sample fabrication

In orderto grow samples with differentQDsizes and densities, four substrates weremountedin the MBE reactor, namely an exactly orientedGaAs(001) substrate and threeGaAs(001) vicinal substrates misoriented by3°, 5° and 7°towards the [100] direction. After oxide layer desorption, a GaAs buffer layer was grown at 600 °C to ensure the translation of multi-atomic steps according to the substrate vicinality. A 10 period GaAs/AlGaAs superlattice was then grown to block carrier diffusion to and from the substrate. After growing a 100 nm thick GaAs layer, the substrate temperature was lowered to 485 °C and 1.4 or 1.5 InAs monolayers (ML) were deposited at a rate of 0.05 ML/s. The growth was then interrupted for 20 s. During this time QDs formed in thesubcritical regime, as the InAs layer thickness was below the 1.7 ML critical thickness for SK dot formation. Under the thermodynamically-controlled growth conditions typical of this regime, the predicted quantum dot spatial density is much smaller than the density of com-

monly used SK dots [107]. Additionally, the use of vicinal surfaces can allow for lateral ordering of QDs [108, 109]. The structure was finalized by a GaAs 70 nm cap layer.

8.3 Micro-PL characterization

8.3.1 Time resolved PL

We performed photoluminecence (PL) spectroscopy measurements on these eight samples under continuous-wave and pulsed laser excitation. The sample grown on the 7° misoriented substrate with a 1.4 ML InAs layer showed the narrowest emission linewidth and a low QD density allowing to study single dots. In the following we discuss measurements on this sample only.
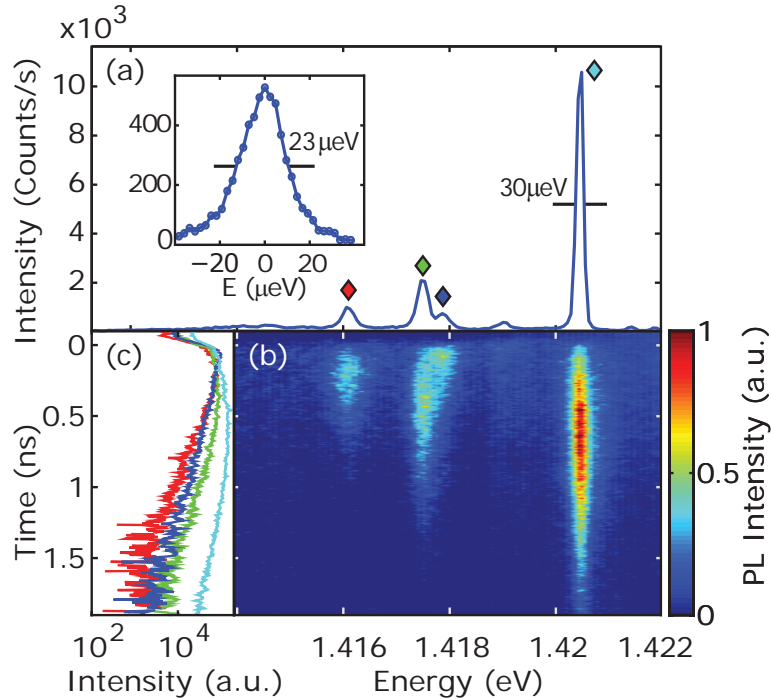
Figure 8.1: a) PL spectrum of a single vicinal quantum dot under pulsed laser excitation at 1.647 eV. The width of the brightest line is 30 μeV, limited by the spectrometer resolution. The inset shows a Fabry-Perot interferometer measurement on a narrow line from another QD. b) Time resolved PL measurement: a picosecond pulsed laser with a repetition rate of 76 MHz populates the quantum dot via non resonant excitation. c) Cuts of the graph in b) at the wavelengths indicated by the colored diamonds.

In order to measure on a single QD we looked for low density regions of the sample, based on PL spectroscopy. The resolution of our spectrometer is 30 μeV,

considerably smaller than the inhomogeneous distribution in the emission energy of different dots due to size fluctuations. We can therefore resolve a single dot by filtering the emission both spatially and in energy.

A typical spectrum from a QD grown on a 7° misoriented substrate is shown in Fig. 8.1, where different optical transitions can be resolved. The line at the highest energy is particularly bright compared to conventional SK dots (without a microcavity) [110] indicating that the effect of non-radiative processes is relatively small in these structures. Furthermore, the width of this line is smaller than the 30 μeV spectrometer resolution (see inset), suggesting these QDs could be used for sophisticated experiments where the selectivity in energy is a crucial requirement, such as spin entanglement in separated quantum systems [8].
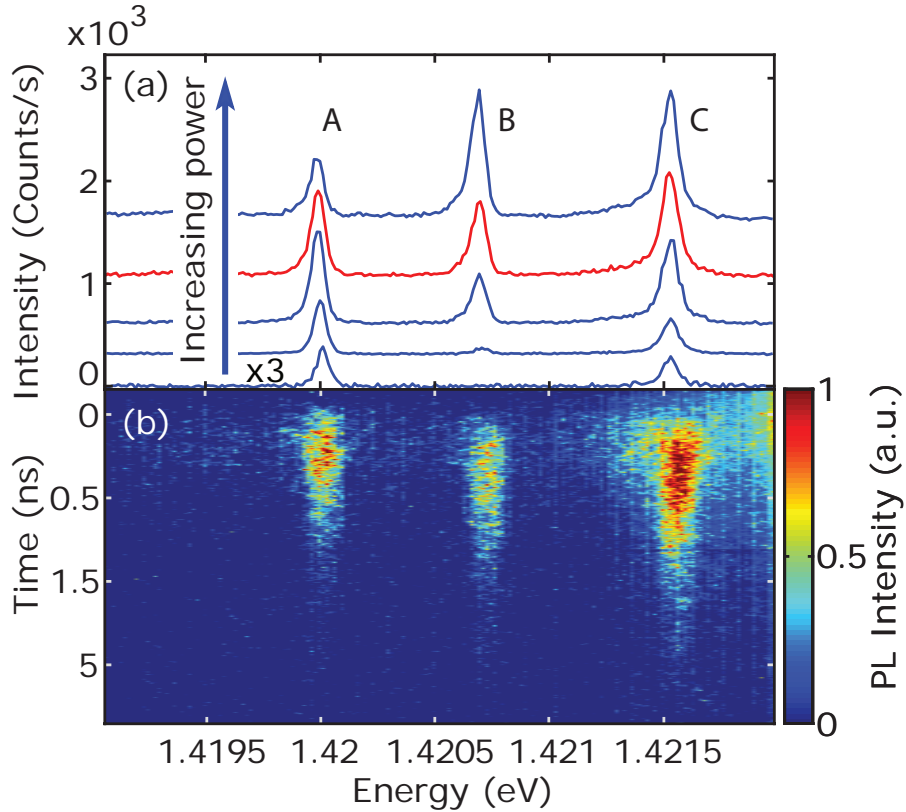
Figure 8.2: a) PL spectra of a quantum dot grown on a vicinal surface under pulsed laser excitation (1.647 eV) at various powers. b) Time resolved PL corresponding to the spectrum plotted in red.

The time evolution of the PL spectrum after pulsed-laser excitation (Fig. 8.1b,c) reveals a lifetime of the different states ranging from 300 to 600 ps. The maximum intensity of different transitions occurs at different times suggesting that the peaks could correspond to stages of a cascaded emission. Combining mea-

surements of this kind with polarization measurements allows us to identify some of the lines.

8.3.2 Line identification

In order to identify the exciton (X) and biexciton (XX) transitions in a QD we observe the dependence of the PL spectrum on excitation power. We expect the intensity ratio between the XX and X transition to increase with excitation power. Spectra taken at different powers (Fig. 8.2a) suggest that the middle line (B) could correspond to the XX transition. However, the time resolved measurement in Fig. 8.2b do not confirm this hypothesis as lines A and C are visible at earlier times than line B. A possible explanation of these data is that, as the excitation power is increased, the dot is found in different charged states leading to the observation of charged excitons alongside the neutral one.

A technique which allows to discriminate between neutral exciton and charged exciton transitions is polarization tomography [34]. By measuring the projection of the PL spectrum on six different polarization states we can reconstruct, for each energy, the polarization state of the emitted photons. The neutral exciton state is usually split in energy [111] so that the corresponding X transitions are of slightly different energy and orthogonal linear polarizations. The charged excitons, on the contrary, are not split, due to the Kramers degeneracy and give an unpolarized PL line. Due to this difference in polarization we can distinguish the exciton and charged exciton lines as in Fig. 8.3. Here the line on the low energy side shows a polarization structure suggesting that it corresponds to the X transition, while the other line is unpolarized and is attributed to a charged exciton.

8.4 Conclusions

To summarize, we report on intense and narrow (23 meV) emission from single QDs grown on a vicinal substrate. Polarization measurements reveal an exciton splitting of 15 μeV. The good optical properties of these dots, together with the self alignment induced by the growth technique could allow for experiments involving multiple, and possibly coupled, QDs. We show that the substrate misorientation angle can be used as an extra parameter to control the quantum dot density and geometry, without compromising their optical properties.
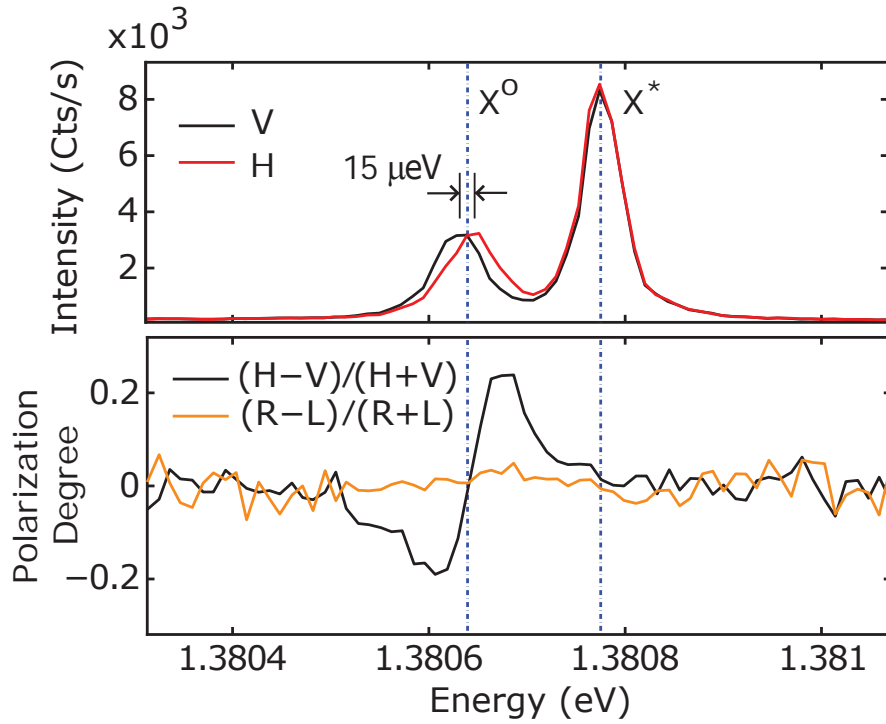
Figure 8.3: a) PL intensity for two orthogonal linear polarizations: horizontal (H) and vertical (V). The two components of the low energy peak are separated in energy by 15 μeV and are attributed to a neutral exciton (X°). The high energy peak is not split and can therefore be attributed to a charged exciton (X*) b) Degree of linear (circular) polarization in black (orange).

Leo Kouwenhoven for support.

Chapter 9

Controlled Aharonov-Bohm oscillations with a single neutral exciton

F. Ding, B. Li, N. Akopian, U. Perinetti, A. Govorov,

F. M. Peeters, C. C. Bof Bufon, C. Deneke, S. Kiravittaya,

Y. H. Chen, A. Rastelli, V. Zwiller & O. G. Schmidt

The Aharonov-Bohm effect [112] modifies the wave function phase $\Delta\varphi$ of a charged particle traveling around a region enclosing a magnetic field. During the 50 years since its discovery, this effect has made a significant impact on the development of physics [113]. The AB effect has been observed independently for electrons and holes in micro-/nanoscale structures [114, 115, 116]. For an electron-hole pair (i.e., a neutral exciton) confined in specially-designed nanostructures, the phases accumulated by the two species will be different after one revolution, leading to modulations between different quantum states [117, 118]. However the experimental optical observation of such effect has so far been limited to quantum ring ensembles [119, 120, 121]. Here we demonstrate Aharonov-Bohm oscillations in the photoluminescence energy and intensity of a *single* neutral exciton confined in a semiconductor quantum ring. Moreover, we control the period of the oscillations with a gate potential that modifies the exciton confinement. This novel control on the optical properties of a quantum ring provides fresh opportunities for exciton storage in quantum information schemes [122, 123].

The results in this chapter will be submitted for publication.

9.1 Introduction

Recent experimental works on the Aharonov-Bohm (AB) effect in ring-like semiconductor structures include magneto-transport measurements on a single quantum ring (QR) fabricated by local oxidation with atomic force microscope (AFM) [116], far-infrared spectroscopy [124], and magnetization spectroscopy [125] on self-assembled InGaAs nanorings epitaxially grown by Stranski-Krastanow (SK) mode. Theoretical investigations have predicted that in semiconductor quantum rings with a confined exciton, the AB effect can be probed from the photoluminescence (PL) emission, since the change in the phase of the wave function is accompanied by a change in the exciton total angular momentum, making the PL emission magnetic field dependent [117, 126, 127, 128, 118, 129]. Bayer *et al.* reported for the first time this effect for a *charged exciton* confined in a lithography defined QR [130]. PL emission from indirect excitons in stacked ZnTe/ZnSe *ensemble* quantum dots (QDs) shows similar oscillations [120], this behavior was explained by the type-II band alignment which confines one carrier inside the QD and the other carrier in the barrier, mimicking a QR-like structure.

We stress that these observations are mainly governed by single charges, e.g., electrons. The AB effect can also be observed for an electron-hole pair (a neutral exciton) on condition that in a ring-like structure the electron and hole move over different paths, resulting in a nonzero electric dipole moment [117]. Considering the relatively small electron-hole separation, the quest for the AB effect in a *single* neutral exciton in a type-I system is challenging. An in-plane electric field could possibly increase the polarization of an exciton and enhance the exciton AB effect [131]. Recently, Fischer *et al.* suggested that the exciton AB effect in a quantum ring can be dynamically controlled by a combination of magnetic and electric fields, a new proposal to trap light [122, 132].

We report here on the magneto-PL study of a single self-assembled semiconductor quantum ring fabricated by *in situ* AsBr$_3$ etching [133]. Due to a radial asymmetry in the effective confinement for electrons and holes, we expect the neutral exciton AB effect. Here we present data on the AB-type oscillations in a single neutral exciton, which is in agreement with previous theoretical predictions. We will also show, for the first time, that a vertical electrical field is able to control this quantum interference effect.

9.2 Sample fabrication

The sample is grown in a solid-source molecular-beam epitaxy system equipped with an AsBr$_3$ gas source. Low density SK InGaAs QDs are first grown and

capped with a 10 nm thick GaAs layer. AsBr$_3$ etching gas is then supplied. Strain-enhanced etching results in the preferential removal of the central part of the buried QDs and the spontaneous formation of ring-like structures [133] [Fig. 9.1(a)]. By varying the nominal etching depth, the morphology of the ring structure can be tuned. Some of the QRs are embedded in an n-i-Schottky structure, consisting of a 20 nm n-doped GaAs layer followed by a 20 nm thick spacer layer under the QRs, 30 nm i-GaAs and a 116 nm thick AlAs/GaAs short period superlattice. With a semi-transparent Ti top gate and a Cr/Au alloyed back gate, a vertical electric field can be applied to modify the electrostatic potential and to control the number of electrons in the ring [134]. Successive charging of a QR by up to two extra electrons is observed in our experiment.

The 3D morphology of *buried* InGaAs QRs is observed by removal of the GaAs cap layer by selective wet chemical etching followed by AFM imaging [133]. A cross sectional transmission electron microscopy (TEM) image of a single QR is also presented [Fig. 9.1(a)]. For the ring studied here (*nominal* etching depth of 3 nm), the inner radius r_1 is about 8.5 nm, an average outer radius r_2 about 19 nm, and a reduced height H about 4 nm. The inner height h is less than 1 nm [inset of Fig. 1(a)].

9.3 AB effect: quantum rings vs. quantum dots

Low temperature PL probes the energy changes and intensity changes related to the nature of the ground state. Figure 9.1(a) shows a typical PL spectrum for a single QR at B=0 T. The neutral exciton X, the biexciton XX, and the charged excitons X$^-$ and X$^+$ were identified by power-dependent PL, polarization-dependent PL, and charging experiments [134]. A magnetic field up to 9 T is applied along the sample growth direction. The evolution of a single QR PL emission with increasing B is shown in Fig. 9.1(b). For comparison we also present data for a conventional InGaAs QD [Fig. 9.1(c)] with a height of about 3 nm. Unlike for QR ensembles [120, 121], the characteristic Zeeman splitting as well as the diamagnetic shift of the PL emission energy for both samples are observed, similar to previous reports on single QRs [135]. A significant feature observed for the QR sample is the decrease in PL intensity with increasing magnetic field, in direct contrast to the constant PL intensity from the reference QD. The change in PL intensity is one of the signatures expected for a QR and is attributed to oscillations in the ground state transitions [117, 119, 120, 121].

The exciton emission energy in a magnetic field can be described by $E_{PL} = E_0 \pm \frac{1}{2}|$g*$|\mu B + \gamma_2 B^2$. Here $|$g*$|$ is the effective exciton Landé factor, μ is the Bohr
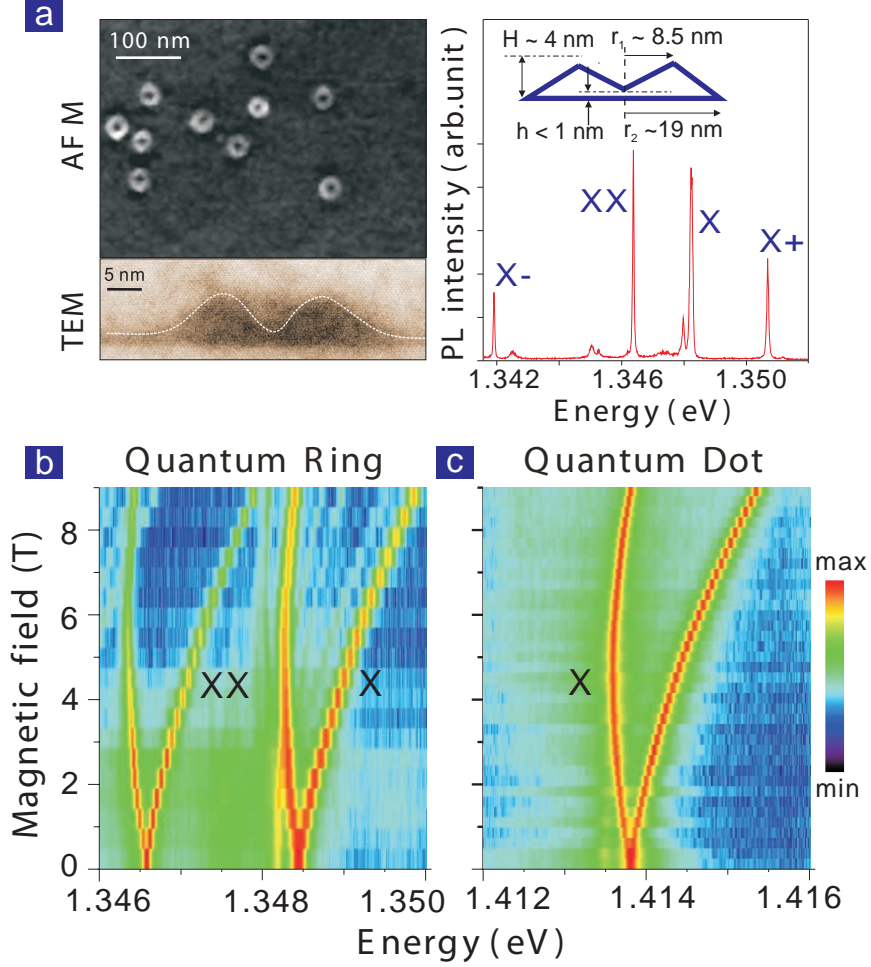
Figure 9.1: (a) AFM image of the QRs shown together with the cross sectional TEM image of a single QR. PL spectrum of a single QR (with a nominal etching depth of 3 nm) is shown in the right. The inset presents the structure parameters. (b), (c) Color-coded maps of the logarithm of the PL intensity as a function of magnetic field and PL energy. For comparison, data for a single QD are shown in (c).

magneton and γ_2 is the diamagnetic shift coefficient. We plot the *neutral* exciton emission energies of the QR and the QD after averaging the Zeeman splitting. For the QR, the emission energy does not scale quadratically with increasing B field, instead it shows two cusps [indicated by arrows in Fig. 9.2(a)] (to see this clearly, we fit the data with three parabolas). To better visualize the oscillation, we subtract a single parabola from Fig. 9.2(a) and plot the results in Fig.9.2(c). In correspondence to the two maxima at $\sim$4 T and $\sim$7 T, the normalized integrated PL intensity also shows two knees [Fig. 9.2(e)], suggesting changes in the ground
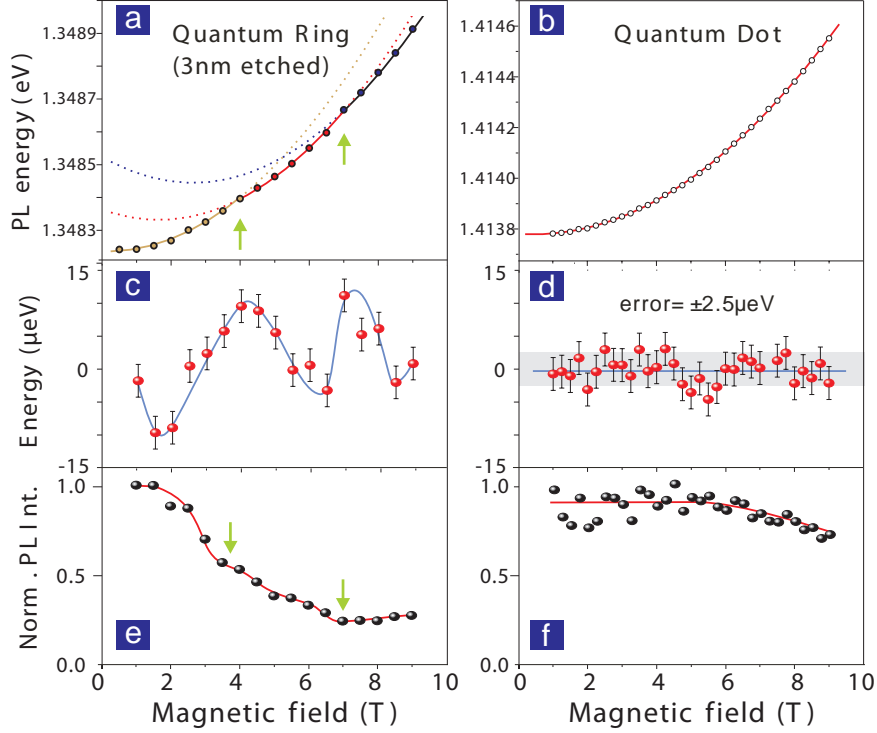
Figure 9.2: Fitted PL peak position versus B field after averaging the Zeeman split-ting for a QR (a) and a QD (b) neutral exciton emission. The lines are the quadratic fits. Oscillations in PL energy for the 3 nm etched QR and corresponding normalized PL intensity as a function of B field are shown in (c) and (e), respectively. For a refer-ence QD, the neutral exciton shows no energy oscillation (d) within an error region of ± 2.5 μeV (gray area), and also the normalized PL intensity shows no clear quenching (f). The solid lines are guide to the eye.

state transitions. This observation strongly contrasts with that of a conventional QD, as shown in Figs. 9.2(b), (d) and (f), where no oscillations in PL energy and no quenching behavior in the PL intensity are seen.

9.4 Electrically tuned AB effect

The dynamic control of this AB behavior with an external electric field is of great interest for the creation of an exciton-based integrated circuit [122]. We demonstrate this possibility with a gated QR-structure, see Fig. 9.3(a). The AB oscillations for a single QR under a forward bias of 2.8 V are clearly seen in Fig. 9.3(b), with the two transition points at 2.6 T and 8 T. Remarkably, when the bias is decreased from 2.8 V to 0.8 V, the transition points shift smoothly
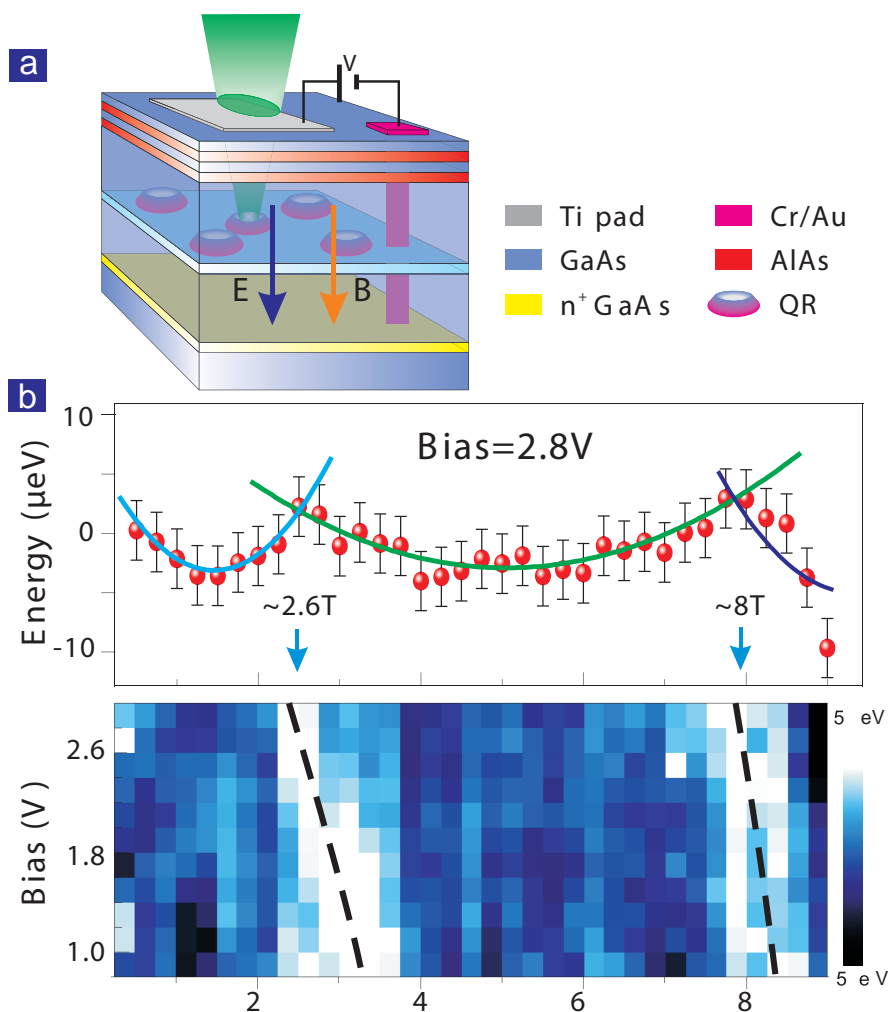
Figure 9.3: (a) Schematic of the gated QR-structure. (b) Under a forward bias of 2.8 V the emission energy shows clear transitions at 2.6 T and 8 T (upper part). When the bias changes from 2.8 V to 0.8 V, the transitions shift smoothly (lower part).

to higher magnetic fields [Fig. 9.3(b)], indicating that the effective radii of the electron and the hole are modified by the external gate potential. The desired control over the single exciton recombination can be achieved, as we conclude from the changes in the PL intensity, by appropriate tuning of either external magnetic or electric fields.

9.5 Discussion

9.5.1 theoretical model

In the following we give a comprehensive description of how the combination of external magnetic and electric field affects the behavior of a single neutral exciton confined in a QR. Although an elaborate calculation should involve the presence of a wetting layer, azimuthal anisotropy [136] and structural asymmetry [135], we model a simplified QR as depicted in Fig. 9.1(a) with the main aim to explain the gate-controlled AB effect (Fig. 9.3). The full Hamiltonian of the exciton within the effective mass approximation is given by

$$H_{tot} = H_e + H_h + V_c\left(\vec{r}_e - \vec{r}_h\right), \tag{9.1}$$

with

$$H_{tot} = \left(\vec{P}_j + q_j\vec{A}_j\right)\frac{1}{2m_j}\left(\vec{P}_j + q_j\vec{A}_j\right) + \delta E_j(\vec{r}_j) + V_j(\vec{r}_j) + q_jEz_j, \tag{9.2}$$

where $V_j(\vec{r}_j)$ is the confinement potential of the electron (hole) due to the band offset of the two materials, which is different for the inner and outer edge of the ring. $V_c\left(\vec{r}_e - \vec{r}_h\right) = -e^2/4\pi\varepsilon\left|\left(\vec{r}_e - \vec{r}_h\right)\right|$ is the Coulomb potential between the electron and the hole, and $\delta E_j(\vec{r}_j)$ is the strain-induced shift to the band offset which depends on the hydrostatic component of the strain tensor ϵ_{ij}. Here the piezoelectric potential is not taken into account since it is negligible as compared to the other terms. The last term of Eq. (9.2) is the potential energy in the presence of the vertical electric field E. Here the total angular momentum is a good quantum number and should be conserved, thus the exciton wave function with total angular momentum L can be written as $\Psi_L\left(\vec{r}_e, \vec{r}_h\right) = \sum_k C_k\Phi_k\left(\vec{r}_e, \vec{r}_h\right)$, where $\Phi_k\left(\vec{r}_e, \vec{r}_h\right) = \psi_{n_e,l_e}\left(\vec{r}_e\right)\psi_{n_h,l_h}\left(\vec{r}_h\right)$ with $l_e + l_h = L$. By diagonalizing the obtained matrix we find the exciton energy levels and their corresponding wave functions. In order to observe the AB oscillation clearly, we give the results of the second derivative of the exciton total energy with respect to the magnetic field. The minima of this quantity corresponds to changes in the ground state [118].

The results for four different values of the electric field are shown in Fig. 9.4(a). Here we only give the results of the exciton states with $L = 0$, as the calculation showed that the $L = 0$ state is always the ground state and is optically active. From Fig. 9.4(a) we notice two oscillations within the given B-range. The indium composition inside the ring and the large lattice mismatch between the ring and barrier materials result in a considerably large strain, and this strain has a different effect on the electron and hole confinement potential (makes the hole confined in the top area of the ring and the electron confined in the center of the ring). The
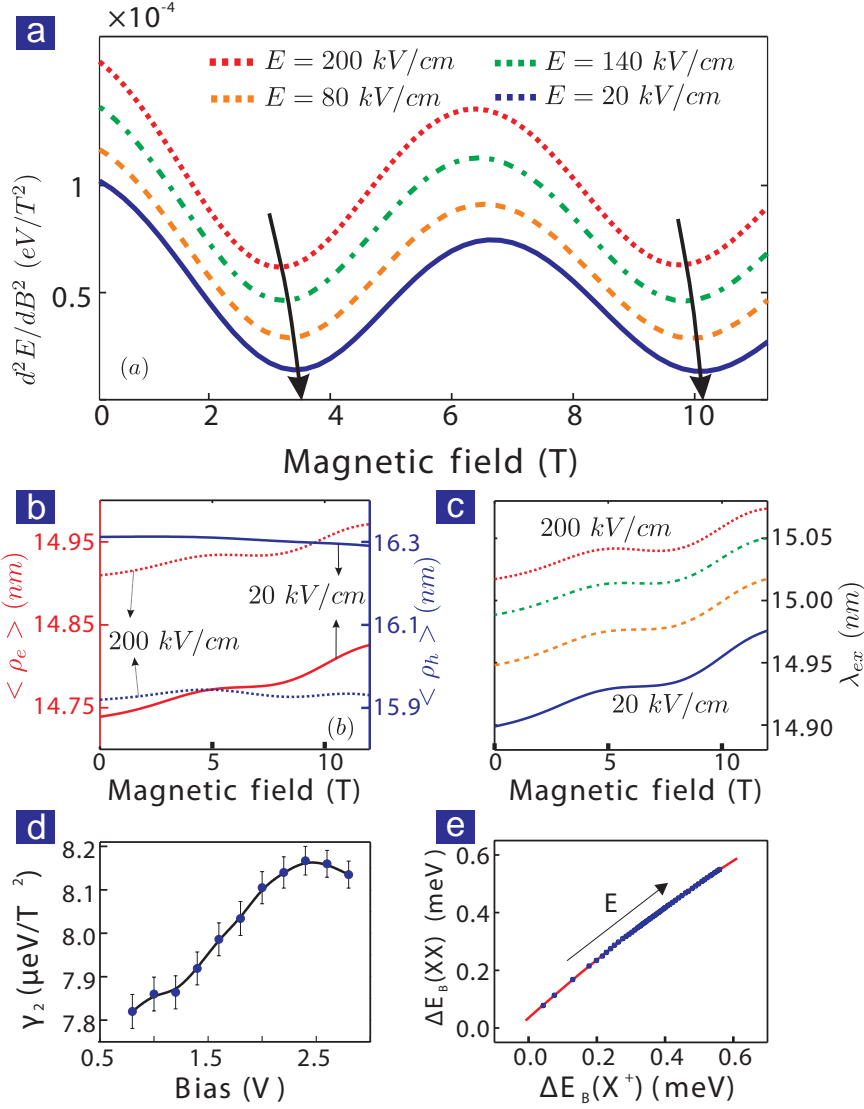
Figure 9.4: (a) Second derivative of the exciton energy of the state with $L = 0$. Calculations are shown for four different values of the electric field. (b) The effective radius of the electron and the hole, defined as $\int \Psi_L^* (\vec{r}_e, \vec{r}_h) \rho_{e(h)} \Psi_L (\vec{r}_e, \vec{r}_h) \, d\vec{r}_e d\vec{r}_h$. (c) The radius $\lambda_{ex} = \left((m_h + m_e)/(m_h/ < \rho_e >^2 + m_e/ < \rho_h >^2) \right)^{0.5}$, which corresponds to the exciton radius definition for a 3D system. (d) The diamagnetic coefficient γ_2 changes with applied bias. (e) The binding energies of XX and X^+ change by nearly the same amount with external E field.

two oscillations within $B = 10$ T come from the angular momentum transitions of the main contributing single particle basis function in the total exciton wave function. With increasing magnetic field from $B = 0$ to $B = 10$ T, the angular

momentum pair (l_e, l_h) in the state $\Phi_k(\vec{r}_e, \vec{r}_h)$ which has the largest contribution to the total wave function $\Psi_L(\vec{r}_e, \vec{r}_h)$ changes from (0, 0) to (-1, 1) and then from (-1, 1) to (-2, 2). The most important finding is that by decreasing the electric field from 200 kV/cm to 20 kV/cm, the two transitions shift to higher B field (indicated by black arrows), which reproduces the shift trend in Fig. 9.3(b).

For a better understanding of this effect we study the effective radius of the electron (hole) $< \rho_e >$ ($< \rho_h >$) as defined by $\int \Psi_L^*(\vec{r}_e, \vec{r}_h)\rho_{e(h)}\Psi_L(\vec{r}_e, \vec{r}_h)\, d\vec{r}_e d\vec{r}_h$ (which represents the electron and hole positions inside the ring). From Fig. 9.4(b) we know that with decreasing the vertical electric field from 200 kV/cm to 20 kV/cm, the electron is attracted to the bottom area of the ring, decreasing its effective radius, while the hole is pushed to the top of the ring and its effective radius increases. From the change of $< \rho_e >$ and $< \rho_h >$ alone we can not conclude that the period of the Aharonov-Bohm oscillation decreases. Theoretical study reveals that the oscillation comes from a change in the value of the angular momentum pair (l_e, l_h), not from the single electron or hole angular momentum. The period of the oscillation is not only related to the effective radius of the electron and the hole, but also to their effective masses.

We find that the magnetic field at which the first transition takes place is proportional to $\hbar/e\lambda_{ex}^2$, where $1/\lambda_{ex}^2 = (m_h/ < \rho_e >^2 + m_e/ < \rho_e >^2)/(m_e + m_h)$. We plot λ_{ex} as a function of magnetic field for different values of electric field in Fig. 9.4(c). Because the effective mass of the hole is much larger than the one of the electron (also because the electron and the hole radius changes within the same order), λ_{ex} should have a similar behavior as the electron effective radius $< \rho_e >$. This is clearly observed in Fig. 9.4(c) and λ_{ex} decreases monotonously with decreasing electric field. As a result, the first transition takes place at a higher magnetic field when we decrease the electric field [see Fig. 9.3(b)]. In fact, λ_{ex} should be proportional to the diamagnetic coefficient, which explains why we observe in the experiment an increase of γ_2 with external bias [see Fig. 9.4(d)]. The explanation for the second transition is similar, although the formula for the magnetic field at which it takes place is different (also it has the dominat term $m_h/ < \rho_e >^2$), which shifts to higher magnetic field when the electric field decreases.

9.5.2 AB effect for charged exciton complexes

It is worth mentioning that for the studied QRs we do not observe substantially different oscillation behaviors for charged exciton complexes. This is somehow surprising, because intuitively one expects that picture a charged exciton (e.g., X^+) should be more sensitive to the AB effect than the neutral exciton. This is be-

cause the exciton complexes confined in our QR are in the strongly confined few-particle regime (in other words, the exciton complexes are not tightly bound) and the inter-particle Coulomb interactions are perturbations to the single-particle energy. The reason is as follows. By studying magneto-PL of different exciton complexes, Tsai *et al.* [137] found that the diamagnetic coefficient $\gamma_2(XX) \approx \gamma_2(X^+)$ in small QDs, and they argued that this should be observable in strongly confined few-particle systems where the electron and hole wave functions have different lateral extents. Recently a similar effect has been reported on small QDs under biaxial strain [138], where the binding energies E_B of both XX and X^+, defined as the energy difference between XX (X^+) and X, change by nearly the same amount with external mechanical stress. Here we observe the same effect in the presence of E field, see Fig. 9.4(e). When the E field on the QR increases, the changes in the binding energies $\Delta E_B(XX) \approx \Delta E_B(X^+)$, indicating that the strongly confined few-particle picture is valid in our QRs and, the effective radii of electron and hole are very different.

9.6 Conclusions

In conclusion, we have presented a controlled neutral exciton AB effect in an AsBr$_3$ *in situ*-etched single semiconductor QR. The effective radii of the electron and hole wave functions are different in these volcano-shape QRs, giving rise to a non-zero net magnetic flux, hence the observation of oscillations in the exciton PL energy and PL intensity in a magnetic field. The optical AB effect can be controlled by applying a vertical electric field. The subtleties of the experimental results are explained by a microscopic model of how a single exciton behaves under the combination of magnetic and electric fields. Further experiments will focus on the utilization of a lateral electric field to further increase the polarization of an exciton, hence the enhancement of the AB effect. We envision that a single exciton memory can be realized based on the optical AB effect for a neutral exciton that we have demonstrated here [122, 123].

Chapter 10

Aharonov-Bohm Oscillations

N. Akopian, U. Perinetti &, V. Zwiller

This chapter present a simple model of a neutral exciton in a quantum ring. We consider an electron and a hole which are constrained on two circles of different radius and we calculate the effects of an external magnetic field, together with the Coulomb interaction between the two particles. Although this model is a strong simplification of the actual problem presented in the previous chapter it qualitatively reproduces the measured effects and serves as a simplified simulation model to illustrate Aharonov-Bohm oscillations in the case of a neutral exciton. In particular it shows what are the roles of different confinement of electron and hole and of Coulomb interaction.

10.1 Model

In order to grasp the behavior of a neutral exciton in a magnetic field we used a simple model in which the electron and the hole are described by one-dimensional wavefunctions on a ring. In the structure studied in chapter 9 the electron and the hole have different effective radii making it possible to have Aharonov-Bohm effect for a neutral exciton at the relatively low magnetic fields achievable in our experiments. We introduced this difference in confinement by assuming that the circles on which the electrons and holes wave functions are defined have different radii R_e and R_h.

Within this assumptions the neutral exciton Hamiltonian consists of the kinetic terms for the two particles and by the Coulomb interaction between them (bold letters are used to indicate vectors):

$$\hat{H} = \frac{(\mathbf{p}_e + e\mathbf{A})^2}{2m_e} + \frac{(\mathbf{p}_h - e\mathbf{A})^2}{2m_h} - V_{eh}(\mathbf{r}_e, \mathbf{r}_h), \tag{10.1}$$

where the coupling to a magnetic field is taken into account in the minimal coupling terms. In the case of a magnetic field orthogonal to the plane of the quantum ring, we can write the vector potential as $\mathbf{A} = \frac{1}{2}\mathbf{B} \times \mathbf{r}$ and the Hamiltonian can be rewritten as

$$\hat{H} = \hat{T}_e + \hat{T}_h + \hat{V}_{eh} = \tag{10.2}$$

$$= \sum_{n=e,h} \frac{\hbar^2}{2m_n R_n^2}\left(-i\frac{\partial}{\partial\theta_n} \pm N_n\right)^2 + V_{eh}(x - y) \tag{10.3}$$

Where $N_n = \frac{\pi B R^2}{h/e}$ is the number of flux quanta threading the ring of particle n. We indicated with x, y the angular positions of the electron and hole respectively.

In order to solve this problem numerically, we take as basis for the single particle states the angular momentum eigenstates:

$$|k_n\rangle = \frac{1}{\sqrt{2\pi}}e^{ik_n\phi_n}, \tag{10.4}$$

and we calculate the matrix elements of the exciton Hamiltonian on product states $|k_e\rangle|k_h\rangle$:

$$\left\langle k_{e2}k_{h2}\left|\hat{H}\right|k_{e1}k_{h1}\right\rangle = \left\langle k_{e2}k_{h2}\left|\hat{T}_n\right|k_{e1}k_{h1}\right\rangle - \langle k_{e2}k_{h2}|V_{eh}|k_{e1}k_{h1}\rangle \tag{10.5}$$

Using the fact that states $|k_n\rangle$ are eigenstates of $\frac{\partial}{\partial\phi}$ with eigenvalue k_n and they are orthogonal to each other, we can immediately see that
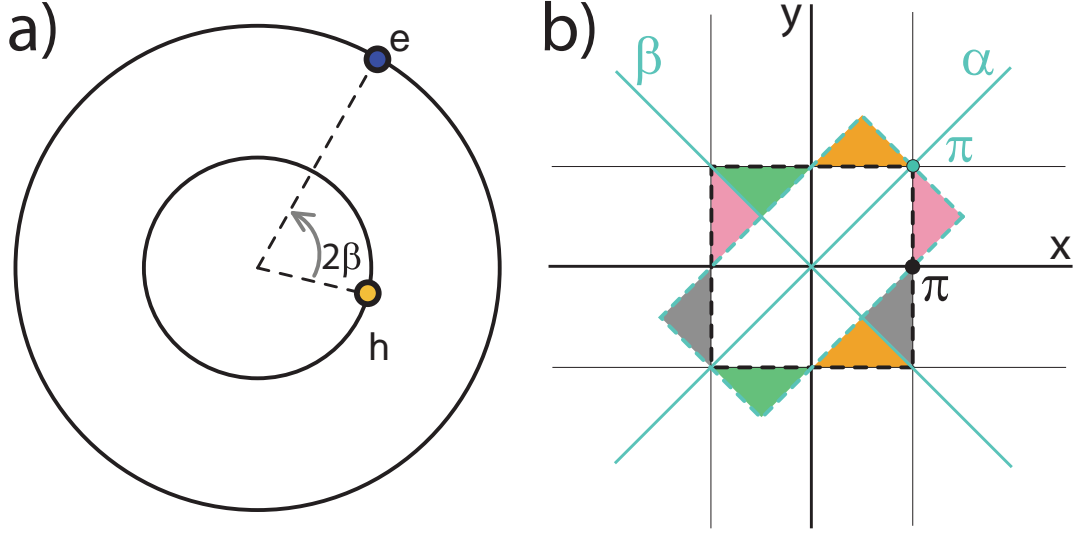
Figure 10.1: (a) Ring model. The hole and the electron are confined in circles of different radius, R_e for the electron and R_h for the hole. We call 2β the difference between the angles x and y indicating the positions of the electron and the hole, respectively. **(b) Domain of integration.** We draw the domains of integration related to the change of variables of equation 10.7. The two domains of integration for x, y (black dashed line) and α, β (blue dashed line) are equivalent. Equivalent regions are marked with the same color.

$$\left\langle k_{e2}k_{h2} \left| \left(\hat{T}_e + \hat{T}_h\right) \right| k_{e1}k_{h1} \right\rangle =$$
$$= \left[\frac{\hbar^2}{2m_e R_e^2} \left(k_{e1} \pm N_e\right)^2 + \frac{\hbar^2}{2m_h R_h^2} \left(k_{h1} \pm N_h\right)^2 \right] \delta_{k_{e1},k_{e2}} \delta_{k_{h1},k_{h2}}. \qquad (10.6)$$

In order to calculate the matrix elements of the Coulomb interaction term, it is convenient to use the fact that V_{eh} only depends on the angle $x - y$ between the two particles. We therefore introduce a change of variables:

$$\alpha \equiv \frac{x+y}{2}, \qquad \beta \equiv \frac{x-y}{2}. \qquad (10.7)$$

Considering that the Jacobian of this transformation is $J = 2$ and transforming the domain of integration as in Fig.10.1(b) we have:

97

$$\langle k_{e2}k_{h2} \left| V_{eh} \right| k_{e1}k_{h1} \rangle =$$

$$= \int\limits_{-\pi}^{\pi} \int\limits_{-\pi}^{\pi} \frac{1}{4\pi^2}\, e^{-i(k_{e2}x+k_{h2}y)}\, V_{eh}\, e^{i(k_{e1}x+k_{h1}y)}\, \mathrm{d}x\, \mathrm{d}y =$$

$$= \frac{1}{4\pi^2} \int\limits_{-\pi}^{\pi} e^{i[(k_{e1}+k_{h1})-(k_{e2}+k_{h2})]\alpha}\, \mathrm{d}\alpha \int\limits_{-\frac{\pi}{2}}^{\frac{\pi}{2}} e^{i[(k_{e1}-k_{h1})-(k_{e2}-k_{h2})]\beta} V_{eh}(\beta) \cdot J\, \mathrm{d}\beta$$

$$= \frac{1}{2\pi} \delta_{k_{e1}+k_{h1},\, k_{e2}+k_{h2}} \int\limits_{-\frac{\pi}{2}}^{\frac{\pi}{2}} e^{i[(k_{e1}-k_{h1})-(k_{e2}-k_{h2})]\beta} V_{eh}(\beta) \cdot 2\, \mathrm{d}\beta.$$

Since $V_{eh}(\beta)$ is an even function and the integral in β is over a symmetric interval around zero, the previous expression simplifies to:

$$\left\langle k_{e2}k_{h2} \left| \hat{V}_{eh} \right| k_{e1}k_{h1} \right\rangle = \tag{10.8}$$

$$= \frac{1}{2\pi} \delta_{k_{e1}+k_{h1},\, k_{e2}+k_{h2}} \cdot 2 \int\limits_{0}^{\frac{\pi}{2}} \cos(\underbrace{[(k_{e1}-k_{h1})-(k_{e2}-k_{h2})]}_{D} \beta)\, V_{eh}(\beta) \cdot 2\, \mathrm{d}\beta.$$

As we can see from the Kroneker delta these matrix elements are non zero only between states such that $k_{e1}+k_{h1} = k_{e2}+k_{h2}$ and this allows to rewrite the argument D in equation 10.8 as $2(k_{e2}-k_{h2})$. We can finally replace V_{eh} with its explicit form, written as a function of $\gamma = 2\beta$,

$$V_{eh}(\gamma) = \frac{e^2}{4\pi\epsilon_0\epsilon_r} \frac{1}{\sqrt{(R_e\cos 2\gamma - R_h)^2 + (R_e\sin 2\gamma)^2}},$$

and obtain a compact form for the Hamiltonian matrix elements:

$$\left\langle k_{e2}k_{h2} \left| \hat{H} \right| k_{e1}k_{h1} \right\rangle =$$

$$= \delta_{k_{e1},k_{e2}} \delta_{k_{h1},k_{h2}} \cdot \frac{\hbar^2}{2m_n R_n^2} \cdot (k_{n1} \pm N_n)^2 - \tag{10.9}$$

$$\frac{1}{2\pi} \delta_{k_{e1}+k_{h1},\, k_{e2}+k_{h2}} \cdot \frac{e^2}{4\pi\epsilon_0\epsilon_r} \cdot 2 \int\limits_{0}^{\pi} \frac{\cos((k_{h1}-k_{h2})\gamma)}{\sqrt{(R_e\cos\gamma - R_h)^2 + (R_e\sin\gamma)^2}}\, \mathrm{d}\gamma.$$

In order to make this expression more readable we can rewrite it as a function of the ratio between the electron and hole effective masses and ring radii.

$$\eta = \frac{m_h}{m_e}, \qquad \rho = \frac{R_h}{R_e}. \tag{10.10}$$

$$\left\langle k_{e2} k_{h2} \left| \hat{H} \right| k_{e1} k_{h1} \right\rangle =$$

$$= \ \delta_{k_{e1}, k_{e2}} \delta_{k_{h1}, k_{h2}} \ \cdot \frac{\hbar^2}{2 m_e R_e^2} \cdot (k_{e1} + N_e)^2 +$$

$$\delta_{k_{e1}, k_{e2}} \delta_{k_{h1}, k_{h2}} \ \cdot \frac{\hbar^2}{2 m_e R_e^2} \cdot \frac{1}{\eta \rho^2} \cdot (k_{h1} - N_h)^2 - \quad (10.11)$$

$$\frac{1}{2\pi} \delta_{k_{e1}+k_{h1}, \, k_{e2}+k_{h2}} \ \cdot \frac{e^2}{4\pi\epsilon_0\epsilon_r} \cdot \frac{1}{R_e} \cdot 2 \int_0^\pi \frac{\cos((k_{h1}-k_{h2})\gamma)}{\sqrt{(\cos\gamma - \rho)^2 + (\sin\gamma)^2}} \, \mathrm{d}\gamma.$$

We can further simplify this expression by using the exciton Bohr radius a_μ and the exciton Rydberg energy E_μ as length and an energy scales, respectively. This allows to define a dimensionless Hamiltonian

$$\tilde{H} \equiv \frac{\hat{H}}{E_\mu}, \qquad E_\mu = \frac{\mu e^4}{2\left(4\pi\epsilon_0\epsilon_r\hbar\right)^2}, \quad (10.12)$$

whose matrix elements are given by:

$$\left\langle k_{e2} k_{h2} \left| \tilde{H} \right| k_{e1} k_{h1} \right\rangle =$$

$$= \ \delta_{k_{e1}, k_{e2}} \delta_{k_{h1}, k_{h2}} \ \cdot \frac{1}{\tilde{R}^2} \cdot \frac{\eta}{1+\eta} \cdot \left[(k_{e1} + N_e)^2 + \frac{1}{\eta\rho^2} (k_{h1} - N_h)^2 \right] -$$

$$2 \frac{1}{2\pi} \delta_{k_{e1}+k_{h1}, \, k_{e2}+k_{h2}} \ \cdot \frac{1}{\tilde{R}} \cdot 2 \int_0^\pi \frac{\cos((k_{h1}-k_{h2})\beta)}{\sqrt{(\cos\beta - \rho)^2 + (\sin\beta)^2}} \, \mathrm{d}\beta, \quad (10.13)$$

where

$$\tilde{R} \equiv \frac{R_e}{a_\mu}, \qquad a_\mu = \frac{4\pi\epsilon_0\epsilon_r\hbar^2}{\mu e^2} \quad (10.14)$$

and $\mu = \dfrac{m_e m_h}{m_e + m_h}$ is the reduced mass of the exciton.

10.2 Simulations

We diagonalized the system Hamiltonian (eq. 10.12) numerically considering states with wavenumbers k ranging from $k = -k_{max} = -10$ to $k = k_{max} = 10$. In order to make sure that we are not restricting ourselves to a too small subspace, we studied how the energy of the ground state changes for different Hilbert spaces

spanned by states with k in [-n, n]. In this way we could see that the ground state energy does not change appreciably by increasing n from 8 to 10.

The results of the calculations with the material parameters of GaAs are shown in Figure 10.2 where we plot how the ground state energy changes as a function of magnetic field, for different values of the electron and hole radii. Oscillations of some tens of μeV are clearly visible in some of the plots and correspond to transitions between states with different total angular momentum.

Transitions between different states with the same total angular momentum do not give rise, in our model, to oscillations on this energy scale. They are much smoother transitions as the electron-hole state is always a superposition of states with given electron and hole angular momentum. An example of this is given in Figure 10.3 for the case of $R_e = 15$ nm and $R_h = 16$ nm. We can see that, at zero magnetic field, the main component to the ground state is $|k_e, k_h\rangle = |0, 0\rangle$ which is heavily mixed with other $|-n, n\rangle$ states by Coulomb interaction. As the magnetic field increases, the amplitudes of the different states change and, at about 2.8 T, the state $|-1, 1\rangle$ becomes the dominant one. Another transition of this kind takes place around $B = 8.6$ T, where the state $|-2, 2\rangle$ becomes dominant. The field values of 2.8 T and 8.6 T at which the transitions occur are in reasonably good agreement with the more elaborate model presented in the previous chapter.
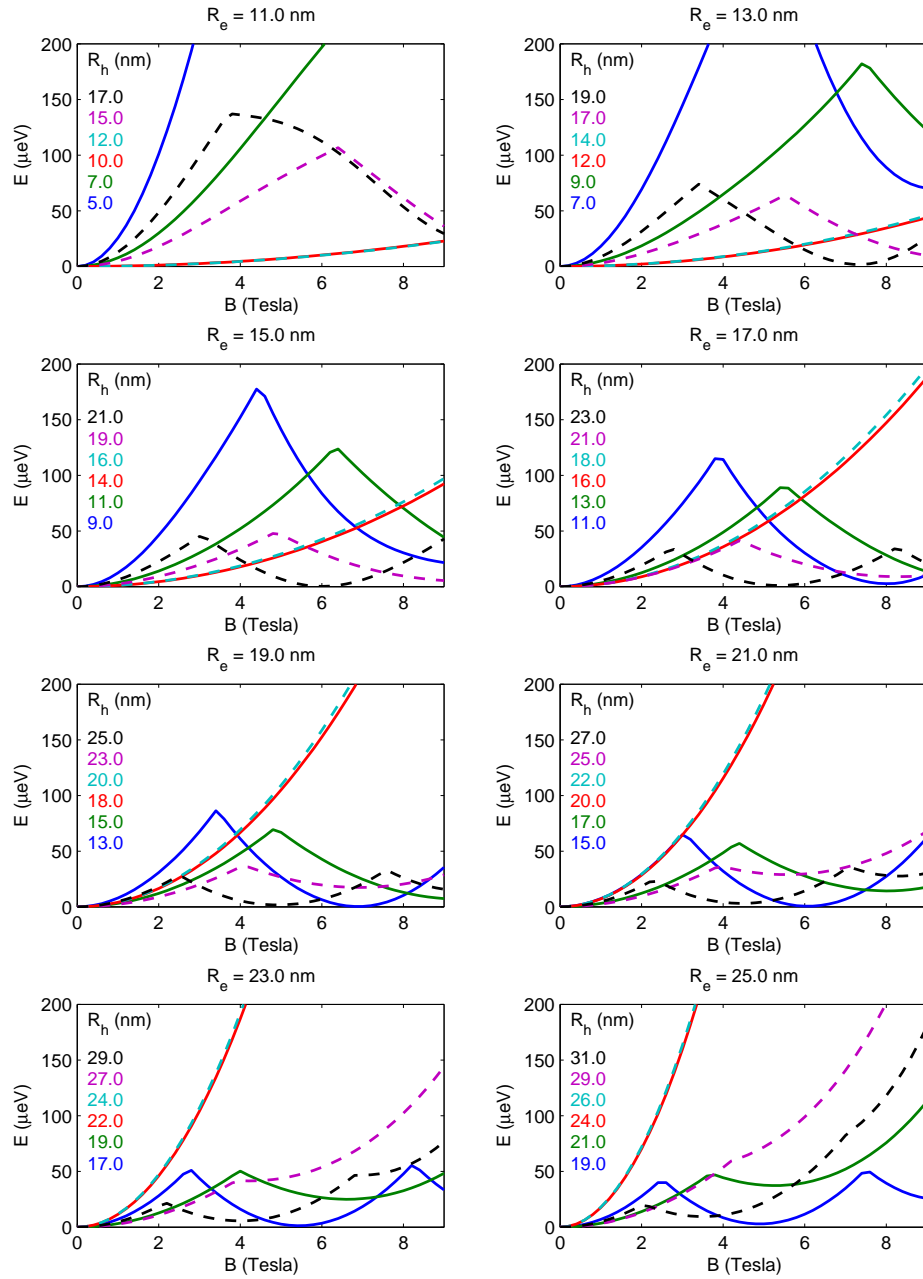
Figure 10.2: Changes in exciton energies as a function of B field. Calculations based on the material parameters of GaAs. Each panel corresponds to the electron being on a circle of radius R_e and to different values for the hole radius Rh. The energies are plotted as solid (dashed) lines for $Re > Rh$ ($Re < Rh$).
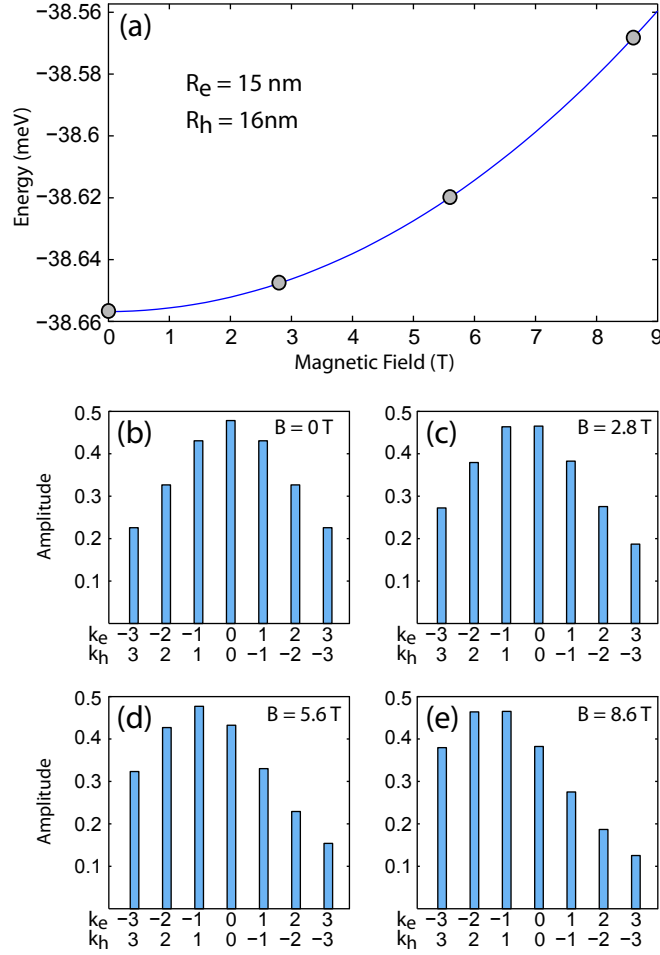
Figure 10.3: Amplitudes on $|k_e, k_h\rangle$ states. (a) Exciton energy as a function of B field for Re = 15 nm and Rh = 16 nm. **(b, c, d, e)** Amplitudes on the states that mostly contribute to the exciton ground state at the magnetic field values indicated in (a).

Chapter 11

Two photon interference

U. Perinetti, N. Akopian, G. S. Solomon & V. Zwiller

In this chapter we present an experimental realization of two-photon interference using photons emitted by an InAs quantum dot under pulsed laser excitation. We interfered photons emitted with a time separation of 5.7 ns and brought together at the same time on a 50:50 beam splitter by means of delay lines. We excited the quantum dot via the InAs wetting layer and directly in a high-energy shell obtaining two-photon overlaps of 50% and 76% respectively. Autocorrelation measurements of the studied quantum dot transition revealed blinking on a time scale of hundreds of nanoseconds.

11.1 Introduction

Two photon interference, or Hong-Ou-Mandel effect, essentially consists in the fact that two indistinguishable photons impinging at the same time on opposite sides of a beam splitter will always be detected in the same output port [139].

This effect has no counterpart for classical light: it is not possible to interfere two classical sources at a beam splitter and have a joint detection probability at the two output below 0.5 [140].

Apart from being a nice exercise in quantum mechanics, two-photon interference is also a very powerful tool: it is the basic ingredient for different quantum information protocols, among which linear-optics quantum computation [15]and quantum teleportation [141].

Two-photon interference has been shown for different subpoissonian sources like parametric down-conversion [139], a single quantum dot [100], trapped ions [84], molecules [142, 143], donor impurities [85] and only recently for two independent quantum dots [144, 145].

This chapter presents the steps we took towards interfering photons from different dots and it shows interference of photons emitted at different times by one quantum dot.

11.2 Two-photon interference, theory

Two photon interference can be explained in a few equations if we restrict ourselves to identical photons that arrive simultaneously at the input ports of a beam splitter [146]. The photon states at the input and output ports of the beam splitter are linked by the following mapping:

$$\hat{a}^\dagger \rightarrow \frac{1}{\sqrt{2}}\left(\hat{c}^\dagger + \hat{d}^\dagger\right) \quad \text{and} \quad \hat{b}^\dagger \rightarrow \frac{1}{\sqrt{2}}\left(\hat{c}^\dagger - \hat{d}^\dagger\right), \tag{11.1}$$

where $\hat{a}^\dagger$, $\hat{b}^\dagger$ and $\hat{c}^\dagger$, $\hat{d}^\dagger$ are the creation operators of photons (in a given spatio-temporal mode) at the input and output ports respectively. So if two identical photons enter the beam splitter we have:

$$
\begin{aligned}
|1,1\rangle_{ab} = \hat{a}^\dagger\hat{b}^\dagger|0,0\rangle_{ab} \rightarrow & \\
\rightarrow \frac{1}{2}(\hat{c}^\dagger + \hat{d}^\dagger)(\hat{c}^\dagger - \hat{d}^\dagger)|0,0\rangle_{cd} = & \frac{1}{2}(\hat{c}^{\dagger 2} - \hat{d}^{\dagger 2})|0,0\rangle_{cd} \\
= \frac{1}{\sqrt{2}}(|2,0\rangle_{cd} - |0,2\rangle_{cd}), &
\end{aligned}
\tag{11.2}
$$

so that the photons are in a superposition of both leaving the beam splitter in port c and both leaving the detector in port d. No coincident detections can happen in this case (11.1).

If the input photons have orthogonal polarizations H and V they are perfectly distinguishable and they can be simultaneously detected at the two output ports:

$$
\begin{aligned}
|1,1\rangle_{ab} = \hat{a}^\dagger \hat{b}^\dagger |0,0\rangle_{ab} &\to \\
&\to \frac{1}{2}(\hat{c}_H^\dagger + \hat{d}_H^\dagger)(\hat{c}_V^\dagger - \hat{d}_V^\dagger)|0,0\rangle_{cd} \\
&= \frac{1}{2}(\hat{c}_H^\dagger \hat{c}_V^\dagger - \hat{c}_H^\dagger \hat{d}_V^\dagger + \hat{c}_V^\dagger \hat{d}_H^\dagger - \hat{d}_H^\dagger \hat{d}_V^\dagger |0,0\rangle_{c,d}) \\
&= \frac{1}{2}(|1_H 1_V, 0\rangle_{cd} - |1_H, 1_V\rangle_{cd} + |1_V, 1_H\rangle_{cd} - |0, 1_H 1_V\rangle_{cd}),
\end{aligned}
\tag{11.3}
$$

where the second and third terms do not cancel and can give detection events in the two output ports simultaneously in half of the detection events. In the following we present imperfect realizations of these two simplified cases. In particular, photons are not perfectly indistinguishable in our case: although we can can make sure that they have the same polarization we have little control on their energies as the energy of the studied transition slightly changes with time. This can be accounted for by associating different wave-packets to the two photons, so that the initial state can be written as:

$$
|\psi\rangle = \iint ds\, dt\, x(s)y(t)\hat{a}^\dagger(s)\hat{b}^\dagger(t)|0\rangle,
\tag{11.4}
$$

where $\hat{a}^\dagger(s)$, $\hat{b}^\dagger(t)$ create a photon at times s, t respectively. Applying the same transformations at the beams splitter as used above, it can be shown that the probability of detecting two photons at different output ports is $P = (1 - V)/2$, where $V = \langle | \int dt x(t)y^*(t)|^2 \rangle$ is the average overlap between the two wave-packets.
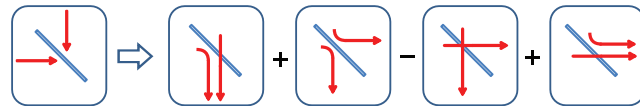
Figure 11.1: Two-photon interference. The cartoons on the right represent the superposition of states at the output of the beam splitter. The middle ones, corresponding to both photons being reflected or transmitted, are not distinguishable in the measurement. Having opposite signs, they cancel so that only states with two-photons at the same output are left.

11.3 Quantum Dot characterization

The quantum dots used in this experiment are InGaAs quantum dots in GaAs. They are grown inside an optical cavity defined by two Bragg mirrors. The cavity has a very big volume and does not change the lifetime of optical transitions. However it is of great use in this experiment as light emitted in resonance with the cavity is directed mostly orthogonally to the sample surface, towards the collection optics. This effectively gives a brighter photon source and allows to take photon correlation measurements in a reasonable time (minutes, hours).

We used an automated scanning routine to find dots that were bright enough for this experiment. We also selected dots based on their linewidth restricting ourselves to linewidths smaller than the resolution of our setup, which is about 30 μeV.
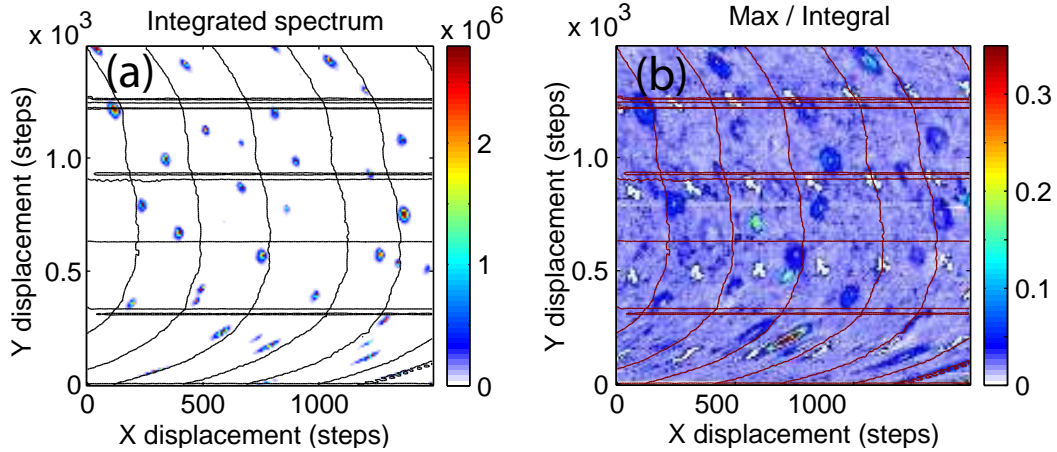
Figure 11.2: **(a)** Map of a region of the sample showing in color the integrated photoluminescence in the bandwidth in which quantum dots emit. Units are arbitrary. **(b)** Map of the same sample region as in the previous figure. Colors represent the ratio between the maximum and the integral of spectra taken at each point.

An example of automatic scan is shown in Fig.11.2. This was taken over an area of about $150x100$ μm^2, using a green laser. Panel (a) shows the integrated intensity over about 50 nm around the cavity wavelength, while panel (b) shows the quantity $G = \frac{\max(I(\lambda))}{\int I(\lambda)d\lambda}$, where $I(\lambda)$ is the emission spectrum. This quantity, G, serves as an empirical quantification of how suitable the dots are for the experiment presented here. It should be noted that dots with linewidths comparable to, or smaller than the setup resolution are a very small fraction of the optically detected dots and usually they are not the brightest ones. The dot studied in this chapter is visible as a red spot at the bottom of Fig.11.2(b). In the same

figure a regular pattern of low signal regions is visible: this are metal markers used as references to easily position on a given quantum dot.

We determined the lifetime of optical transitions by time resolved PL measurements. Emission from the transition of interest was sent to an avalanche photodiode (APD) via a monochromator. The dots were excited by a pulsed (picosecond) Ti:Sapph laser and the time of detection events was measured by an amplitude to time converter. The laser wavelength was 816 nm, creating electron hole pairs in the wetting layer. We calculated the lifetime by fitting the data taking into account the finite response time of our APDs. In particular we fitted the measurement with an exponential decay convoluted with the APD response to a picosecond pulse (Fig.11.3).
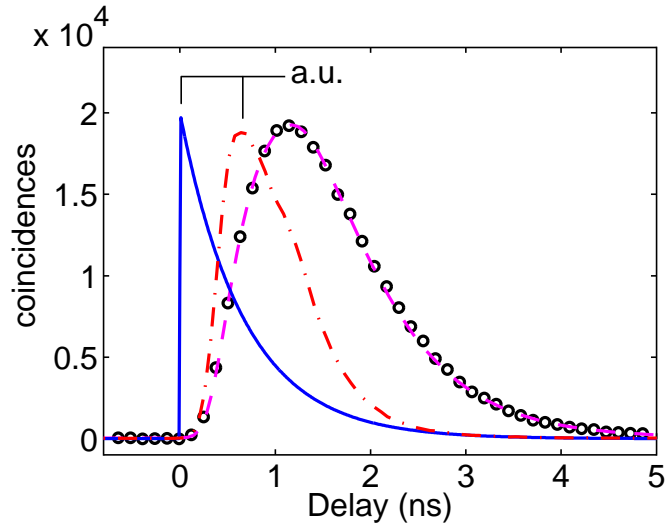
Figure 11.3: Lifetime measurement. Measured decay signal by means of an avalanche photodiode (circles). The measurement was fitted (dashed line) with an exponential decay (solid line) convoluted with the measurement setup response (dot-dash line) to a picosecond laser pulse. We estimated a lifetime $\tau = 670$ ps and a background signal of 500 cts.

In order to determine the purity of our single photon source we performed an intensity autocorrelation measurement under pulsed excitation in an excited state of the quantum dot. We excited the dot with 895 nm laser light which is about 30 nm shorter in wavelength than the observed PL line. It is clear from Fig.11.4(a) that this QD is an extremely pure source of single photons as no peak can be seen at zero delay within the experimental error. The measurement was taken over about 17 hours of integration time with count rates at the two detectors of 4000 and 8800 counts. Based on a laser repetition rate of 12.6 ns,

this corresponds to a combined excitation and detection efficiency of 0.00016 for the two detectors combined. For such a small collection efficiency the normalized areas of the peaks in Fig.11.4(a) are the values of the discrete $g^{(2)}$ function. These areas, calculated from the data after background subtraction, are plotted in Fig.11.4(b). We subtracted a constant background of 107 counts (*under*estimated as the average signal in $(-8, -4) \cup (4, 8)$ ns minus twice its standard deviation). From this we get $g^{(2)}[0] = 0.024$. This means that the probability of detecting two or more photons in the same pulse $P(n \geqslant 2) = \frac{1}{2}\bar{n}^2 g^{(2)}[0]$ is 40 times smaller than for a Poissonian source, for which $P(n \geqslant 2) = \frac{1}{2}\bar{n}^2$. Without subtracting a background from the data we get $g^{(2)}[0] = 0.14$, which corresponds to a correlation suppression factor of about 7.

More than $g^{(2)}[0]$, what is relevant to the present experiment [100] is the quantity g given by the ratio $g = g^{(2)}[0]/g^{(2)}[1]$. This represents for two subsequent pulses, the probability that either of the two contains two photons divided by the probability that both contain one photon and determine the contrast of the two-photon interference measurement. In our case $g = 0.017$, after subtracting the background counts.

In the autocorrelation measurement the peaks close to zero delay are bigger than the ones at longer delays. This means that if the quantum dot emits a photon after a given laser pulse, the probability of emitting another one of the same color is higher for the next few pulses than for an average pulse. This can be interpreted as blinking of the quantum dot: the relevant optical transition going on and off randomly with characteristic time scales τ_{on} and τ_{off}. One explanation for this behavior is based on the fact that the dot can be in different charged states and we excite it resonantly only when it is in a particular state. This explanation is supported by the fact that we do see different charged state transitions when the dot is excited via the wetting layer. Another reason for the blinking could be the fact that an excited electron hole pair might end up in a dark exciton state due to spin flips. The blinking might also be caused by the dot preferentially emitting photons with the same polarization within a short time scale. Since we detect only one polarization we would be sometimes blind to the emitted light and the dot would seem dark.

11.4 Setup

The central element of the measurement setup is the beam splitter at which two-photon interference occurs. We chose a fiber based beam splitter (Fig.11.5) in order to avoid any mismatch between the spatial modes of the incoming photons.
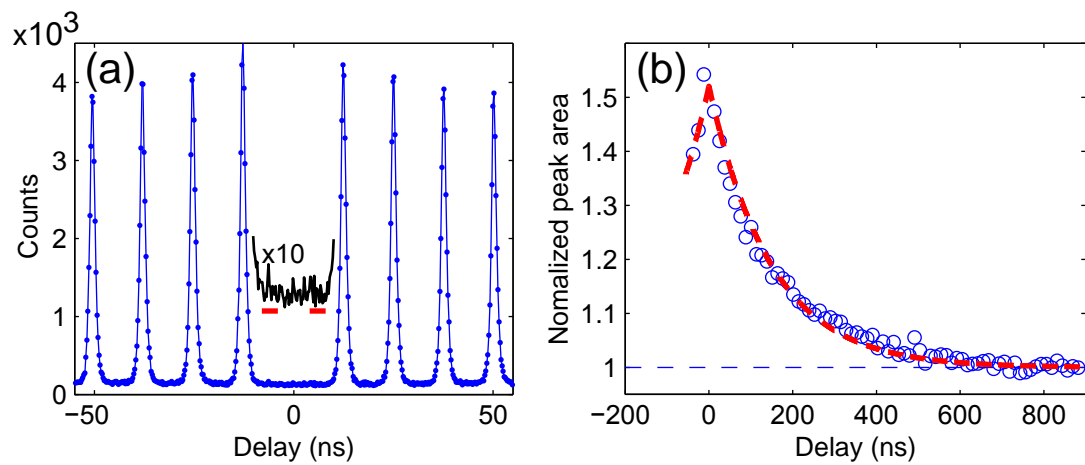
Figure 11.4: Antibunching. (a) Photon correlation measurement under excitation of the quantum dot in a high energy shell. Counts around zero delay a showed rescaled by a factor 10. Two short horizontal lines indicate the background level and the intervals in which it was estimated.

The reflectivity of this beam splitter is 0.55 ± 0.5 and was measured by using a laser at the same wavelength as the quantum dot transition studied here. The fact that the beam splitter is not perfectly $50 : 50$ slightly reduces the interference visibility as we will see later in this chapter.

We produce pairs of photons by periodically exciting a quantum dot with pairs of laser pulses separated by a time interval dt. In order to let the photons emitted after two adjacent laser pulses arrive simultaneously at the beam splitter we let them travel different distances. This is done by means of a fiber based Michelson interferometer with a time difference δt equal to the pulse separation dt. In this way if the photon which is emitted first goes the long arm and the other the short arm they will meet at the same time at the beam splitter. We tuned dt to be equal to the fixed delay δt within some pico seconds by looking at the interferometer outputs with a streak camera (Hamamatsu).
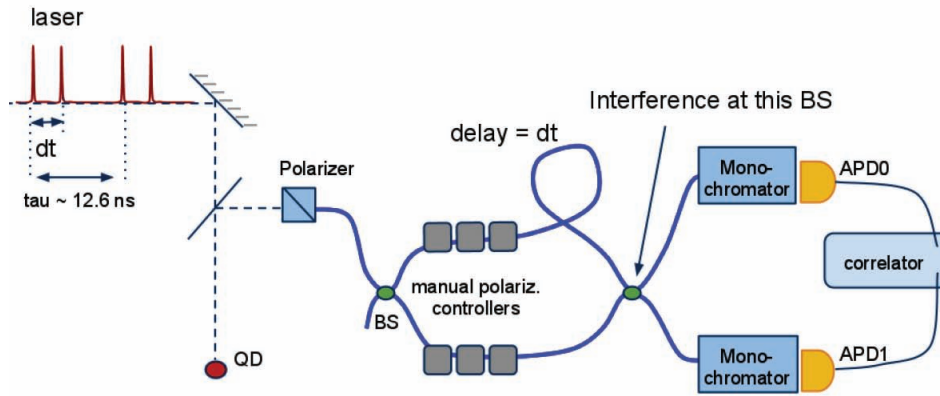
Figure 11.5: Two photon interference setup. Every $\tau = 12.6$ ns a pair of picosecond laser pulses separated by a delay dt is focussed on a quantum dot in order to excite it. After each pulse, with a small probability, a single photon is emitted by the dot and injected in a Michelson interferometer. The fiber based Michelson allows to interfere pairs of photons with a time separation of $\delta t = 5.7$ ns, corresponding to the path difference between its arms. In the experiment dt was tuned to match δt. The photons are detected with avalanche photodiodes and a correlator measures the difference between detection times. Monochromators were used to select the transition of interest.

We used the polarization degree of freedom in order to make photons going in different arms of the Michelson either distinguishable or indistinguishable. To this end we first selected a given polarization $|V\rangle$ at the input of the interferometer. This polarization state was then modified independently in the two arms by

straining and twisting the fiber with manual polarization controllers. We made sure that the polarization states at the beam splitter were parallel or orthogonal by measuring their polarization state at one of the Michelson outputs. In particular we used a polarizer in front of one of the two detectors and we tuned the polarization controllers to minimize the transmitted signal. The polarizer was then removed for the interference measurement. It should be noted that in this setup all the optical fiber in the detection paths (except the one after the second beam splitter) need to be kept fixed during the measurements in order to maintain orthogonal or parallel polarization states at the beam splitter. Laser light and unwanted light from the quantum dot were filtered out by using a 920 nm long pass filter and two monochromators in front of the detectors. One of the monochromators is a 1 m Jobin-Yvon spectrometer with a tunable slit and a free space APD at one of the output ports. This system allows to select a narrow energy range of a few tens of μeV. The other is a tunable filter by Photonetc and has a transmission band of about 300μeV). We used a multimode fiber to couple the output of this monochromator to the other APD.

In our experiment we register detection events in which both detectors clicked within a given time interval. We build a histogram of the number of detection events as a function of the time difference between the two clicks. Due to the geometry of the setup most of the detection events are around different time delays τ.

If two photons one emitted at time t_0 (early photon) and the other emitted at time $t_0 + dt$ (late photon) follow different arms of the interferometer they can either be detected at the same time, $\Delta t = 0$ or with time delays of $\Delta t = \pm 2dt$ depending on whether the early photon went the long arm and the late photon the short arm or vice versa. The detection events corresponding to the two photons taking the same arm of the interferometer are around $\Delta t = \pm dt$. Detection events at longer delays Δt correspond to the detection of photons produced in different repetitions of the laser pulses. A schematics of the expected measurements for different delays is shown in Fig.11.6(a,b) for different values of dt. In our case the delay between a pair of laser pulses is longer, $dt = 5.7ns$, and this causes the different peaks of the histogram to be reshuffled in time in a less intuitive way. We used the same color for corresponding peaks in the two sketches in order to facilitate their identification.

The shape of these correlation peaks is intrinsically determined by the lifetime of the studied transition and, in the actual measurements, it is modified by the time jitter introduced by the detection equipment. This jitter is, in our case, much longer than the lifetime. To include both lifetime and the APD response time (11.6(a,b)) we convoluted the idealized correlation histograms of Fig.11.6(a,b)
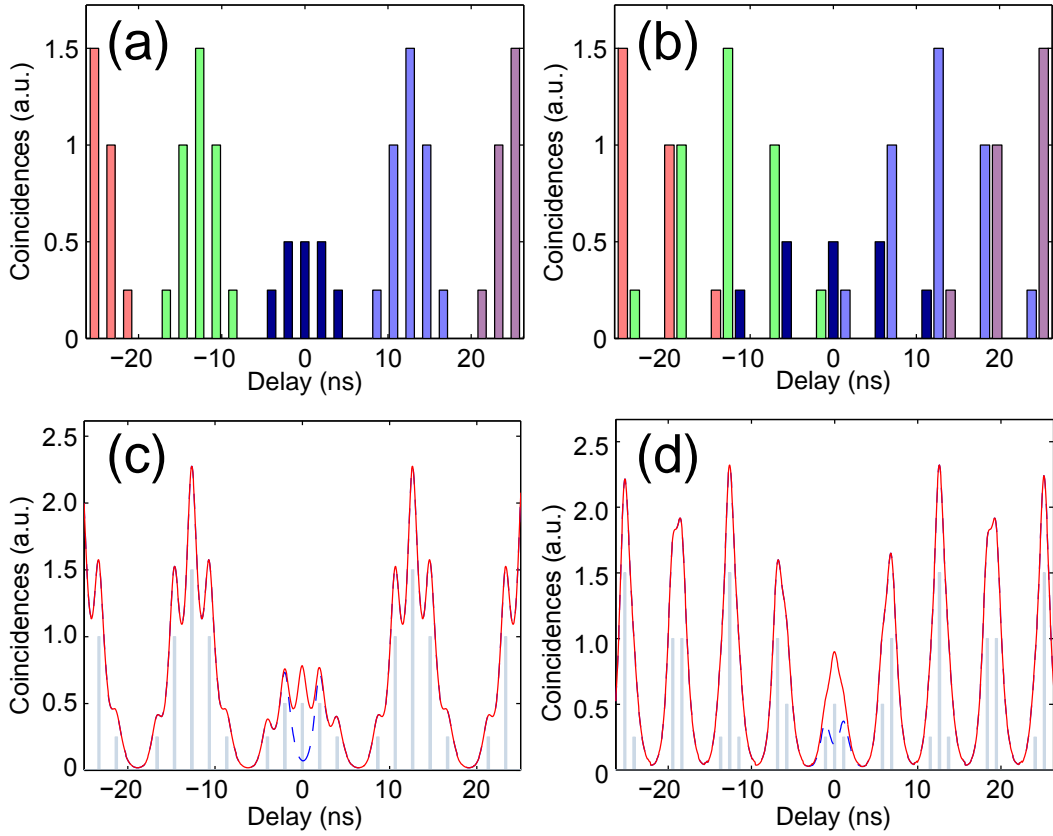
Figure 11.6: **(a)** Expected peak positions and (relative) areas for a photon interference measurement. The peak at zero delay is absent for perfect two-photon interference. We assumed the laser and Michelson delays to be $dt = \delta t = 2$ ns. **(b)** Same as in the previous figure but with delays $dt = \delta t = 5.7$ ns, as in the measurements presented in this chapter. Corresponding peaks have the same color in panels (a) and (b). **(c,d)** Expected measurement considering the spread in time of the photon wave-packets and the time jitter introduced by the detectors. Solid (red) line: no interference; dashed (blue) line: perfect interference.

with an average autocorrelation peak from the measurement of Fig.11.4(a).

11.5 Two-photon interference measurements

We injected electron-hole pairs in the quantum dot by laser excitation at two different wavelengths. First we excited the quantum dot non resonantly, using laser pulses with a wavelength of 816 nm. In this way carriers are created in the wetting layer and in the GaAs layers and subsequently relax to the quantum dot. Under this excitation conditions the count rates were 9.0 ± 0.5 kHz for the free space APD and 25 ± 5 for the fiber coupled APD. The resulting interference measurements for parallel and for orthogonal polarizations is shown in Fig.11.7(a). The two measurements were taken over about 3.5 hours each. The second measurement was rescaled by a factor of 0.98 in order to directly compared it to the first. The scaling factor was determined such as to ensure that the integral of the two measurements at times far from zero delay (delay between ~ 20 and ~ 280 ns) are the same. A clear difference is visible between the two measurements for the peak at zero delay. We quantify the interference by the average overlap integral V defined earlier. If we assume a perfect setup, this quantity is directly related to the area of the peak at zero delay, in particular $(1-V)$ can be measured as the ratio between the area of the zero delay peak and the area of the peak at δt delay (or as the ratio between the area of the zero delay peak and the area of the same peak but for completely distinguishable photons). Measuring V in this way actually gives an underestimate of it because spurious effect like deviations from a 50:50 splitting ratio, imperfect single photon sources and geometrical imperfections of the optical system all contribute to reduce this quantity. We will discuss the influence of this effects later in this section.

Since in our experiment we are not able to resolve all the different peaks and we need to resort to fitting in order to estimate the area of the central peak relative to the area of the surrounding peaks. Calculated curves corresponding different degrees of interference are superimposed to the measurements. We used a constant background and the overall intensity of the simulated correlations as fitting parameters. It can be seen that the curves for no interference ($V = 0$) and partial interference ($V = 50$) are reasonably good fits to the orthogonal and parallel polarization measurements respectively.

In order to get better two-photon interference we excited the quantum dot resonantly in a high energy shell, at about 30 nm shorter wavelength than the studied s-shell transition. To do this we scanned the wavelength of our laser, while in continuous wave mode, from high energy down to the energies of quantum dot
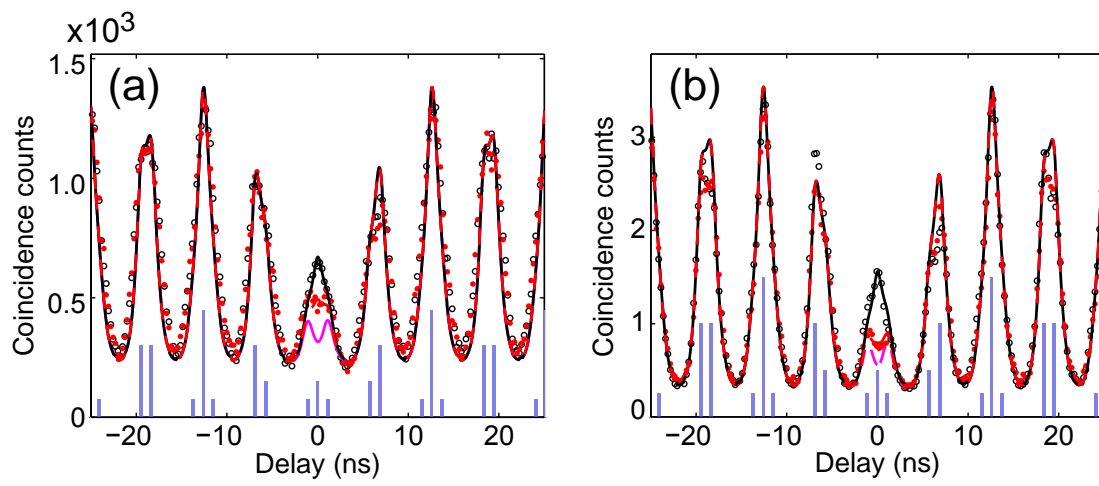
Figure 11.7: **(a) Two photon interference under non resonant excitation.** Caption goes here. **(b) Two photon interference under excitation in the dot.**

transitions. We could not study resonances closer to the s-shell than the one studied because we could not filter out the laser light from the measurement setup at too long wavelengths.

We took 10 hour measurements for orthogonal polarizations (HV, horizontal and vertical) and for parallel polarizations (VV, both vertical). The data of this latter case were were rescaled by a factor 1.9 according to the same criterion as in the previous measurement.

The fitting [Fig.11.7(b)] reveals an average two photon overlap of 0.76, much bigger than for the case of non resonant excitation. This is probably due to the fact that the excitation is limited to the dot and that there is less charge noise that can cause dephasing of the optical transition.

In order to consider some of the imperfections of our system we can write for the areas of the zero and δt delay peaks:

$$A_{\delta t} = A \left\{ p\frac{A_{\delta t}}{A} + (1-p)[(R^2 + T^2)(1+2g) - 2RTV] \right\} \tag{11.5}$$

$$A_0 = A \left[R^2(1+2g) + T^2 \right], \tag{11.6}$$

where p is the probability for the two photons to have orthogonal probabilities, R,T are the reflection and transmission coefficient of the beam splitter and g quantifies the quality of our single photon source as described in section 11.3. A is a normalization constant. From these equations we can write the overlap integral V as:

$$V = \frac{1}{2} \left(\frac{R}{T} + \frac{T}{R} \right)(1+2g) - \frac{\nu - p}{2(1-p)} \left[\frac{R}{T}(1+2g) + \frac{T}{R} \right] \tag{11.7}$$

Table 11.1: Photon state fidelity

	H,V meas.		V,V meas.	
	before	after	before	after
$\|\langle s\|H\rangle\|^2$	0.976	0.978	0.012	< 0.020
$\|\langle s\|V\rangle\|^2$	0.024	0.022	0.988	> 0.980
$\|\langle l\|H\rangle\|^2$	0.010	0.014	0.014	< 0.023
$\|\langle l\|V\rangle\|^2$	0.990	0.986	98.6	> 0.977

Taking the first non-zero terms of its Taylor expansion around $g = p = 0$, $x = R - 1/2 = 0$ and the measured ν we can estimate the error in V to be: $\Delta V = (2-\nu)g + (1-\nu)(4x^2 + \Delta p)$.

The contribution due to imperfect polarization preparation can be estimated from table 11.1.

Bibliography

[1] B. Streetman and S. Banerjee, *Solid State Electronic Devices.* Pearson Education, 6 ed., 2009. 13

[2] P. Weisbuch and B. Vinter, *Quantum Semiconductor Structures.* Academic Press, 1991. 13, 25

[3] P. Michler, ed., *Single Quantum Dots.* Springer, 2003. 13, 18

[4] K. K. Likharev, "Single-electron devices and their applications," *Proceedings of the IEEE*, vol. 87, pp. 606–632, April 1999. 13

[5] F. H. L. Koppens, C. Buizert, K. J. Tielrooij, I. T. Vink, K. C. Nowack, T. Meunier, L. P. Kouwenhoven, and L. M. K. Vandersypen, "Driven coherent oscillations of a single electron spin in a quantum dot," *Nature*, vol. 442, pp. 766–771, 2006. 13, 56

[6] J. R. Petta, A. C. Johnson, J. M. Taylor, E. A. Laird, A. Yacoby, M. D. Lukin, C. M. Marcus, M. P. Hanson, and A. C. Gossard, "Coherent Manipulation of Coupled Electron Spins in Semiconductor Quantum Dots," *Science*, vol. 309, pp. 2180–2184, 2005. 13

[7] A. Aspect, J. Dalibard, and G. Roger, "Experimental Test of Bell's Inequalities Using Time-Varying Analyzers," *Physical Review Letters*, vol. 49, pp. 1804–1807, Dec 1982. 13

[8] D. L. Moehring, P. Maunz, S. Olmschenk, K. C. Younge, D. N. Matsukevich, L. M. Duan, and C. Monroe, "Entanglement of single-atom quantum bits at a distance," *Nature*, vol. 449, no. 7158, pp. 68–71. 13, 72, 73, 76, 82

[9] P. Michler, A. Imamoglu, M. D. Mason, P. J. Carson, G. F. Strouse, and S. K. Buratto, "Quantum correlation among photons from a single quantum dot at room temperature," *Nature*, vol. 406, pp. 968–970, August 2000. 13, 80

[10] N. Akopian, N. H. Lindner, E. Poem, Y. Berlatzky, J. Avron, D. Gershoni, B. D. Gerardot, and P. M. Petroff, "Entangled photon pairs from semiconductor quantum dots," *Physical Review Letters*, vol. 96, no. 13, 2006. 13, 80

[11] C. Santori, D. Fattal, J. Vuckovic, G. S. Solomon, and Y. Yamamoto, "Indistinguishable photons from a single-photon device," *Nature*, vol. 419, pp. 594–597, October 2002. 13

[12] R. P. Feynman, "Simulating physics with computers," *International Journal of Theoretical Physics*, vol. 21, pp. 467–488, 1982. 13

[13] M. A. Nielsen and I. L. Chuang, *Quantum computation and quantum information.* Cambridge Univ. Press, Cambridge, 2000. 13

[14] G. Bennett C. H., Brassard, "Quantum Cryptography: Public key distribution and coin tossing," *Proceedings of the IEEE International Conference on Computers, Systems, and Signal Processing, Bangalore*, p. 175, 1984. 14

[15] E. Knill, R. Laflamme, and G. J. Milburn, "A scheme for efficient quantum computation with linear optics," *Nature*, vol. 409, pp. 46–52, January 2001. 14, 72, 104

[16] J. E. Avron, G. Bisker, D. Gershoni, N. H. Lindner, E. A. Meirom, and R. J. Warburton, "Entanglement on Demand through Time Reordering," *Physical Review Letters*, vol. 100, no. 12, 2008. 15

[17] W. Sheng and P. Hawrylak, "Atomistic theory of electronic and optical properties of InAs/InP self-assembled quantum dots on patterned substrates," *Phys. Rev. B*, vol. 72, p. 035326, 2005. 18

[18] M. Ediger, G. Bester, A. Badolato, P. M. Petroff, K. Karrai, A. Zunger, and R. J. Warburton, "Peculiar many-body effects revealed in the spectroscopy of highly charged quantum dots," *Nat. Phys.*, vol. 3, pp. 774–779, 2007. 18

[19] R. Singh and G. Bester, "Nanowire quantum dots as an ideal source of entangled photon pairs," *Phys. Rev. Lett.*, vol. 103, p. 063601, 2009. 18, 28

[20] A. Hartmann, Y. Ducommun, E. Kapon, U. Hohenester, and E. Molinari, "Few-particle effects in semiconductor quantum dots: Observation of multicharged excitons," *Phys. Rev. Lett.*, vol. 84, pp. 5648–5651, 2000. 18

[21] M. A. Verheijen, G. Immink, T. de Smet, M. T. Borgström, and E. P. A. M. Bakkers, "Growth kinetics of heterostructured GaP-GaAs nanowires," *J. Am. Chem. Soc.*, vol. 128, pp. 1353–1359, 2006. 18, 56, 57

[22] M. Gong, K. Duan, C.-F. Li, R. Magri, G. A. Narvaez, and L. He, "Electronic structure of self-assembled InAs/InP quantum dots: Comparison with self-assembled InAs/GaAs quantum dots," *Phys. Rev. B*, vol. 77, p. 045326, 2008. 19, 25

[23] D. J. Griffiths, *Introduction to quantum mechanics.* Prentice Hall, 1995. 19

[24] P. Hawrylak, "Excitonic artificial atoms: Engineering optical properties of quantum dots," *Phys. Rev. B*, vol. 60, pp. 5597–5608, 1999. 21, 26

[25] V. Fock, "Bemerkung zur Quantelung des harmonischen Oszillators im Magnetfeld," *Zeitschrift für Physik A Hadrons and Nuclei*, vol. 47, pp. 446–448, May 1928. 21

[26] C. G. Darwin, "The Diamagnetism of the Free Electron," *Mathematical Proceedings of the Cambridge Philosophical Society*, vol. 27, no. 01, pp. 86–90, 1931. 21

[27] L. Jacak and P. Hawrylak, *Quantum Dots.* Springer, 1998. 23

[28] M. Bayer, V. B. Timofeev, T. Gutbrod, A. Forchel, R. Steffen, and J. Oshinowo, "Enhancement of spin splitting due to spatial confinement in $In_xGa_{1-x}As$ quantum dots," *Phys. Rev. B*, vol. 52, pp. R11623–R11625, 1995. 25

[29] B. D. Gerardot, D. Brunner, P. A. Dalgarno, P. Öhberg, S. Seidl, M. Kroner, K. Karrai, N. G. Stoltz, P. M. Petroff, and R. J. Warburton, "Optical pumping of a single hole spin in a quantum dot," *Nature*, vol. 451, pp. 441–444, 2008. 25

[30] M. Bayer, G. Ortner, O. Stern, A. Kuther, A. A. Gorbunov, A. Forchel, P. Hawrylak, S. Fafard, K. Hinzer, T. L. Reinecke, S. N. Walck, J. P. Reithmaier, F. Klopf, and F. Schäfer, "Fine structure of neutral and charged excitons in self-assembled InGaAs/(Al)GaAs quantum dots," *Phys. Rev. B*, vol. 65, p. 195315, 2002. 27, 29, 67

[31] R. M. Stevenson, R. J. Young, P. See, C. E. Norman, A. J. Shield, P. Atkinson, and D. A. Ritchie, "Strong directional dependence of single-quantum-dot fine structure," *Appl. Phys. Lett.*, vol. 87, p. 133120, 2005. 28

[32] O. Benson, C. Santori, M. Pelton, and Y. Yamamoto, "Regulated and entangled photons from a single quantum dot," *Phys. Rev. Lett.*, vol. 84, pp. 2513–2516, 2000. 28

[33] S. N. Walck and T. L. Reinecke, "Exciton diamagnetic shift in semiconductor nanostructures," *Phys. Rev. B*, vol. 57, pp. 9088–9096, 1998. 32, 58

[34] J. Altepeter, D. James, and P. Kwiat, "4 qubit quantum state tomography," in *Quantum State Estimation*, pp. 27–45, 2004. 38, 83

[35] Y. Li, F. Qian, J. Xiang, and C. M. Lieber *Materials Today*, vol. 9, p. 19, 2006. 44

[36] R. S. Wagner and W. C. Ellis, "Vapor-liquid-solid mechanism of single crystal growth," *Appl. Phys. Lett.*, vol. 4, pp. 89–90, 1964. 44

[37] M. S. Gudiksen, L. J. Lauhon, J. Wang, D. C. Smith, and C. M. Lieber, "Growth of nanowire superlattice structures for nanoscale photonics and electronics," *Nature*, vol. 415, pp. 617–620, February 2002. 44

[38] L. J. Lauhon, M. S. Gudiksen, D. Wang, and C. M. Lieber, "Epitaxial core-shell and core-multishell nanowire heterostructures," *Nature*, vol. 420, pp. 57–61, November 2002. 44

[39] E. Lind, A. I. Persson, L. Samuelson, and L.-E. Wernersson, "Improved sub-threshold slope in an inas nanowire heterostructure field-effect transistor," *Nano Letters*, vol. 6, pp. 1842–1846, September 2006. 44

[40] M. T. Björk, B. J. Ohlsson, T. Sass, A. I. Persson, C. Thelander, M. H. Magnusson, K. Deppert, L. R. Wallenberg, and L. Samuelson, "One-dimensional heterostructures in semiconductor nanowhiskers," *Applied Physics Letters*, vol. 80, no. 6, pp. 1058–1060, 2002. 44

[41] X. Duan, Y. Huang, Y. Cui, J. Wang, and C. M. Lieber, "Indium phosphide nanowires as building blocks for nanoscale electronic and optoelectronic devices," *Nature*, vol. 409, pp. 66–69, January 2001. 44, 56

[42] H. Pettersson, J. Trägårdh, A. I. Persson, L. Landin, D. Hessman, and L. Samuelson, "Infrared photodetectors in heterostructure nanowires," *Nano Letters*, vol. 6, pp. 229–232, February 2006. 44

[43] E. D. Minot, F. Kelkensberg, M. van Kouwen, J. A. van Dam, L. P. Kouwen-hoven, V. Zwiller, M. T. Borgström, O. Wunnicke, M. A. Verheijen, and E. P. A. M. Bakkers, "Single quantum dot nanowire leds," *Nano Letters*, vol. 7, pp. 367–371, February 2007. 44

[44] V. G. Dubrovskii, G. E. Cirlin, I. P. Soshnikov, A. A. Tonkikh, N. V. Sibirev, Yu, and V. M. Ustinov, "Diffusion-induced growth of gaas nanowhiskers during molecular beam epitaxy: Theory and experiment," *Physical Review B*, vol. 71, p. 205325, May 2005. 45

[45] C. Chen, M. C. Plante, C. Fradin, and R. R. LaPierre *J. Mater. Res.*, vol. 21, p. 2801, 2006. 46

[46] M. Tchernycheva, J. C. Harmand, G. Patriarche, L. Travers, and G. E. Cirlin, "Temperature conditions for gaas nanowire formation by au-assisted molecular beam epitaxy," *Nanotechnology*, vol. 17, pp. 4025–4030, August 2006. 47

[47] F. Glas, "Critical dimensions for the plastic relaxation of strained axial heterostructures in free-standing nanowires," *Physical Review B*, vol. 74, p. 121302, Sep 2006. 48

[48] M. T. Borgström, V. Zwiller, E. Muller, and A. Imamoglu, "Optically bright quantum dots in single nanowires," *Nano Lett.*, vol. 5, pp. 1439–1443, 2005. 49, 56

[49] Y. M. Niquet, "Electronic and optical properties of inas gaas nanowire superlattices," *Physical Review B*, vol. 74, p. 155304, Oct 2006. 51

[50] I. Vurgaftman, J. R. Meyer, and L. R. R. Mohan, "Band parameters for iii–v compound semiconductors and their alloys," *Journal of Applied Physics*, vol. 89, no. 11, pp. 5815–5875, 2001. 51

[51] A. I. Persson, M. T. Björk, S. Jeppesen, J. B. Wagner, L. R. Wallenberg, and L. Samuelson, "Inas1-xpx nanowires for device engineering," *Nano Letters*, vol. 6, pp. 403–407, March 2006. 51

[52] M. H. Huang, S. Mao, H. Feick, H. Yan, Y. Wu, H. Kind, E. Weber, R. Russo, and P. Yang, "Room-temperature ultraviolet nanowire nanolasers," *Science*, vol. 292, pp. 1897–1899, 2001. 56

[53] X. Duan, Y. Huang, Y. Cui, J. Wang, and C. M. Lieber, "Indium phosphide nanowires as building blocks for nanoscale electronic and optoelectronic devices," *Nature*, vol. 409, pp. 66–69, 2001. 56

[54] X. Duan, Y. Huang, R. Agarwal, and C. M. Lieber, "Single-nanowire electrically driven lasers," *Nature*, vol. 421, pp. 241–245, 2003. 56

[55] H. Pettersson, J. Trägårdh, A. I. Persson, L. Landin, D. Hessman, and L. Samuelson, "Infrared photodetectors in heterostructure nanowires.," *Nano Lett.*, vol. 6, pp. 229–232, 2006. 56

[56] E. D. Minot, F. Kelkensberg, M. van Kouwen, J. A. van Dam, L. P. Kouwenhoven, V. Zwiller, M. T. Borgström, O. Wunnicke, M. A. Verheijen, and E. P. A. M. Bakkers, "Single quantum dot nanowire LEDs," *Nano Lett.*, vol. 7, pp. 367–371, 2007. 56, 64

[57] J. Renard, R. Songmuang, C. Bougerol, B. Daudin, and B. Gayral, "Exciton and biexciton luminescence from single GaN/AlN quantum dots in nanowires," *Nano Lett.*, vol. 8, pp. 2092–2096, 2008. 56

[58] M. T. Björk, C. Thelander, A. E. Hansen, L. E. Jensen, M. W. Larsson, L. R. Wallenberg, and L. Samuelson, "Few-electron quantum dots in nanowires," *Nano Lett.*, vol. 4, pp. 1621–1625, 2004. 56, 58

[59] P. Michler, A. Kiraz, C. Becher, W. V. Schoenfeld, P. M. Petroff, L. Zhang, E. Hu, and A. Imamoglu, "A quantum dot single-photon turnstile device," *Science*, vol. 290, pp. 2282–2285, 2000. 56

[60] C. Santori, M. Pelton, G. Solomon, Y. Dale, and Y. Yamamoto, "Triggered single photons from a quantum dot," *Phys. Rev. Lett.*, vol. 86, pp. 1502–1505, 2001. 56

[61] J. R. Petta, A. C. Johnson, J. M. Taylor, E. A. Laird, A. Yacoby, M. D. Lukin, C. M. Marcus, M. P. Hanson, and A. C. Gossard, "Coherent manipulation of coupled electron spins in semiconductor quantum dots," *Science*, vol. 309, pp. 2180–2184, 2005. 56

[62] J. Wang, M. S. Gudiksen, X. Duan, Y. Cui, and C. M. Lieber, "Highly polarized photoluminescence and photodetection from single indium phosphide nanowires," *Science*, vol. 293, pp. 1455–1457, 2001. 56

[63] O. L. Muskens, J. Treffers, M. Forcales, M. T. Borgström, E. P. A. M. Bakkers, and G. J. Rivas, "Modification of the photoluminescence anisotropy of semiconductor nanowires by coupling to surface plasmon polaritons," *Opt. Lett.*, vol. 32, pp. 2097–2099, 2007. 56

[64] M. H. M. van Weert, N. Akopian, F. Kelkensberg, U. Perinetti, M. P. van Kouwen, J. Gómez Rivas, M. T. Borgström, R. E. Algra, M. A. Verheijen, E. P. A. M. Bakkers, L. P. Kouwenhoven, and V. Zwiller, "Orientation-dependent optical-polarization properties of single quantum dots in nanowires," *Small*, vol. 5, pp. 2134–2138, 2009. 56

[65] M. Bayer, O. Stern, P. Hawrylak, S. Fafard, and A. Forchel, "Hidden symmetries in the energy levels of excitonic /'artificial atoms/'," *Nature*, vol. 405, pp. 923–926, 2000. 56

[66] C. Fasth, A. Fuhrer, M. T. Björk, and L. Samuelson, "Tunable double quantum dots in InAs nanowires defined by local gate electrodes," *Nano Lett.*, vol. 5, pp. 1487–1490, 2005. 56

[67] H. T. Ng, J. Han, T. Yamada, P. Nguyen, Y. P. Chen, and M. Meyyappan, "Single crystal nanowire vertical surround-gate field-effect transistor," *Nano Lett.*, vol. 4, pp. 1247–1252, 2004. 56

[68] T. Bryllert, L.-E. Wernersson, T. Lowgren, and L. Samuelson, "Vertical wrap-gated nanowire transistors," *Nanotechnol.*, vol. 17, pp. S227–S230, 2006. 56

[69] V. Schmidt, H. Riel, S. Senz, S. Karg, W. Riess, and U. Gösele, "Realization of a silicon nanowire vertical surround-gate field-effect transistor," *Small*, vol. 2, pp. 85–88, 2006. 56

[70] K. Hiruma, T. Katsuyama, K. Ogawa, M. Koguchi, H. Kakibayashi, and G. P. Morgan, "Quantum size microcrystals grown using organometallic vapor phase epitaxy," *Appl. Phys. Lett.*, vol. 59, pp. 431–433, 1991. 57

[71] L. J. Lauhon, M. S. Gudiksen, D. Wang, and C. M. Lieber, "Epitaxial core-shell and core-multishell nanowire heterostructures," *Nature*, vol. 420, pp. 57–61, 2002. 57

[72] M. Kroutvar, Y. Ducommun, D. Heiss, M. Bichler, D. Schuh, G. Abstreiter, and J. J. Finley, "Optically programmable electron spin memory using semiconductor quantum dots.," *Nature*, vol. 432, pp. 81–84, 2004. 60

[73] A. Greilich, A. Shabaev, D. R. Yakovlev, A. Efros, I. A. Yugova, D. Reuter, A. D. Wieck, and M. Bayer, "Nuclei-induced frequency focusing of electron spin coherence," *Science*, vol. 317, pp. 1896–1899, 2007. 62

[74] M. Sénès, B. Urbaszek, X. Marie, T. Amand, J. Tribollet, F. Bernardot, C. Testelin, M. Chamarro, and J. M. Gérard, "Exciton spin manipulation in InAs/GaAs quantum dots: Exchange interaction and magnetic field effects," *Phys. Rev. B*, vol. 71, p. 115334, 2005. 62

[75] M. Paillard, X. Marie, P. Renucci, T. Amand, A. Jbeli, and J. M. Gérard, "Spin relaxation quenching in semiconductor quantum dots," *Phys.Rev.Lett.*, vol. 86, pp. 1634–1637, 2001. 62

[76] M. Tchernycheva, G. E. Cirlin, G. Patriarche, L. Travers, V. Zwiller, U. Perinetti, and J. C. Harmand, "Growth and characterization of InP nanowires with inasp insertions," *Nano Lett.*, vol. 7, pp. 1500–1504, 2007. 64

[77] C. E. Pryor and M. E. Flatté, "Landé g Factors and Orbital Momentum Quenching in Semiconductor Quantum Dots," *Physical Review Letters*, vol. 96, p. 026804, January 2006. 66

[78] M. T. Björk, A. Fuhrer, A. E. Hansen, M. W. Larsson, L. E. Fröberg, and L. Samuelson, "Tunable effective g factor in InAs nanowire quantum dots," *Physical Review B*, vol. 72, p. 201307, Nov 2005. 66

[79] A. De and C. E. Pryor, "Calculation of Landé g factors for III-V nanowhisker quantum dots and comparison with experiment," *Physical Review B*, vol. 76, p. 155321, Oct 2007. 66

[80] S. Strauf, N. G. Stoltz, M. T. Rakher, L. A. Coldren, P. M. Petroff, and D. Bouwmeester, "High-frequency single-photon source with polarization control," *Nature Photonics*, vol. 1, pp. 704–708, November 2007. 72

[81] B. Lounis and M. Orrit, "Single-photon sources," *Rep. Prog. Phys.*, vol. 68, pp. 1129–1179, May 2005. 72

[82] R. B. Patel, A. J. Bennett, I. Farrer, C. A. Nicoll, D. A. Ritchie, and A. J. Shields, "Tunable indistinguishable photons from remote quantum dots," Nov 2009. 72

[83] R. Hanson, L. P. Kouwenhoven, J. R. Petta, S. Tarucha, and L. M. K. Vandersypen, "Spins in few-electron quantum dots," *Rev. Mod. Phys.*, vol. 79, no. 4, p. 1217, 2007. 72

[84] P. Maunz, D. L. Moehring, S. Olmschenk, K. C. Younge, D. N. Matsukevich, and C. Monroe, "Quantum interference of photon pairs from two

remote trapped atomic ions," *Nat. Phys.*, vol. 3, pp. 538–541, June 2008. 72, 104

[85] K. Sanaka, A. Pawlis, T. D. Ladd, K. Lischka, and Y. Yamamoto, "Indistinguishable photons from independent semiconductor nanostructures," *Phys. Rev. Lett.*, vol. 103, no. 5, p. 053601, 2009. 72, 104

[86] J. Brendel, N. Gisin, W. Tittel, and H. Zbinden, "Pulsed energy-time entangled twin-photon source for quantum communication," *Phys. Rev. Lett.*, vol. 82, pp. 2594–2597, Mar 1999. 72

[87] L. A. Liew, S. Knappe, J. Moreland, H. Robinson, L. Hollberg, and J. Kitching, "Microfabricated alkali atom vapor cells," *Appl. Phys. Lett.*, vol. 84, no. 14, pp. 2694–2696, 2004. 72

[88] L. Wang, V. Křápek, F. Ding, F. Horton, A. Schliwa, D. Bimberg, A. Rastelli, and O. G. Schmidt, "Self-assembled quantum dots with tunable thickness of the wetting layer: Role of vertical confinement on interlevel spacing," *Phys. Rev. B*, vol. 80, no. 8, p. 085309, 2009. 72, 73

[89] A. Rastelli, S. Stufler, A. Schliwa, R. Songmuang, C. Manzano, G. Costantini, K. Kern, A. Zrenner, D. Bimberg, and O. G. Schmidt, "Hierarchical self-assembly of gaas/algaas quantum dots," *Phys. Rev. Lett.*, vol. 92, p. 166104, Apr 2004. 72

[90] M. Benyoucef, L. Wang, A. Rastelli, and O. G. Schmidt, "Towards quantum interference of photon pairs emitted from two independent quantum dots," *in preparation*, 2009. 78

[91] T. H. Stievater, X. Li, D. G. Steel, D. Gammon, D. S. Katzer, D. Park, C. Piermarocchi, and L. J. Sham, "Rabi oscillations of excitons in single quantum dots," *Physical Review Letters*, vol. 87, no. 13, p. 133603, 2001. 78, 80

[92] P. Ester, L. Lackmann, S. M. de Vasconcellos, M. C. Hübner, A. Zrenner, and M. Bichler, "Single photon emission based on coherent state preparation," *Appl. Phys. Lett.*, vol. 91, no. 11, p. 111110, 2007. 78

[93] K. Koyama, M. Yoshita, M. Baba, T. Suemoto, and H. Akiyama, "High collection efficiency in fluorescence microscopy with a solid immersion lens," *Appl. Phys. Lett.*, vol. 75, no. 12, pp. 1667–1669, 1999. 78

[94] X. Li, Y. Wu, D. Steel, D. Gammon, T. H. Stievater, D. S. Katzer, D. Park, C. Piermarocchi, and L. J. Sham, "An all-optical quantum gate in a semiconductor quantum dot," *Science*, vol. 301, pp. 809–811, August 2003. 80

[95] L. Robledo, J. Elzerman, G. Jundt, M. Atature, A. Hogele, S. Falt, and A. Imamoglu, "Conditional dynamics of interacting quantum dots," *Science*, vol. 320, pp. 772–775, May 2008. 80

[96] Z. Yuan, B. E. Kardynal, R. M. Stevenson, A. J. Shields, C. J. Lobo, K. Cooper, N. S. Beattie, D. A. Ritchie, and M. Pepper, "Electrically driven single-photon source," *Science*, vol. 295, pp. 102–105, January 2002. 80

[97] R. J. Young, M. R. Stevenson, P. Atkinson, K. Cooper, D. A. Ritchie, and A. J. Shields, "Improved fidelity of triggered entangled photons from single quantum dots," *New Journal of Physics*, vol. 8, p. 29, February 2006. 80

[98] R. Hafenbrak, S. M. Ulrich, P. Michler, L. Wang, A. Rastelli, and O. G. Schmidt, "Triggered polarization-entangled photon pairs from a single quantum dot up to 30 k," *New Journal of Physics*, vol. 9, p. 315, September 2007. 80

[99] M. Atature, J. Dreiser, A. Badolato, and A. Imamoglu, "Observation of faraday rotation from a single confined spin," *Nat Phys*, vol. 3, pp. 101–106, February 2007. 80

[100] C. Santori, D. Fattal, J. Vuckovic, G. S. Solomon, and Y. Yamamoto, "Indistinguishable photons from a single-photon device," *Nature*, vol. 419, pp. 594–597, October 2002. 80, 104, 108

[101] D. S. L. Mui, D. Leonard, L. A. Coldren, and P. M. Petroff, "Surface migration induced self-aligned inas islands grown by molecular beam epitaxy," *Applied Physics Letters*, vol. 66, no. 13, pp. 1620–1622, 1995. 80

[102] Y. Sugiyama, Y. Nakata, K. Imamura, S. Muto, and N. Yokoyama, "Stacked inas self-assembled quantum dots on (001) gaas grown by molecular beam epitaxy," *Japanese Journal of Applied Physics*, vol. 35, pp. 1320–1324, 1996. 80

[103] M. Kitamura, M. Nishioka, J. Oshinowo, and Y. Arakawa, "In situ fabrication of self-aligned ingaas quantum dots on gaas multiatomic steps by metalorganic chemical vapor deposition," *Applied Physics Letters*, vol. 66, no. 26, pp. 3663–3665, 1995. 80

[104] S. Liang, H. L. Zhu, and W. Wang, "Temperature-dependent bimodal size evolution of inas quantum dots on vicinal gaas(100) substrates," *Journal of Applied Physics*, vol. 100, no. 10, 2006. 80

[105] S. Liang, H. Zhu, J. Pan, X. Ye, and W. Wang, "Growth of inas quantum dots on vicinal gaas (100) substrates by metalorganic chemical vapor deposition and their optical properties," *Journal of Crystal Growth*, vol. 289, pp. 477–484, April 2006. 80

[106] A. A. Tonkikh, G. E. Cirlin, V. G. Dubrovskii, Y. B. Samsonenko, N. K. Polyakov, V. A. Egorov, A. G. Gladyshev, N. V. Kryzhanovskaya, and V. M. Ustinov, "Quantum dots in inas layers of subcritical thickness on gaas(100)," *Technical Physics Letters*, vol. 29, pp. 691–693, August 2003. 80

[107] V. G. Dubrovskii, G. E. Cirlin, and V. M. Ustinov, "The effective thickness, temperature and growth rate behavior of quantum dot ensembles," *physica status solidi (b)*, vol. 241, no. 10, pp. R42–R45, 2004. 81

[108] G. E. Cirlin, G. M. Guryanov, A. O. Golubok, Ya, N. N. Ledentsov, P. S. Kop'ev, M. Grundmann, and D. Bimberg, "Ordering phenomena in inas strained layer morphological transformation on gaas (100) surface," *Applied Physics Letters*, vol. 67, no. 1, pp. 97–99, 1995. 81

[109] V. Talalaev, B. Novikov, S. Verbin, A. Novikov, Son, I. Shchur, G. Gobsch, R. Goldhahn, N. Stein, A. Golombek, G. Tsyrlin, V. Petrov, V. Ustinov, A. Zhukov, and A. Egorov, "Recombination emission from inas quantum dots grown on vicinal gaas surfaces," *Semiconductors*, vol. 34, pp. 453–461, April 2000. 81

[110] D. V. Regelman, U. Mizrahi, D. Gershoni, E. Ehrenfreund, W. V. Schoenfeld, and P. M. Petroff, "Semiconductor quantum dot: A quantum light source of multicolor photons with tunable statistics," *Physical Review Letters*, vol. 87, p. 257401, Nov 2001. 82

[111] D. Gammon, E. S. Snow, B. V. Shanabrook, D. S. Katzer, and D. Park, "Fine structure splitting in the optical spectra of single gaas quantum dots," *Physical Review Letters*, vol. 76, p. 3005, April 1996. 83

[112] Y. Aharonov and D. Bohm, "Significance of electromagnetic potentials in the quantum theory," *Physical Review*, vol. 115, no. 3, p. 485, 1959. 85

[113] S. Popescu, "Dynamical quantum non-locality," *Nature Physics*, vol. 6, pp. 151–153, March 2010. 85

[114] A. G. Aronov and Yu, "Magnetic flux effects in disordered conductors," *Reviews of Modern Physics*, vol. 59, pp. 755–779, Jul 1987. 85

[115] S. Zaric, G. N. Ostojic, J. Kono, J. Shaver, V. C. Moore, M. S. Strano, R. H. Hauge, R. E. Smalley, and X. Wei, "Optical signatures of the aharonov-bohm phase in single-walled carbon nanotubes," *Science*, vol. 304, pp. 1129–1131, May 2004. 85

[116] A. Fuhrer, S. Luscher, T. Ihn, T. Heinzel, K. Ensslin, W. Wegscheider, and M. Bichler, "Energy spectra of quantum rings," *Nature*, vol. 413, pp. 822–825, October 2001. 85, 86

[117] A. O. Govorov, S. E. Ulloa, K. Karrai, and R. J. Warburton, "Polarized excitons in nanorings and the optical aharonov-bohm effect," *Physical Review B*, vol. 66, p. 081309, Aug 2002. 85, 86, 87

[118] M. Grochol, F. Grosse, and R. Zimmermann, "Optical exciton aharonov-bohm effect, persistent current, and magnetization in semiconductor nanorings of type i and ii," *Physical Review B*, vol. 74, p. 115416, Sep 2006. 85, 86, 91

[119] E. Ribeiro, A. O. Govorov, W. Carvalho, and G. M. Ribeiro, "Aharonov-bohm signature for neutral polarized excitons in type-ii quantum dot ensembles," *Physical Review Letters*, vol. 92, p. 126402, Mar 2004. 85, 87

[120] I. R. Sellers, V. R. Whiteside, I. L. Kuskovsky, A. O. Govorov, and B. D. McCombe, "Aharonov-bohm excitons at elevated temperatures in type-ii znte/znse quantum dots," *Physical Review Letters*, vol. 100, p. 136405, Apr 2008. 85, 86, 87

[121] M. D. Teodoro, V. L. Campo, V. L. Richard, E. Marega, G. E. Marques, G. ao Gobato, F. Iikawa, M. J. S. P. Brasil, Z. Y. AbuWaar, V. G. Dorogan, Yu, M. Benamara, and G. J. Salamo, "Aharonov-bohm interference in neutral excitons: Effects of built-in electric fields," *Physical Review Letters*, vol. 104, p. 086401, Feb 2010. 85, 87

[122] A. M. Fischer, V. L. Campo, M. E. Portnoi, and R. A. Römer, "Exciton storage in a nanoscale aharonov-bohm ring with electric field tuning," *Physical Review Letters*, vol. 102, p. 096405, Mar 2009. 85, 86, 89, 94

[123] T. Lundström, W. Schoenfeld, H. Lee, and P. M. Petroff, "Exciton storage in semiconductor self-assembled quantum dots," *Science*, vol. 286, pp. 2312–2314, 1999. 85, 94

[124] A. Lorke, R. J. Luyken, A. O. Govorov, J. P. Kotthaus, J. M. Garcia, and P. M. Petroff, "Spectroscopy of nanoscopic semiconductor rings," *Physical Review Letters*, vol. 84, pp. 2223–2226, Mar 2000. 86

[125] N. A. J. M. Kleemans, I. M. A. B. Silkens, V. M. Fomin, V. N. Gladilin, D. Granados, A. G. Taboada, J. M. Garc'ia, P. Offermans, U. Zeitler, P. C. M. Christianen, J. C. Maan, J. T. Devreese, and P. M. Koenraad, "Oscillatory persistent currents in self-assembled quantum rings," *Physical Review Letters*, vol. 99, p. 146808, Oct 2007. 86

[126] L. G. G. V. Dias da Silva, S. E. Ulloa, and T. V. Shahbazyan, "Polarization and aharonov-bohm oscillations in quantum-ring magnetoexcitons," *Physical Review B*, vol. 72, p. 125327, Sep 2005. 86

[127] R. A. Römer and M. E. Raikh, "Aharonov-bohm effect for an exciton," *Physical Review B*, vol. 62, pp. 7045–7049, Sep 2000. 86

[128] C. A. *JETP Lett.*, vol. 62, p. 900, 1995. 86

[129] M. Tadić, N. Čukarić, V. Arsoski, and F. M. Peeters, "Anticrossing-induced optical excitonic aharonov-bohm effect in strained type-i semiconductor nanorings," Mar 2010. 86

[130] M. Bayer, M. Korkusinski, P. Hawrylak, T. Gutbrod, M. Michel, and A. Forchel, "Optical detection of the aharonov-bohm effect on a charged particle in a nanoscale quantum ring," *Physical Review Letters*, vol. 90, p. 186801, May 2003. 86

[131] A. V. Maslov and D. S. Citrin, "Enhancement of the aharonov-bohm effect of neutral excitons in semiconductor nanorings with an electric field," *Physical Review B*, vol. 67, p. 121304, Mar 2003. 86

[132] A. A. High, E. E. Novitskaya, L. V. Butov, M. Hanson, and A. C. Gossard, "Control of exciton fluxes in an excitonic integrated circuit," *Science*, vol. 321, pp. 229–231, July 2008. 86

[133] F. Ding, L. Wang, S. Kiravittaya, E. Müller, A. Rastelli, and O. G. Schmidt, "Unveiling the morphology of buried in(ga)as nanostructures by selective

wet chemical etching: From quantum dots to quantum rings," *Applied Physics Letters*, vol. 90, no. 17, p. 173104, 2007. 86, 87

[134] R. J. Warburton, C. Schaflein, D. Haft, F. Bickel, A. Lorke, K. Karrai, J. M. Garcia, W. Schoenfeld, and P. M. Petroff, "Optical emission from a charge-tunable quantum ring," *Nature*, vol. 405, pp. 926–929, June 2000. 87

[135] T. C. Lin, C. H. Lin, H. S. Ling, Y. J. Fu, W. H. Chang, S. Di Lin, and C. P. Lee, "Impacts of structural asymmetry on the magnetic response of excitons and biexcitons in single self-assembled in(ga)as quantum rings," *Physical Review B*, vol. 80, p. 081304, Aug 2009. 87, 91

[136] V. M. Fomin, V. N. Gladilin, J. T. Devreese, N. A. J. M. Kleemans, M. Bozkurt, and P. M. Koenraad, "Electron and exciton energy spectra in self-assembled ingaas/gaas ring-like nanostructures," *physica status solidi (b)*, vol. 245, no. 12, pp. 2657–2661, 2008. 91

[137] M. F. Tsai, H. Lin, C. H. Lin, S. Di Lin, S. Y. Wang, M. C. Lo, S. J. Cheng, M. C. Lee, and W. H. Chang, "Diamagnetic response of exciton complexes in semiconductor quantum dots," *Physical Review Letters*, vol. 101, p. 267402, Dec 2008. 94

[138] F. Ding, R. Singh, J. D. Plumhof, T. Zander, V. Křápek, Y. H. Chen, M. Benyoucef, V. Zwiller, K. Dörr, G. Bester, A. Rastelli, and O. G. Schmidt, "Tuning the exciton binding energies in single self-assembled ingaas/gaas quantum dots by piezoelectric-induced biaxial stress," *Physical Review Letters*, vol. 104, p. 067405, Feb 2010. 94

[139] C. K. Hong, Z. Y. Ou, and L. Mandel, "Measurement of subpicosecond time intervals between two photons by interference," *Physical Review Letters*, vol. 59, pp. 2044–2046, Nov 1987. 104

[140] R. Loudon, *The Quantum Theory of Light.* Oxford University Press, 3 ed., 2000. 104

[141] D. Bouwmeester, J.-W. Pan, K. Mattle, M. Eibl, H. Weinfurter, and A. Zeilinger, "Experimental quantum teleportation," *Nature*, vol. 390, pp. 575–579, December 1997. 104

[142] A. Kiraz, M. Ehrl, Th, M. oğlu, C. Bräuchle, and A. Zumbusch, "Indistinguishable Photons from a Single Molecule," *Physical Review Letters*, vol. 94, p. 223602, Jun 2005. 104

[143] R. Lettow, Y. L. A. Rezus, A. Renn, G. Zumofen, E. Ikonen, S. Götzinger, and V. Sandoghdar, "Quantum Interference of Tunably Indistinguishable Photons from Remote Organic Molecules," *Physical Review Letters*, vol. 104, p. 123605, Mar 2010. 104

[144] E. B. Flagg, A. Muller, S. V. Polyakov, A. Ling, A. Migdall, and G. S. Solomon, "Interference of Single Photons from Two Separate Semiconductor Quantum Dots," *Physical Review Letters*, vol. 104, p. 137401, Apr 2010. 104

[145] R. B. Patel, A. J. Bennett, I. Farrer, C. A. Nicoll, D. A. Ritchie, and A. J. Shields, "Two-photon interference of the emission from electrically tunable remote quantum dots," *Nature Photonics*, vol. 4, pp. 632–635, July 2010. 104

[146] T. Legero, T. Wilk, A. Kuhn, and G. Rempe, "Characterization of single photons using two-photon interference," 2005. 104

Summary

Optical Properties of Semiconductor Quantum Dots

This thesis presents different optical experiments performed on small semiconductor structures called quantum dots. These structures behave as boxes for electrons and holes allowing to confine a small number of them to a tiny region of space, some nm across. The aim of this work was to study the basic properties of different types of quantum dots made of various materials and with different techniques. The main feature of quantum dots is that confinement causes electrons and holes to sit on an essentially discrete set of energy levels. Although the separation of these levels can be comparable to the energy scale k_BT at room temperature, the experiment presented here needed to be conducted at a temperature of some Kelvin, in order to reduce scattering processes, namely with phonons.

This research was motivated by the fact that the conventional way of producing (growing) quantum dots by self-assembly has some limitations. Self assembled dots have excellent optical properties, but there are serious limitations to the materials that can be used and to the shape that can be given to both the dot and the surrounding semiconductor structure. More flexibility in the choice of materials and shapes would allow to design quantum dots with specific energy configurations, useful for different applications. Some examples that are closely related to the work presented here are the emission of photons at telecom wavelengths, the realization of efficient LEDs emitting single photons, the optical coupling of a quantum dot to an atomic vapor or the switching on and off of an optical transition. It is with this applications in mind that we studied different kinds of quantum dots in collaboration with many Dutch and international partners including Philips, NIST (US), the Ioffe Institute (Russia), the CNRS (France) and the Max Plank Institute (Germany).

From a chronological point of view the work described in this thesis opens and closes with experiments on quantum dots in nanowires to which chapters 4, 5 and 6 are devoted. These structures are interesting because of the choice of materials that they offer and because their shape is that of a quantum dot with two leads attached. We presented some successful examples of fabrication and testing of dots made of InAsP, incorporated in a InP wire. We demonstrated that quantum dots in nanowires can have reasonably narrow optical transitions, with linewidths below 30 μeV (the resolution of our spectrometer). Unfortunately it is still not possible to produce structures of such a quality in a reproducible way, but the optimization of nanowire growth performed at Philips allowed for an overall improvement of the quantum dot linewidths and brightness. Selecting some particularly good dots it was possible to produce excitons in a given spin state (Chapter 5) and to show that, in the presence of a magnetic field, this state is preserved for a time comparable to the exciton lifetime. This is interesting in view of using the electron or hole spin for quantum information purposes. In order to study what is the influence of a magnetic field on electrons and holes in nanowire dots we decided to measure their g-factors in different directions. This was possible only in the latest months, when a cryostat with a *vector* magnet was available. The results (Chapter 6) are still preliminary because we could perform a wide set of measurements only on one dot, but they suggest that we could determine the g-factors of electrons and holes in two directions.

We examined two other kinds of quantum dots, mainly with the aim of selecting dots with a specific level structure for a proposed experiment [Avron]. We soon realized that these dots were not suitable for this purpose and this led us to different research paths. We studied how a type of GaAs quantum dots can be used in combination with an atomic vapour with optical transitions at similar energy as the dot (Chapter 7) and we characterized small InAs dots grown on misoriented substrates (Chapter 8).

In collaboration with the group of A. Rastelli (Dresden) we studied InAs quantum rings in order to detect the Aharonov-Bohm effect for neutral excitons. The experiments (Chapter 9) show oscillations that are compatible with the Aharonov-Bohm effect both according to a quite refined theoretical model and to a more simplistic one (Chapter 10). Moreover, the oscillations can be tuned by an electric field which could allow for making an optical memory by electrically turning a transition from bright to dark (storage) and bright again (readout).

The last chapter of this thesis deals with a definetely more complex experiment in which we studied two-photon interference. Apart from being a nice quantum effect it is also a useful tool for different quantum information protocols like linear

optics quantum computation and the entanglement of remote qubits. The work presented in chapter 11 was made especially with the latter application in mind. We demostrated that a InAs quantum dot can emit pairs of indistiguishable photons (80% average wave-packet overlap) with a delay of about 5 ns between them.

<div align="right">

Umberto Perinetti
January 2011

</div>

Samenvatting

Optische Eigenschappen van Halfgeleidende Quantum Dots

Dit proefschrift beschrijft verschillende optische experimenten die gedaan zijn met kleine halfgeleidende structuren genaamd quantum dots. Deze structuren gedragen zich als doosjes voor electronen en gaten, en maken het mogelijk om een klein aantal daarvan op te sluiten in een zeer kleine ruimte, van enkele nanometers groot. Het doel van dit werk was om de basale eigenschappen te bestuderen van verschillende typen quantum dots, gemaakt van verschillende materialen en met verschillende technieken. Het belangrijkste kenmerk van quantum dots is dat het opsluiten van electronen en gaten zorgt voor gekwantiseerde energietoestanden. Alhoewel de afstand tussen deze energieniveaus vergelijkbaar kan zijn met de energieschaal k_bT op kamertemperatuur, moesten de experimenten die hier beschreven worden toch gedaan worden op een temperatuur van een aantal Kelvin, om verstrooiingsprocessen met phononen te onderdrukken. Dit onderzoek was gemotiveerd door het feit dat de conventionele manier om quantum dots the produceren (groeien) door zelf-assemblage een aantal beperkingen heeft. Zelf-geassembleerde quantum dots hebben uitstekende optische eigenschappen, maar er zijn serieuze beperkingen wat betreft de materialen die gebruikt kunnen worden en de vorm die aan zowel de dot als de omringende halfgeleiderstructuur kan worden gegeven. Meer flexibiliteit in de keuze van materialen en vormen zou het mogelijk maken quantum dots met specifieke energieconfiguraties te ontwerpen, die nuttig kunnen zijn voor verschillende toepassingen. Een aantal voorbeelden van toepassingen die nauw gerelateerd zijn aan dit werk zijn het uitzenden van photonen op telecom golflengten, het realizeren van een efficinte LED die enkele photonen kan uitzenden, het optisch koppelen van een quantum dot en een atomisch gas, en het aan- en uitschakelen van een optische transitie. Met deze toepassingen in het achterhoofd hebben we verschillende soorten quantum dots onderzocht in samenwerking met veel Nederlandse en internationale partners, waaronder Philips, NIST (VS), het Ioffe Institute (Rusland), CNRS (Frankrijk) en het Max Planck Institute (Duitsland). Chronologisch gezien be-

gint en eindigt dit werk met experimenten aan quantum dots in nanodraden, dat wordt beschreven in hoofdstuk 4, 5 en 6. Deze structuren zijn interessant door de keuze van materialen die mogelijk wordt gemaakt en doordat de geometrie een quantum dot met twee contacten is. We beschrijven succesvolle voorbeelden van fabricage en metingen aan dots gemaakt van InAsP, ingebed in een draad van InP. We hebben aangetoond dat quantum dots in nanodraden redelijk smalle optische transities kunnen hebben, met lijnbreedtes beneden 30 μeV (de resolutie van onze spectrometer). Helaas is het nog steeds niet mogelijk structuren van deze kwaliteit op een reproduceerbare manier te maken, maar de optimalizatie van nanodraad-groei bij Philips heeft wel een algehele verbetering van de lijnbreedte en de helderheid als resultaat. Door een aantal bijzonder goede dots te selecteren was het mogelijk om selectief excitonen te produceren in een gecontroleerde spin-toestand (hoofdstuk 5) en om aan te tonen dat, in aanwezigheid van een magnetisch veld, deze toestand behouden blijft voor een tijd vergelijkbaar met de exciton levensduur. Dit is interessant met oog op het gebruik van de electron- of gat-spin voor quantum informatie toepassingen. Om te bestuderen wat de invloed van een magnetisch veld op electronen en gaten in nanodraad dots is hebben we besloten hun g-factoren in verschillende richtingen te meten. Dit was pas mogelijk in de laatste maanden, toen een cryostaat met een vectormagneet beschikbaar was. De resultaten (hoofdstuk 6) zijn nog voorlopig omdat we aan slechts n dot een grote set metingen hebben kunnen doen, maar lijken te suggereren dat we de g-factoren van electronen en gaten in twee richtingen kunnen bepalen. We hebben nog twee andere soorten quantum dots onderzocht, voornamelijk met het doel dots met een bepaalde energiestructuur te selecteren voor een voorgesteld experiment [Avron]. We realizeerden echter al snel dat deze dots niet geschikt waren voor dat experiment, en dat leidde ons naar een andere onderzoeksrichting. We bestudeerden hoe een bepaald type GaAs quantum dot gebruikt kan worden in combinatie met een atomisch gas met een optische transitie op een vergelijkbare energie als de dot (hoofdstuk 7), en we karakteriseerden kleine InAs dots gegroeid in verkeerd georinteerde substraten (hoofdstuk 8). In samenwerking met de groep van A. Rastelli (Dresden) bestudeerden we InAs quantum ringen om het Aharonov-Bohm effect te detecteren voor neutrale excitonen. De experimenten (hoofdstuk 9) laten oscillaties zien die overeenstemmen met het Aharonov-Bohm effect, zowel volgens een gerafineerd theoretisch model als een eenvoudiger model (hoofdstuk 10). Verder kunnen de oscillaties worden benvloed door een electrisch veld, wat zou kunnen leiden tot een optisch geheugen door electrisch een transitie van licht naar donker (opslag) en weer naar licht (uitlezing) te brengen. Het laatste hoofdstuk van dit proefschrift gaat over een complexer experiment, waarbij we twee-photon interferentie hebben

bestudeerd. Afgezien van het feit dat het een interessant quantum effect is, is het ook een nuttig gereedschap voor verschillende quantum informatie protocollen zoals lineare-optica quantum berekeningen en het verstrengelen van afgelegen qubits. Het werk dat besproken wordt in hoofdstuk 11 was vooral gedaan met dit laatste in het achterhoofd. We hebben aangetoond dat een InAs quantum dot paren niet-onderscheidbare photonen kan uitzenden (80% golfpakket overlap) met een vertraging van ongeveer 5 ns tussen beiden.

Umberto Perinetti
Januari 2011

Curriculum Vitae

Umberto Perinetti

October 5, 1981	Born in L'Aquila, Italy.
1995 – 2000	High school, Liceo Scientifico A. Bafile, L'Aquila, Italy.
2000 – 2003	BSc Physics, University of Pisa. BSc supervisor: prof. D. Anselmi Subject: Bohm mechanics
2003 – 2005	MSc Physics, University of Pisa. MSc supervisor: prof. F. Beltram Subject: Tunneling between edge states of a quantum Hall system
2000 – 2005	Student at Scuola Normale Superiore, Pisa
2005 – 2010	PhD research, Delft University of Technology under supervision of dr. Valery Zwiller and prof. dr. ir. L. P. Kouwenhoven Subject: Optical properties of semiconductor quantum dots.

Publications

1. *Tuning single GaAs quantum dots in resonance with a rubidium vapor*
   N. Akopian, U. Perinetti, L. Wang, O. G. Schmidt, A. Rastelli, & V. Zwiller
   Applied Physics Letters, **97**, 113108 (2010)

2. *Single quantum dot nanowire photodetectors*
   M. P. van Kouwen, M. H. M. van Weert, M. E. Reimer, N. Akopian, U. Perinetti,
   R. Algra, E. P. A. M. Bakkers, L. P. Kouwenhoven, & V. Zwiller
   Applied Physics Letters, **97**, 082103 (2010)

3. *Gate controlled Aharonov-Bohm-type oscillations from single neutral excitons in quantum rings*
   F. Ding, N. Akopian, B. Li, U. Perinetti, A. Govorov, F. M. Peeters, C. C. Bof Bufon, C. Deneke, Y. H. Chen, A. Rastelli, O. G. Schmidt, & V. Zwiller
   Physical Review B, **82**, 075309 (2010)

4. *Orientation-Dependent Optical-Polarization Properties of Single Quantum Dots in Nanowires*
   M. H. M. van Weert, N. Akopian, F. Kelkensberg, U. Perinetti, M. P. van Kouwen,
   J. G. Rivas, M. T. Borgstrm, R. E. Algra, M. A. Verheijen, E. P. A. M. Bakkers,
   L. P. Kouwenhoven, & V. Zwiller
   Small, Vol. **5**, No. 19, pp. 2134-2138 (2009)

5. *Sharp emission from single InAs quantum dots grown on vicinal GaAs surfaces*
   U. Perinetti, N. Akopian, Yu. A. D. Bouravleuv, G. E. Cirlin, & V. Zwiller
   Applied Physics Letters, **94**, 163114 (2009)

6. *Optics with single nanowires*
   V. Zwiller, N. Akopian, M. H. M. van Weert, M. P. van Kouwen, U. Perinetti,
   L .P. Kouwenhoven, R. Algra, J. Gomez Rivas, E. Bakkers, & G. Patriarche
   Comptes Rendus Physique, **9**, 804 (2008)

7. *Selective excitation and detection of spin states in a single nanowire quantum dot*
   M. H. M. van Weert, N. Akopian, U. Perinetti, M. P. van Kouwen,
   R. E. Algra, M. A. Verheijen, E. P. Bakkers, L. P. Kouwenhoven, & V. Zwiller
   Nano Letters, **5**, 1989 (2009)

8. *Superconducting single photon detectors with minimized polarization dependence*
   S. N. Dorenbos, E. M. Reiger, N. Akopian, U. Perinetti, V. Zwiller, T. Zijlstra, & T. M. Klapwijk
   Applied Physics Letters, **93**, 161102 (2008)

9. *Low noise superconducting single photon detectors on silicon*
   S. N. Dorenbos, E. M. Reiger, U. Perinetti, V. Zwiller, T. Zijlstra, & T. M. Klapwijk
   Applied Physics Letters, **93**, 131101 (2008)

10. *Growth and characterization of InP nanowires with InAsP insertions*
    M. Tchernycheva, G. E. Cirlin, G. Patriarche, L. Travers, V. Zwiller, U. Perinetti, & J. C. Harmand
    Nano Letters, **7**, 1500 (2007)

11. *Particle-hole symmetric Luttinger liquids in a quantum Hall circuit*
    S. Roddaro, U. Perinetti, V. Pellegrini, F. Beltram, L. Pfeiffer, & K. West
    Physica E: Low-dimensional Systems and Nanostructures, **34**, 132 (2006)